AD-A095 498 NAVAL OCEAN SYSTEMS CENTER SAN DIEGO CA F/G 4/1

TROPOSPHERIC REFRACTIVITY PROFILES INFERRED FROM RF MEASUREMENT--ETC(U)

OCT 80 K D ANDERSON

UNCLASSIFIED NOSC/TR-629 NL

1 OF 2

AD A
095498

NOSC

12

NOSC

NOSC TR 629

LEVEL II

NOSC TR 629

AD A095498

Technical Report 629

TROPOSPHERIC REFRACTIVITY PROFILES INFERRED FROM RF MEASUREMENTS

Passive Refractive Index by Satellite Monitoring (PRISM)

KD Anderson

24 October 1980

Final Report for Period October 1977 - September 1980

Prepared for
Naval Sea Systems Command
NAVSEA 62R13

Approved for public release; distribution unlimited

NAVAL OCEAN SYSTEMS CENTER
SAN DIEGO, CALIFORNIA 92152

NAVAL OCEAN SYSTEMS CENTER, SAN DIEGO, CA 92152

AN ACTIVITY OF THE NAVAL MATERIAL COMMAND

SL GUILLE, CAPT, USN
Commander

HL BLOOD
Technical Director

ADMINISTRATIVE INFORMATION

Work was performed under Program Element 62712N, Task Area SF12141491 (NOSC 82-CT48) by members of the Tropospheric Assessment Systems Branch (Code 5325) for Naval Sea Systems Command, NAVSEA 62R13. This report covers work from October 1977 to September 1980 and was approved for publication 24 October 1980.

Released by
JH Richter, Head
EM Propagation
Division

Under authority of
JD Hightower, Head
Environmental Sciences
Department

ACKNOWLEDGEMENTS

Many people contributed a great deal of time and effort to this study. The author wishes particularly to acknowledge HV Hitney for his assistance in the analytical efforts and WK Horner for providing the meteorological data.

To convert from	to	Multiply by
millibars	pascals (Pa)	100
degrees (angle)	mrad	~17.5

UNCLASSIFIED (14) NOSC-TR-629

SECURITY CLASSIFICATION OF THIS PAGE (When Data Entered)

REPORT DOCUMENTATION PAGE

READ INSTRUCTIONS BEFORE COMPLETING FORM

1. REPORT NUMBER: NOSC Technical Report 629 (TR 629)

2. GOVT ACCESSION NO.: AD-A095498

3. RECIPIENT'S CATALOG NUMBER: (1)

4. TITLE (and Subtitle): TROPOSPHERIC REFRACTIVITY PROFILES INFERRED FROM RF MEASUREMENTS - Passive Refractive Index by Satellite Monitoring (PRISM).

5. TYPE OF REPORT & PERIOD COVERED: Final rept. Oct[redacted]977 - Sep[redacted]80

6. PERFORMING ORG. REPORT NUMBER

7. AUTHOR(s): KD Anderson (12) 99

8. CONTRACT OR GRANT NUMBER(s): (17)

9. PERFORMING ORGANIZATION NAME AND ADDRESS: Naval Ocean Systems Center, San Diego, CA 92152

10. PROGRAM ELEMENT, PROJECT, TASK AREA & WORK UNIT NUMBERS: PE 62712N SF 12141491 (NOSC 82-CT48)

11. CONTROLLING OFFICE NAME AND ADDRESS: Naval Sea Systems Command, NAVSEA 62R13, Washington, DC 20362

12. REPORT DATE: 24 Oct[redacted]80

13. NUMBER OF PAGES: 98

14. MONITORING AGENCY NAME & ADDRESS (if different from Controlling Office): (16) F12141

15. SECURITY CLASS. (of this report): Unclassified

15a. DECLASSIFICATION/DOWNGRADING SCHEDULE

16. DISTRIBUTION STATEMENT (of this Report)

Approved for public release; distribution unlimited

17. DISTRIBUTION STATEMENT (of the abstract entered in Block 20, if different from Report)

18. SUPPLEMENTARY NOTES

19. KEY WORDS (Continue on reverse side if necessary and identify by block number)

Troposphere; Refractive index; Structural properties; Radio-frequency ducting; Atmospheric ducting; Passive Refractive Index by Satellite Monitoring (PRISM)

20. ABSTRACT (Continue on reverse side if necessary and identify by block number)

The objective of this work was to develop and validate a technique for passively inferring the tropospheric refractivity structure from observations of low-angle, satellite-to-ground rf transmissions. Eleven measurements of dual-frequency radio transmissions were made. The ducting structure was correctly inferred in seven of the lower frequency and five of the high-frequency observations. The inferred profile structure can differ significantly from the observed refractive structure. The major limitation to the applicability of this technique is an uncorrectable rms range error of about 4 km. These errors are caused by small-scale refractivity fluctuations in the atmosphere. Although moderate success was achieved in inferring the refractive structure from rf measurements, it is recommended that this project be terminated, since operationally significant data cannot be extracted reliably.

DD FORM 1 JAN 73 1473 EDITION OF 1 NOV 65 IS OBSOLETE S/N 0102-LF-014-6601

(UNCLASSIFIED)

SECURITY CLASSIFICATION OF THIS PAGE (When Data Entered)

343159

OBJECTIVE

Develop and validate a technique for passively inferring the tropospheric refractivity structure from observations of low-angle, satellite-to-ground rf transmissions.

RESULTS

1. Eleven measurements of dual-frequency radio transmissions were made during the summer of 1978.

2. Application of the technique correctly infers the ducting structure in seven of the lower frequency observations and five of the high-frequency observations.

3. Inferred profile structure can differ significantly from the observed refractive structure.

4. The major limitation to the applicability of this technique is an uncorrectable rms range error of approximately 4 km.

5. Moderate success was achieved in inferring the refractive structure from rf measurements.

RECOMMENDATION

Terminate this project, since operationally significant data cannot be extracted reliably.

CONTENTS

ILLUSTRATIONS

TABLES

INTRODUCTION

Modern naval microwave communication and sensor system performance can be greatly affected by refractive conditions. For example, a typical surface search radar system, under standard atmospheric conditions, can normally detect targets up to 30 km distant. Under atmospheric conditions in which a surface-based duct is present, however, it is not uncommon for this radar system to detect the same targets at ranges in excess of 300 km.

Statistics on refractive conditions found in a maritime environment are useful as an aid in determining the scope of environmental effects on microwave system performance. A 5-year data base of upper air soundings from 921 radiosonde stations distributed throughout the world was extensively analyzed by GTE/Sylvania (ref 1). The results of this study were examined by NOSC for radiosonde stations situated along ocean coastal regions, island stations, and meteorological station ships (category "C" stations). The following conclusions were drawn: (1) Surface-based ducts occur worldwide 6 percent of the time on the average. (2) The average thickness of the surface-based duct is less than 100 m. (3) Elevated ducts occur 13 percent of the time on the average. (4) The average height of the elevated duct is less than 1500 m. These percentages seem low, but they represent an average worldwide occurrence. In some areas of the world, the percentages are significantly higher. In the San Diego locale, for example, a surface-based duct occurs 23 percent of the time and an elevated duct occurs 48 percent of the time. These percentages relate directly to microwave system performance and can be used to indicate, by geographical regions, locales in which propagation anomalies may significantly affect operations. While such statistics may be useful for long-range planning, it is the current refractive conditions that must be understood for immediate operations.

Assessment of the refractive effects on microwave systems must be considered a twofold problem. First, a reasonably accurate representation of the vertical refractivity structure is required. Second, a computational and display system is needed that relates the refractive environment to those effects by means of EM propagation models. The Integrated Refractive Effects Prediction System (IREPS) (ref 2) provides the hardware and software necessary to determine the atmospheric refractive effects on microwave systems. IREPS is currently installed aboard 13 of the Navy's major combatants and its products are valued in operational decisionmaking. This system essentially satisfies the second portion of the assessment problem.

---

1. GTE/Sylvania Inc Final Report, Radiosonde Data Analysis-Five Years Data, by LD Ortenburger, NSA Contract MDA 904-76-C-0233, 29 July 1977.
2. NOSC TD 238, Integrated Refractive Effects Prediction System (IREPS), Interim User's Manual, by HV Hitney and RA Paulus, March 1979.

Two methods are used by the operational forces to obtain the refractivity structure: a balloonborne radiosonde and an airborne microwave refractometer. Each method suffers drawbacks. In particular, the radiosonde radiates approximately 1 W at 403 MHz, which renders this method undesirable during periods of electromagnetic control (EMCON). Because it is an airborne system, the refractometer is an expensive measurement and is available only on a select few aircraft.

Although each method can measure the refractivity structure, a technique entitled Passive Refractive Index by Satellite Monitoring (PRISM) was proposed as a potentially useful third alternative. By receiving rf transmissions from a satellite and inferring the refractivity structure from the location of the interference nulls (created by the path-length difference between the direct and sea-reflected rays), PRISM provides several advantages. First and foremost, the technique is completely passive since only the satellite radiates. Second, since the location of the interference null is detectable by measuring the relative amplitude of the signal, the receiver hardware is relatively simple. Third, the satellite does not have to be tracked by ground-station equipment since only a useable signal is required. Lastly, logistics support is minimal compared to that of radiosonde and refractometer methods .

It is the purpose of this paper to present the background, procedures, measurements, and results of the PRISM Project. PRISM was initiated in October 1977 under the sponsorship of the Naval Sea Systems Command, with the objective to develop and validate a technique proposed by HV Hitney (ref 3) to infer the tropospheric refractivity structure passively from rf measurements.

3. NOSC Technical Note NELC TN 3108, A Proposed Method to Infer Refractive-Index Profiles by Satellite Monitoring, by HV Hitney, 21 January 1976. NOSC TNs are informal documents intended chiefly for internal use.

BACKGROUND

Many experiments have been performed in the general field of rf inversion (ref 4). Occultation experiments have been successful in determining the refractivity structure for altitudes generally in excess of 10 km. Less successful have been attempts to infer the structure from measurements of elevation angle and Doppler shift. These methods generally require either extremely high accuracy of the ground-station tracking equipment or high frequency stability. In 1977, when this study began, no inversion technique was available to infer the low-level (less than 4 km altitude) refractivity structure passively with significant reliability and precision.

Examination of radio data measured on an aircraft-to-ground path (ref 5) indicated that the location of the interference nulls could be used first to infer the elevation angles to the required accuracy, then to infer the refractivity profile. In figure 1, the path length difference δ is related to the true elevation angle α (by ref 6) as follows:

$$\theta = \sqrt{(\alpha/3)^2 + 2h/3a_e} - \alpha/3 \tag{1}$$

$$\delta = 2\ (\alpha + \theta)^2 \sqrt{h^2 + a_e\ (a_e + h)\ \theta^2} \tag{2}$$

Equations (1) and (2) are valid if the direct and reflected rays are parallel. Considering the necessarily limited altitude of the aircraft, this condition was not strictly met. However, profiles were inferred that closely approximated the observed, warranting the extension of this technique to a satellite-to-ground path on which the rays would be parallel.

A ground-station receiver was designed and a suitable satellite was chosen in the time frame from October 1977 to June 1978. During July and August of 1978, observations of dual rf transmissions and the local refractivity structure were made (ref 7).

---

4. NASA TM X-62, 150, Mathematics of Profile Inversion, edited by L Colin, August 1972.

5. NOSC Technical Note NELC TN 2874, Propagation Measurements at 3 GHz in the San Diego Offshore Area, by KD Anderson and DR Jensen, 20 January 1975.

6. NRL Report 7098, Machine Plotting of Radio/Radar Vertical Coverage Diagrams, by LV Blake, Naval Research Laboratory, 25 June 1970.

7. NOSC TN 639, PRISM — Passive Refractive Index by Satellite Monitoring: Preliminary Measurements and Results, by KD Anderson and HV Hitney, March 1979.

Application of this inference technique to the observed data illustrated a major problem in the determination of δ: the path-length difference could not be extracted reliably from the frequency diversity information available. A procedure to recover δ from a simplified atmospheric model (ref 8) was investigated. This procedure started with higher elevation angles (70 milliradians), where the refractivity structure has negligible effect, and iterated δ for the lower angles. But since the combination of measurement inaccuracies and low angle refraction effects dominated, this procedure was found to be untenable.

Since the extraction of δ proved unworkable, the inference technique was modified. Briefly, it was found that possible null locations are easily determined from the signal received. Some of these locations must be true nulls. Comparing all possible null locations found to a library of null locations (computed by ray-trace techniques for a wide selection of assumed refractivity profiles) could yield a respectable inferred profile.

The following sections of this paper will examine the methodology of the modified technique, the measurements, and results.

EXPERIMENTAL PROCEDURES

METHODOLOGY

Inference of the tropospheric refractivity ducting environment is based upon a statistical analysis of satellite-to-ground rf transmissions. When the satellite is near the horizon (fig 1), the received signal is the sum of two rays. One ray propagates only through the atmosphere, the direct path, while the second ray is reflected from the surface of the ocean. Since there is a phase shift of π radians upon reflection, the received signal is a maximum when the path phase difference between the direct and reflected ray is an integral multiple of π. Conversely, when the path phase difference is a multiple of 2π (i.e. the path length difference is a multiple of one wavelength), the received signal is a minimum. As the satellite moves through its orbit, the path length difference changes over many wavelengths, resulting in a received signal that repeats maxima and minima with time or, correspondingly, with range. Each occurrence of the minimum, or null, is assigned a number based on the integral number of wavelengths difference between the direct and the sea-reflected paths. Null 1 corresponds to a path length difference of one wavelength, null 2 to a difference of two wavelengths, and so on.

---

8. A Null Finding Algorithm for PRISM, prepared for NOSC by PH Levine et al under Contract N00123-78-C-0043, 23 July 1979.

Figure 2 portrays the form of the received signal plotted as amplitude in dB versus ground range from the receiver to the satellite. Two sets of curves are shown, illustrating the effects of two different refractivity profiles. The solid-line plot represents the signal received under standard atmospheric conditions whereas the broken line shows the pattern when a moderately strong surface-based duct is present. Both cases are computed from ray trace procedures for a frequency of 1239 MHz, satellite height of 1000 km and a receiver height of 35 m. In addition to the received signal amplitude curves, the two curves proceeding from the lower left to the upper right relate the respective path length differences (null numbers) to ground range. The first null observed for the standard profile (solid-line plot) corresponds to a path-length difference of one wavelength. It occurs at a range of 3415 km. Note that for the surface-based duct environment (broken-line plot) the first observable minimum is not null 1, but rather null 3, which is found at a range of 3405 km. Note also that as the path-length difference increases (at increasing elevation angles) the location of each null tends to become independent of the refractivity structure.

These two theoretical plots of path-length difference as a function of range illustrate the methodology of the inversion technique. Simply, the form of the path-length difference (pld) curve is extracted from the observed data by noting the range at which each minimum occurs, without regard to an absolute null number assignment. The observed pld curve is then compared to a library of pld curves generated from a wide variety of refractivity profiles. The inferred profile is selected as the refractivity structure that yields the minimum standard deviation of the difference between the predicted and the observed ranges. For a given library profile null number, the range at which the null occurs is compared to every possible null location found in the observed data. If the minimum difference is less than 10 km, the observed location is noted. Otherwise the library null number is tagged as rejected. The minimum range difference is found for each null of the library profile. Up to 20 predicted nulls are examined. The standard deviation of the range differences is computed for the library profile. After these procedures have been completed for every profile, the "best fit" of the observed to the calculated pld curves is given by the profile that has the minimum standard deviation of the range differences and the fewest number of rejected library nulls.

Since the inference technique relies upon comparing modeled to observed data, the prediction accuracy is governed, in part, by the adequacy (number and scope) of the selected library profiles. Accordingly, figure 3 is a plot of null number as ordinate and ground range as abscissa for all the 438 refractivity profiles contained in the library. The figure illustrates the pld for a transmission frequency of 1239 MHz, a satellite height of 1000 km and a receiver height of 35 metres. An expansion about the first five null numbers is shown as figure 4. On

this figure is imposed the regional influence by ducting environment type. That is, the figure illustrates the possible ranges, as a function of pld, that can occur for a nonducting, an elevated, and a surface-based ducting refractivity profile. There are regions in which each ducting case singularly dominates, and there are regions in which two and even all three ducting cases compete. Although similar, the various pld curves are unique.

Figures 5 and 6 show the received signal measured on 20 July 1978 at 1946 (GMT) for transmission frequencies of 1239 MHz and 2891 MHz, satellite height of 1001 km, and receiver height of 35 metres. The path length difference curves are computed from ray trace methods by using the refractivity structure as measured by a radiosonde taken near the receiver site at 1945 (GMT) on the same day. As expected, the interference patterns exhibit maxima and minima in the presence of noise. Noise contributions are particularly noticeable at ranges exceeding 3350 km.

From examination of the data, one of the first questions to be addressed is "What constitutes an interference null?" For the lower frequency data, the null locations for ranges less than 3350 km are obvious. At greater ranges, however, are the minima true nulls or noise? Examination of the higher frequency data indicates fewer obvious nulls, with most minima uncertain. This problem was examined in detail, and empirical guidelines were established to define a null. These rules are developed as follows.

A range window is centered on each sample point of the data. If the amplitude of the current sample is the minimum value within the bounds of the window, the range at which the current sample occurs is tagged as a possible null location. The width of the window is approximately the range separation between adjacent high order nulls, and is 20 km for the 1239 MHz data and 10 km for the 2891 MHz data. In addition, nulls are defined to occur at ranges less than the maximum range at which the received signal is greater than the average amplitude of all samples. The primary motivation for this second requirement is explained with reference to figures 5 and 6. Note that the signal is observed for ranges in excess of 3500 km whereas the prediction indicates that the first observable null occurs at a range of 3409 km. Also note that the amplitude of the signal tends to decrease at a rate of 0.1 dB per km for ranges in excess of 3400 km. Since the measured refractivity structure shows a strong surface-based duct, it is thought that the unexpected appearance of the signal is due to coupling of energy into the duct at ranges well beyond the horizon. The imposition of the maximum range criteria removes this precursor from processing. To summarize the null definition, a maximum range at which nulls occur is imposed on the basis of the average value of the signal, and possible null locations are selected as the minimum value within a predefined range window.

The following sections will deal with the development and formulation of the library refractivity profiles, ray tracing procedures, and the hardware.

REFRACTIVITY PROFILE MODEL

The refractivity index, n, is defined as the ratio of the propagation velocity in a vacuum to the velocity in the medium. In the atmosphere, the value of n differs from unity by about 0.05 percent. It is convenient to define the refractivity, N, as $(n-1) \times 10^6$, which has values in the range 0 to 500. For radio frequencies, the refractivity is related to atmospheric temperature, pressure, and humidity by the relationship

$$N = 77.6P/T + 3.73 \times 10^5 e/T^2, \tag{3}$$

where P is the pressure in millibars, T is the air temperature in kelvins and e is the saturated water vapor pressure in millibars. In some applications it is desirable to remove the effects of the earth's curvature. This is accomplished by the modified refractivity, M, which is related to N as follows:

$$M = N + 0.157z, \tag{4}$$

where z is the height above the earth's surface, in metres.

Whenever M decreases with height, a so-called trapping layer is formed. An EM wave entering this region at a small angle is refracted or bent at a curvature greater than the curvature of the earth's surface. The height interval between the top of the trapping layer and the lowest height where a trapped ray propagates is called the ducting region, or duct. This region may be found by simple inspection of a plot of M as abscissa and height as ordinate (fig 7). A straightedge is placed parallel to the height axis through the M-unit value at the top of the trapping layer, and the ducting region is the height interval from that point to the first lower intersection of the straightedge with the M curve. In figure 7, the plot of M vs height illustrates two ducting regions. An elevated duct exists if the base of the duct is above the earth's surface, whereas a surface-based duct exists if the base of the duct is at the earth's surface.

Empirically, the environment model was divided into three regions (fig 8). Following Bean and Dutton (ref 9) in the height interval from 9 to 50 km above the earth, the N profile varies exponentially with height as follows:

$$N = 105 \exp[-0.1424 (Z-9)], \tag{5}$$

where Z is the height in kilometres. As the altitude increases to 50 km, N becomes 0.31; this value implies that the medium is a near-vacuum. For heights in excess of 50 km the medium is assumed to be a vacuum and N is independent of height, with a value of zero. In the region from the surface to 9 km the N curve is segmented, varying linearly with height. On the basis of many observations of real-world N profiles and experience in assessing propagation effects, a four-segment construction is used for the linear portion of the library N profiles.

RAY TRACING PROCEDURES

The location of the minima and the elevation angle in the inversion library are derived from refractivity profiles previously described and ray tracing calculations made on a digital computer. Since these computations are critical to the inversion process and differ from procedures developed by others, this section briefly describes the formulation.

A spherical coordinate system (ρ, θ, ϕ) with center at the center of the earth and a point source located at a height z_1 above the surface of the earth is illustrated in figure 9. Since the refractivity structure is assumed to be spherically symmetric, all functions are independent of ϕ and only the meridian plane is considered. Snell's law in this case may be written as

$$\frac{\rho n}{a} \cos \alpha = c, \tag{6}$$

where a is the earth's radius, ρ is the vector from the earth's center to a point along the ray, α is the angle formed between the normal of ρ and the ray, and c is a constant that is evaluated at any point along the ray where n, ρ, and α are known. From simple trigonometry, eq (6) can be expressed as

$$\frac{\rho n}{a} \sin \alpha = \pm\sqrt{(\rho n/a)^2 - c^2}. \tag{7}$$

9. Radio Meteorology, BR Beam and EJ Dutton, p 64, Dover Publications Inc, 1968.

Combining eq (6) and (7),

$$\tan \alpha = \frac{\pm\sqrt{(\rho n/a)^2 - c^2}}{c} = \frac{d\rho}{\rho d\theta}. \tag{8}$$

Integrating in terms of the central angle θ,

$$\theta = \pm c \int_{\rho_1}^{\rho_2} \frac{d\rho}{\rho\sqrt{(\rho n/a)^2 - c^2}}. \tag{9}$$

The quantity r, which is the distance the ray travels as measured along the earth's surface, is given by the relationship

$$r = \theta a. \tag{10}$$

Since the refractivity structure is composed of three regions-linear, exponential, and constant (unity)-the solution of eq (9) is examined in each region.

LINEAR REGION RAY TRACING

In the height interval from 0 to 9 km above the earth's surface, it is assumed that the distribution of n can be expressed in the form $n(\rho) = b_0 + b_1/\rho$ for an interval of ρ. The linear variation of n allows a closed form solution to eq (9) as follows:

$$\left.\begin{aligned} \theta &= \frac{-c}{\sqrt{\mu}} \ln\left[\frac{2\mu + \rho t + 2\sqrt{\mu v}}{\rho}\right] && (\mu > 0) \\ &= \frac{c}{\sqrt{-\mu}} \arctan\left[\frac{2\mu + \rho t}{2\sqrt{-\mu}\ \sqrt{v}}\right] && (\mu < 0) \\ &= -c\,\frac{2\sqrt{v}}{\rho t} && (\mu = 0) \end{aligned}\right\} \tag{11}$$

where

$$t = 2(b_0 b_1)/a$$

$$\mu = (b_0/a)^2$$

$$v = [(b_0\rho + b_1)/a]^2 - c^2.$$

For each linear segment of refractivity, the coefficients b_0 and b_1 are readily determined. A computer solution to this equation is easily amenable and the solution is rapidly found.

EXPONENTIAL REGION RAY TRACING

The refractivity in the height interval of 9 to 50 km above the earth's surface is given by equation (5) as

$$N = 105 \exp[-0.1424(Z-9)].$$

For any known pairs of α and η at the surface, the range, r, in this region can be found independently from all other regions since this curve is fixed. If the surface launch angle, α_0, of the ray and the surface value of the refractive index, η_0, are given, the ray characteristic, c, is established:

$$c = \eta_0 \cos \alpha_0. \quad (12)$$

Because η_0 typically is constrained to the interval of 1.0002 to 1.0005 and because the limits of α_0 are 0 to 70 milliradians, the value of c falls in the interval 0.99775 to 1.0005. Solutions to the ground range, r, as a function of c, with the above limitations, are presented in figure 10. These values were computed by using equation (9), which was numerically integrated. As shown, the quantity r varies from 350 to 500 km over the full interval of c. Since the discrete values of r, indicated by the crosses, are well behaved, a fourth degree polynomial interpolation function was made that describes r in terms of c. To improve accuracy, the interpolation function was not fit directly to c but rather to a quantity defined as $\chi = (c - 1) \times 10^6 + 2501$. The sum of the square of the deviations is less than 200 m. Coefficients of the polynomial as fit to χ are listed in figure 10. The net interpolation function provides a very rapid means of computing r, as the ray travels through the exponential region, from knowledge of the surface refractivity and elevation angle.

CONSTANT REGION RAY TRACING

The refractive index for heights exceeding 50 km is assumed to be unity. Since the refractivity of the medium does not vary with height, a ray propagating through this region will not be refracted and will, in fact, describe a straight line. Therefore a geometrical solution to equation (9) is readily attainable and is illustrated in figure 11. From the law of sines,

$$\theta_v = \pi - \alpha_v - \arcsin\left[\frac{\rho_v}{\rho_s}\sin(\alpha_v + \pi/2)\right], \tag{13}$$

where ρ_v is the vector from the earth's center to a height of 50 km, α_v is the angle between the normal of ρ_v and the ray, and ρ_s is the vector from the earth's center to the satellite. If the same reasoning is followed as in the previous section, the penetration angle, α_v, can be found from η_0 and α_0 by the relationship

$$\alpha_v = \arctan\left[\frac{\pm\sqrt{(\rho_v/a)^2 - c^2}}{c}\right]. \tag{14}$$

For a satellite at 1000 km altitude, the rate of change of r with respect to ρ_s is approximately 1.46 km per km for the interval $0.99775 < c < 1.0005$. The ground range, r, is normalized to a satellite height of 1000 km by adding $(a + 1000 - \rho_s) \times 1.46$ to the observed ground range. Normalization allows the library data to be computed only once, saving a considerable amount of time.

A FORTRAN program implementing the previous equations was written for a Data General NOVA 800 minicomputer with a hardware floating point processor. All computations are done with 15 digit accuracy, and the ground range, r, for a ray from the surface to a height of 1000 km, is found in approximately 100 ms.

TRANSMITTER

Satellite P76-5 was selected as the rf source for the measurement tests. Its orbit is sun-synchronous, which allows observations to be made at nearly the same time each day. The satellite was designed and constructed by Stanford Research Institute to support the Defense Nuclear Agency wideband satellite experiment (ref 10). It was placed into a 1000 km orbit for the purpose of carrying a multifrequency crystal-stabilized coherent rf transmitter to characterize transionospheric propagation effects. Ten frequencies are radiated: one at 137.7 MHz, seven in the 378 to 448 MHz band, and one each at 1239 and 2891 MHz. The antennas are nadir-directed and right circular polarized. Effective radiated power is 22 dBm at 1239 MHz and 19 dBm at 2891 MHz. In addition to these desirable hardware characteristics, ephemeral data could be obtained, on a weekly basis, from the Naval Astronautics Group, Pt Mugu, CA.

10. Early Results from the DNA Wideband Satellite Experiment—Complex Signal Scintillation, EJ Fremouw, Radio Science, vol 13, no 1, p 167-187, January-February 1978.

RECEIVER

The key to the success of the measurement program is the ability to detect the transmitted signals as the satellite is rising or setting on the horizon. This region is crucial since the dominant refractive effects occur for elevation angles less than 20 milliradians. Also it is the region where the received signals are lowest in intensity. Other design factors are the accuracy in predicting the satellite position and velocity vectors from available ephemeral data and an option to acquire data from satellites other than P76-5. In accordance with the above points, the design goals are as follows:

Instantaneous signal detection

Dual frequency

-145 dBm sensitivity

20 dB dynamic range

10 kHz acquisition bandwidth

100 mrad antenna beamwidth

Real-time processing

Balancing the design criteria led to the configuration shown in figure 12. The high gain, wide bandwidth rf preamplifier sets the overall noise figure to 4.5 dB. To attain the required sensitivity, a final IF bandwidth of 20 Hz was selected. A narrow bandwidth such as this combined with the instantaneous signal detection requirement abrogates the use of a single IF filter. A high speed digital signal processor (DSP—Spectral Dynamics model SD-360) was chosen to implement 512 contiguous IF filters in the range from dc to 10 kHz. This unit is the heart of the receiver, since it provides a dual-channel processor (two independent filter banks), 70 dB dynamic range, 10 kHz acquisition bandwidth, and real-time processing.

Instantaneous signal detection is accomplished by downconverting the rf signals to a nominal IF of 5 kHz. Uncertainties in the satellite position and frequency drift limit precise knowledge of the transmitted signal to approximately ±2 kHz; therefore the received IF falls between 3 and 7 kHz. Since this is well within the 10 kHz acquisition bandwidth, the received signal is immediately detectable. As the satellite moves through its orbit, the radial velocity varies, causing a slowly changing Doppler shift. To keep the signal in the acquisition band, the first local oscillators are manually adjusted to drive the IF to its nominal 5 kHz. Both first local oscillators (Hewlett Packard models 8614 and 8616 signal generators) are phase locked frequencies to 1.995 MHz offset from their respective transmit signals. The second local oscillator (Hewlett Packard model 5110B/5100A

synthesizer) is set to 2.0 MHz and drives both second stage mixers, generating the 5 kHz IF. An analog tape records the IF as a backup against computer failure.

Data processing and archiving are performed by a Data General NOVA 3/12 computer. The computer controls the DSP and sets it into a dual channel FFT processing mode for analyzing a 10 kHz band. Data gathering is initiated by an operator command and normally begins when a signature is observed on a spectral display. From this point, the computer logs the time of day and examines the dual spectrum every 50 ms (DSP analysis period). In each period, the amplitude and frequency information of the received signals is stored for further processing. The examination continues until halted by an operator command.

Table 1 lists the power budget factors for the P76-5 transmitter. Free space path loss is the attenuation in radiated power due to geometrical spreading and is given by the summation

$$\mathrm{FSPL} = 32.45 + 20 \log f + 20 \log d, \tag{15}$$

where f is the frequency in MHz and d is the distance from the source in km. The values listed are computed for a range of 4000 km. Antenna gains of 20 and 32 dB were measured by using a single ground station circular parabolic antenna 2 m in diameter. The antenna is fitted with a broadband horizontally polarized log periodic feed that passes signals from 800 MHz to 10 GHz. Summing the ERP, FSPL, gain and loss in table 1 gives received signal power levels of -127 dBm (1239 MHz) and -125 dBm (2891 MHz) which must be detected by the receiver. Measured receiver sensitivities at the two frequencies are -144 and -143 dBm, and the corresponding expected signal-to-noise ratios thus are +17 and +18 dB. Constructive interference of the direct ray and the sea-reflected ray increases the received power by 6 dB. Therefore, the dynamic range between maxima and minima is limited to +23 dB at 1239 MHz and +24 dB at 2891 MHz.

EXPERIMENTAL MEASUREMENTS

RADIO MEASUREMENTS

Eleven separate observations of the 1239 and 2891 MHz emissions of satellite P76-5 were made during July and August 1978. These observations were conducted by NOSC personnel at building T323, which is situated at 32°42' N latitude and 117°15' W longitude. The receiving antenna is 35 m above mean sea level (msl) and has an unobstructed view of the oceanic horizon for azimuthal angles of 190° to 340°. This antenna position allowed observations of P76-5 while it ascended and descended at the horizon on the same orbit. Table 2 illustrates the geometrical and temporal characteristics of each observation. The column labeled Start

	Power Level	
Frequency	1239 MHz	2891 MHz
ERP (dBm)	+22	+19
Free space path loss (dB)	-166	-173
Antenna gain	+20	+32
Polarization loss (dB)	-3	-3
Received signal level (dBm)	-127	-125
Receiver sensitivity (dBm)	-144	-143
SNR (dB)	+17	+18

Table 1. Power budget for Wideband Satellite (P76-5).

Date (1978)	Start Time (GMT)	Nominal Height (km)	Ascending = A Descending = D	Horizon Azimuth Angle (degrees)	RAOB Time (GMT)
20 July	1946	1001	A	193.9	1945
20 July	2002	1022	D	332.4	
28 July	1951	1009	A	195.8	2000
28 July	2006	1032	D	331.5	
2 August	1956	1039	D	334.5	2005
3 August	2020	1019	A	212.5	2028
3 August	2034	2038	D	322.3	
14 August	2039	1036	A	224.8	2039
14 August	2051	1048	D	314.7	
16 August	2013	1037	A	207.9	2013
16 August	2028	1050	D	324.9	

Table 2. PRISM measurement periods.

Time (GMT) indicates the time at which the observation began. The termination of the measurement normally occurred approximately 4 minutes after this time. Average height of the satellite above msl is computed from ephemeral data for each observation and is listed in the column labeled Nominal Height (km). Each measurement is indicated as ascending or descending at the start time, and the azimuthal angle from the receiver to the horizon point is shown. The eleven observations were made on six separate days at approximately 2000 GMT (12 noon local time); and except on 2 August, both the ascending and descending measurements were taken within 20 minutes of each other.

REFRACTIVE PROFILE MEASUREMENTS

Upper air soundings, known as radiosonde observations or RAOBs, were made by NOSC personnel at approximately the same time as each day's period of radio measurements. The radiosondes were launched at a site only tens of metres distant from the receiving antenna. To provide a better definition of the refractivity structure, the humidity and temperature elements were electrically interchanged. This modification allows the radiosonde to sample and transmit humidity information for a longer period and does not affect the calibration or analysis of the data. Telemetry from the radiosonde was recorded on strip charts and manually decoded to provide values of pressure, air temperature, and humidity. These atmospheric quantities were then processed by a computer program to obtain the modified refractivity, in M-units, as a function of height in metres above msl. A description of the observed refractivity profiles is provided in table 3. This table shows whether the duct is surface based (SBD) or elevated (ELV) and lists the geometrical characteristics. Strong surface-based ducts were observed on 20 July and 16 August; moderate to weak elevated ducts were observed for the remaining four periods.

MEASUREMENT PERIODS

A summary of the inferred data is shown by table 4. The summary includes, for each frequency, the inferred duct type, the standard deviation of the range differences between the observed and "best fit" null locations, and a subjective measure of the agreement between the observed and inferred refractivity profiles. A rating of good is given if the inferred profile geometry reasonably approximates the observed; moderate indicates that the inferred duct type agrees with the observed but the geometries differ signficantly; poor is assigned if neither the geometry nor the type agrees. For the 1239 MHz data, the summary shows that the inferred duct type (surface based, elevated, or no ducts) agrees with the observed in seven of the eleven measurements. But the subjective agreement between the inferred and observed is rated as good in only four cases. The inferred duct type for the 2891 MHz data matches in five of the eleven observations although the subjective agreement of the inferred to the observed profile is moderate at best.

Date (1978)	Duct Type	Layer Top (m)	Layer Base (m)	ΔM	Duct Base (m)	Duct Thickness (m)
20 July	SBD	359.2	349.5	-72.6	0	359.2
28 July	ELV	787.0	465.3	-22.1	266.8	520.2
2 August	2 ELV	693.6	486.7	-11.1	422.5	271.1
		1171.4	898.0	-21.4	769.0	402.4
3 August	ELV	584.4	493.0	-13.0	390.6	193.8
14 August	ELV	633.9	422.4	-33.5	128.9	505.0
16 August	SBD	394.5	328.5	-58.8	0	394.5

SBD: surface-based duct
ELV: elevated duct

Table 3. Summary of observed RAOBs.

			1239 MHz			2891 MHz)		
Date (1978)	Start Time (GMT)	Observed Duct Type	Inferred Duct Type	Standard Deviation (km)	Agreement	Inferred Duct Type	Standard Deviation (km)	Agreement
20 July	1946	SBD	SBD	1.93	Good	SBD	2.67	Moderate
	2002	SBD	SBD	3.13	Moderate	SBD	2.11	Moderate
28 July	1951	ELV	None	5.28	Poor	SBD	1.79	Poor
	2006	ELV	ELV	1.41	Moderate	ELV	2.06	Moderate
2 August	1956	2 ELV	ELV	2.64	Good	ELV	1.38	Moderate
3 August	2020	ELV	SBD	5.58	Poor	SBD	2.61	Poor
	2034	ELV	SBD	3.57	Poor	SBD	2.64	Poor
14 August	2039	ELV	SBD	2.39	Poor	SBD	2.89	Poor
	2051	ELV	ELV	3.44	Moderate	SBD	2.13	Poor
16 August	2013	SBD	SBD	1.73	Good	ELV	2.53	Poor
	2028	SBD	SBD	2.83	Good	SBD	2.77	Moderate

Table 4. Summary of inferred data.

Plots of the received signal and the inferred profiles are included for reference. Each of the eleven measurement periods (all in 1978) is examined, and the observed refractivity profile, signal received, and inferred profile are discussed.

20 JULY MEASUREMENTS

This measurement is characterized by an intense surface-based duct, illustrated in figure 13. Top height of the duct is 359 m and the layer thickness is 10 m. The M-unit difference between the top and base of the layer of -72.6 M-units shows this to be one of the most intense ducts yet observed in the San Diego area. An interesting feature of this profile is its obvious trilinearity. Since the comparison library profiles are linear segments (to 9 km), a reasonably good agreement is expected.

Figure 14 is a plot of the 1239 MHz signal received as P76-5 was ascending at 1946 GMT. The "best fit" pld curve is superimposed and indicates a surface based duct as the pld curve terminates at null 3. Crosses (+) on this plot show the null number (ordinate) vs range (abscissa) matrix of all possible nulls searched. These crosses are shown for only the even null numbers, since placing crosses for each null number would clutter the figure. The "best fit" modified refractive index profile is shown in figure 15. Note the spectacular similarity between the observed and predicted profiles even though the top height of the predicted duct is 109 m below the observed duct.

Figures 16 and 17 illustrate the 2891 MHz received signal and the inferred profile for the ascension of P76-5. Note in particular the uneven range spacing of the possible null locations and the ragged appearance of the signal. Although the inferred profile is a surface-based duct, the geometries are considerably different from the observed profile.

Figure 18 illustrates the 1239 MHz signal received as P76-5 was descending to the horizon, taken approximately 16 minutes after the ascending measurement. Note that the possible null locations are not as deep as the locations shown by figure 14. Because the computer did not start acquisition of the real-time signal properly, the data displayed by figure 18 is derived from reprocessing the real-time signal captured on the analog tape backup system. Since this tape tends to increase the noise threshold of the signal, the depth of the nulls is not as great. Nevertheless, the null locations for ranges less than 3350 km are clearly defined. The inferred profile is plotted as figure 19. This profile indicates a moderately strong surface-based duct, but its similarity to the observed is not as striking as in the ascending case. Note also that the standard deviation of the range differences is 3.13 km as compared to a standard deviation of 1.93 km for the earlier measurement.

Figures 20 and 21 illustrate the 2891 MHz received signal and the inferred profile for the descending pass of P76-5. Since

the signal was processed from the backup tape system, the possible null locations are not as deep as expected. The inferred profile is a surface-based duct and appears to better represent the observed as compared to the inferred profile from the lower frequency measurement. The best fit standard deviation is 2.11 km for the 2891 MHz signal and 3.13 km for the 1239 MHz signal.

28 JULY MEASUREMENTS

This measurement is characterized by a moderate elevated duct and is shown in figure 22. Top height of the duct is 787 m, with a layer thickness of 321.7 m. Note that several linear segments compose the trapping layer. The base of the duct is 266.8 m and the duct thickness is 520.2 m.

Figure 23 is a plot of the 1239 MHz signal received as P76-5 was ascending at 1951 GMT. The possible null locations are relatively well defined, with amplitude depths of nearly 20 dB. The inferred profile (fig 24) shows a nonducting situation, which does not agree with the observed. Standard deviation is 5.28 km, a magnitude which indicates that the inversion technique performed poorly.

Figures 25 and 26 illustrate the 2891 MHz signal and the inferred profile for the ascension of P76-5. The range separation of the possible null locations is uneven and the appearance of the signal is ragged. An intense surface-based duct is inferred. Surprisingly, the standard deviation is 1.79 km, which indicates a close approximation.

Figure 27 is a plot of the 1239 MHz signal received as P76-5 was descending at 2006 GMT. Possible null locations are well defined. An elevated duct is inferred, as illustrated by figure 28. The duct thickness of 410 m agrees favorably with the observed thickness, but the top of the duct is 663 m higher. A standard deviation of 1.41 km indicates a good fit.

Figures 29 and 30 illustrate the 2891 MHz signal and the inferred profile for the descending pass of P76-5. The possible null locations are unevenly spaced and the signal appears ragged. An elevated duct is inferred although the geometry is different from the observed. A standard deviation of 2.06 km suggests a moderately good fit.

2 AUGUST MEASUREMENTS

This measurement is characterized by a dual elevated duct and is shown in figure 31. The lowest duct extends from a base at 422.5 m to a top at 693.6 m. A second duct exists from a base at 769 m to a top at 1171.4 m. The observed structure cannot be inferred, since only single-duct structures are included in the library.

Figure 32 illustrates the 1239 MHz signal received as P76-5 was descending to the horizon. The ascension of P76-5 occurred at an azimuth angle that the receiver could not observe. An elevated duct is inferred and, referencing figure 33, is a reasonable one-duct approximation to the observed. A standard deviation of 2.64 km is found.

Figures 34 and 35 illustrate the 2891 MHz signal and the inferred profile for the descending pass. The relative spacing of the possible null locations is more regular although the signal is ragged in appearance. An elevated duct is inferred that is much weaker than the observed. A standard deviation of 1.38 km indicates a good fit.

3 AUGUST MEASUREMENTS

This measurement is characterized by a relatively weak elevated duct illustrated by figure 36. The duct extends from 390.6 to 584.4 m with a ΔM of -13 M-units. A trilinear profile could be constructed that reasonably fits the observed.

Figure 37 is a plot of the 1239 MHz signal received as P76-5 was ascending at 2020 GMT. The range separation between possible null locations is uneven and the signal for ranges greater than 3200 km is ragged. A moderate albeit thick surface-based duct is inferred and is shown in figure 38. The standard deviation of 5.58 km indicates a poor fit.

Figures 39 and 40 illustrate the 2891 MHz signal and the inferred profile for the ascension. The signal is typical of the 2891 MHz data, having uneven spacing between the possible null locations and appearing ragged. A standard deviation of 2.61 km indicates a moderate fit although the inferred profile is an intense surface-based duct.

Figure 41 is a plot of the 1239 MHz signal received as P76-5 was descending at 2034 GMT. Possible null locations are readily observable for ranges less than 3300 km and tend to lose definition at greater ranges. An intense low level surface-based duct is inferred, as shown in figure 42. The standard deviation is 3.57 km.

Figures 43 and 44 illustrate the 2891 MHz signal and the inferred profile for the descending pass. The inferred profile is an intense surface-based duct with a top at 750 m. A moderately good fit is indicated by a standard deviation of 2.64 km.

14 AUGUST MEASUREMENTS

This measurement is characterized by a moderate elevated duct, as shown in figure 45. The duct exists between 128.9 and 633.9 m with a ΔM of -33.5 M-units. The profile is reasonably trilinear.

Figure 46 is a plot of the 1239 MHz signal as P76-5 was ascending at 2039 GMT. Possible null locations are readily observable for ranges less than 3350 km and tend to become indistinct at longer ranges. A moderate surface-based duct is inferred, as shown in figure 47. Standard deviation is 2.39 km.

Figures 48 and 49 illustrate the 2891 MHz signal and the inferred profile for the ascending pass. A moderate surface-based duct is inferred and the standard deviation is 2.89 km.

Figure 50 is a plot of the 1239 MHz signal as P76-5 was descending at 2051 GMT. The signal is similar to the ascending pass. A tremendous elevated duct is inferred and is shown in figure 51. Top height of the inferred duct is 1750 m, with base at 279 m and a ΔM of -90 M-units. A standard deviation of 3.44 km is found.

Figures 52 and 53 illustrate the 2891 MHz signal and the inferred profile for the descending pass. A strong surface-based duct is inferred and the base of the layer closely matches the observed. Standard deviation is 2.13 km.

16 AUGUST MEASUREMENTS

This measurement is characterized by a strong surface-based duct, as shown by figure 54. Top height of the duct is at 394.5 m, with a ΔM of -58.8 M-units. The profile can be accurately represented by a trilinear structure.

Figure 55 is a plot of the 1239 MHz signal as P76-5 was ascending at 2013 GMT. The possible null locations appear relatively clean and correctly separated in range. A surprisingly good approximation to the observed profile is inferred as shown by figure 56, although the top of the duct is 94 m below the observed. The M difference is -59 M-units and closely matches the observed. A good fit is indicated by a 1.73 km standard deviation.

Figures 57 and 58 illustrate the 2891 MHz signal and the inferred profile for the ascending pass. The possible null locations are unevenly spaced and the signal amplitude appears ragged. A strong elevated duct is inferred with a standard deviation of 2.53 km.

Figure 59 is a plot of the 1239 MHz signal as P76-5 was descending at 2028 GMT. The possible nulls are not as clean as in the ascending pass. Nevertheless, the inferred profile reasonably approximates the observed, as shown by figure 60. A standard deviation of 2.83 km is found.

Figures 61 and 62 illustrate the 2891 MHz signal and the inferred profile for the descending pass. A strong surface-based duct is inferred and a standard deviation of 2.77 km is found.

RESULTS

This technique was applied to eleven observations of dual-frequency transmissions made on a satellite-to-ground path. The major findings are as follows:

> Seven observations of the 1239 MHz data correctly predicted the measured ducting environment. However, the geometry of the inferred profile (top height of the duct, base of the layer, etc) can differ significantly from the measured profile geometry.
>
> Five observations of the 2891 MHz data correctly predicted the measured ducting environment. Again, the geometries of the observed and inferred profiles can differ significantly.
>
> Ray traces (based on the measured refractivity) compared to the observed radio data indicate rms elevation angle errors of 605 μrad for the 1239 MHz data and 430 μrad for the 2891 MHz data.
>
> The rms range error between the computed null location (based on the measured refractivity) and the observed null location is 4.2 km for the 1239 MHz data and 3.7 km for the 2891 MHz data.
>
> The rms elevation angle and range errors appear to be caused by small scale refractivity perturbations. These errors are uncorrectable and bound the attainable accuracy for any shallow angle rf measurements.

The first two findings are derived directly from table 4, which is a summary of the data inferred from the rf measurements. A detailed examination of each measurement period is provided in the prior section.

Range errors are estimated by computing the null locations by means of the observed refractive structure and comparing these locations to the observed locations. The comparison is identical to that described for the inference technique. Figures 63 and 64 illustrate the range errors for all measurement periods as a function of elevation angle. The rms errors are 4.2 km for the 1239 MHz data and 3.7 km for the 281 MHz data. Since the range separation between higher elevation angle nulls is approximately 20 km (1239 MHz) and 8.7 km (2891 MHz), the inference technique performs better with the lower frequency data than with the higher frequency data. An rms error of 3.7 km is nearly half of the range separation at the higher frequency. Therefore the null locations are uncertain to plus or minus one null number. Since the rms range error for the lower frequency is approximately 20% of the range separation, the uncertainty in the null location is less than one null number and can be extracted with better reliability.

Elevation angle errors, shown by figures 65 and 66, are computed from the range error measurements. For each null location in the observed data, an equivalent elevation angle is interpolated from the predicted ray trace data. The elevation angle error is the difference between the predicted angle and the interpolated angle. The 0.61 mrad error for the 1239 MHz signal is in close agreement to a value of 0.52 mrad, found by Crane (ref 11) at an elevation angle of 17 mrad for a 1295 MHz radar.

CONCLUSION

A complex measurement program was undertaken to examine the feasibility of passively inferring the tropospheric refractive index structure from observations of low angle satellite-to-ground rf transmissions. The results of this study show moderate success in profile inference, but the technique cannot provide reliable and operationally significant data.

RECOMMENDATION

Although the results of this study show a moderate success in inferring the refractive structure from rf measurements, it is recommended that this project be terminated, since operationally significant data cannot be extracted reliably.

11. RADC-TR-78-252, Analysis of Tropospheric Effects at Low Elevation Angles, by RK Crane, p 51-55, November 1978.

REFERENCES

1. GTE/Sylvania Inc Final Report, Radiosonde Data Analysis—Five Years Data, by LD Ortenburger, NSA Contract MDA 904-76-C-0233, 29 July 1977.

2. NOSC TD 238, Integrated Refractive Effects Prediction System (IREPS), Interim User's Manual, by HV Hitney and RA Paulus, March 1979.

3. NOSC Technical Note NELC TN 3108, A Proposed Method to Infer Refractive-Index Profiles by Satellite Monitoring, by HV Hitney, 21 January 1976. NOSC TNs are informal documents intended chiefly for internal use.

4. NASA TM X-62, 150, Mathematics of Profile Inversion, edited by L Colin, August 1972.

5. NOSC Technical Note NELC TN 2874, Propagation Measurements at 3 GHz in the San Diego Offshore Area, by KD Anderson and DR Jensen, 20 January 1975.

6. NRL Report 7098, Machine Plotting of Radio/Radar Vertical Coverage Diagrams, by LV Blake, Naval Research Laboratory, 25 June 1970.

7. NOSC TN 639, PRISM—Passive Refractive Index by Satellite Monitoring: Preliminary Measurements and Results, by KD Anderson and HV Hitney, March 1979.

8. A Null Finding Algorithm for PRISM, prepared by NOSC by PH Levine et al under Contract N00123-78-C-0043, 23 July 1979.

9. Radio Meteorology, BR Bean and EJ Dutton, p 64, Dover Publications Inc, 1968.

10. Early Results from the DNA Wideband Satellite Experiment—Complex Signal Scintillation, EJ Fremouw et al, Radio Science, vol 13, no 1, p 167-187, January-February 1978.

11. RADC-TR-78-252, Analysis of Tropospheric Effects at Low Elevation Angles, by RK Crane, p 51-55, November 1978.

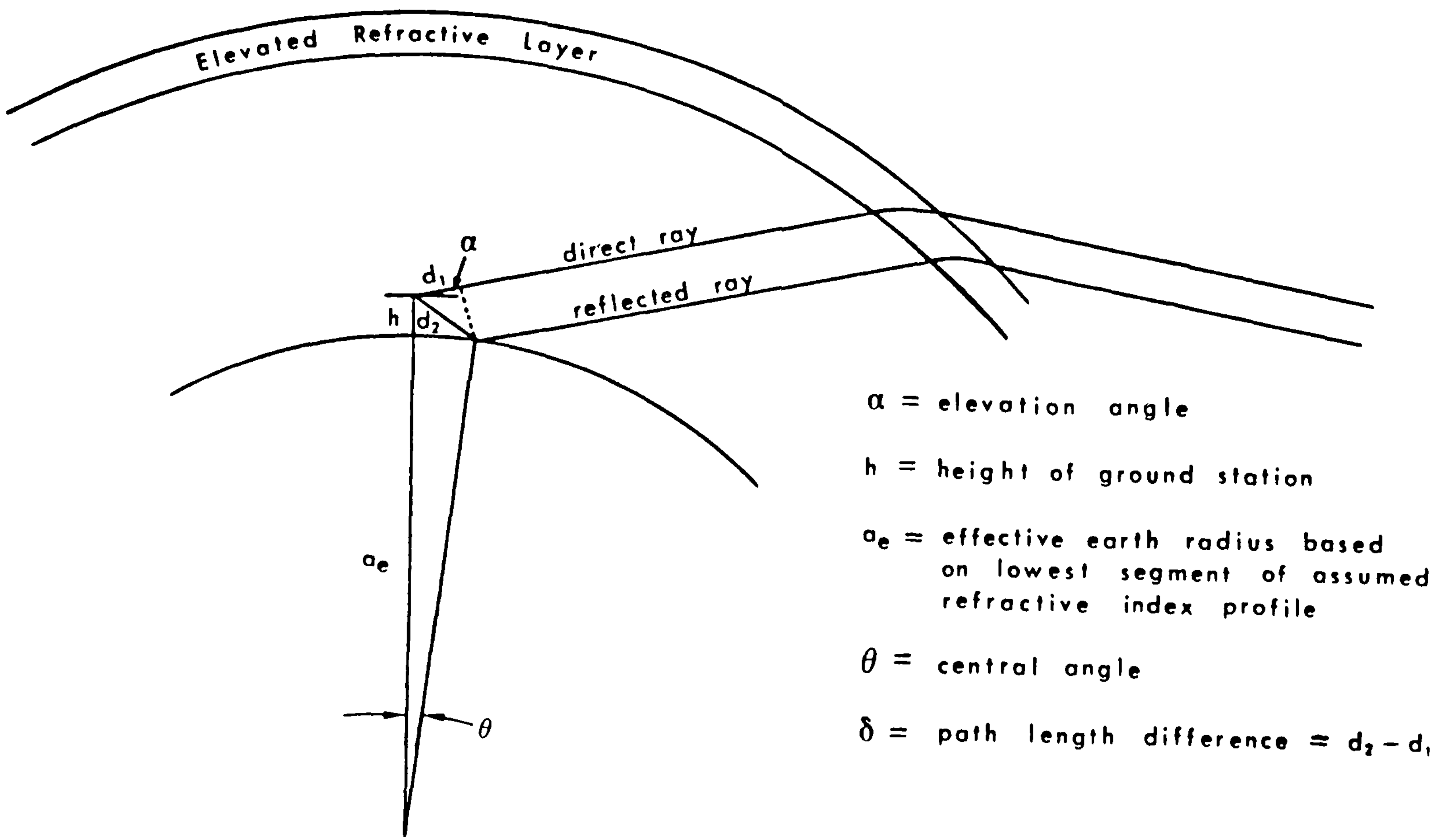

Figure 1. Satellite-to-ground path length difference geometry.

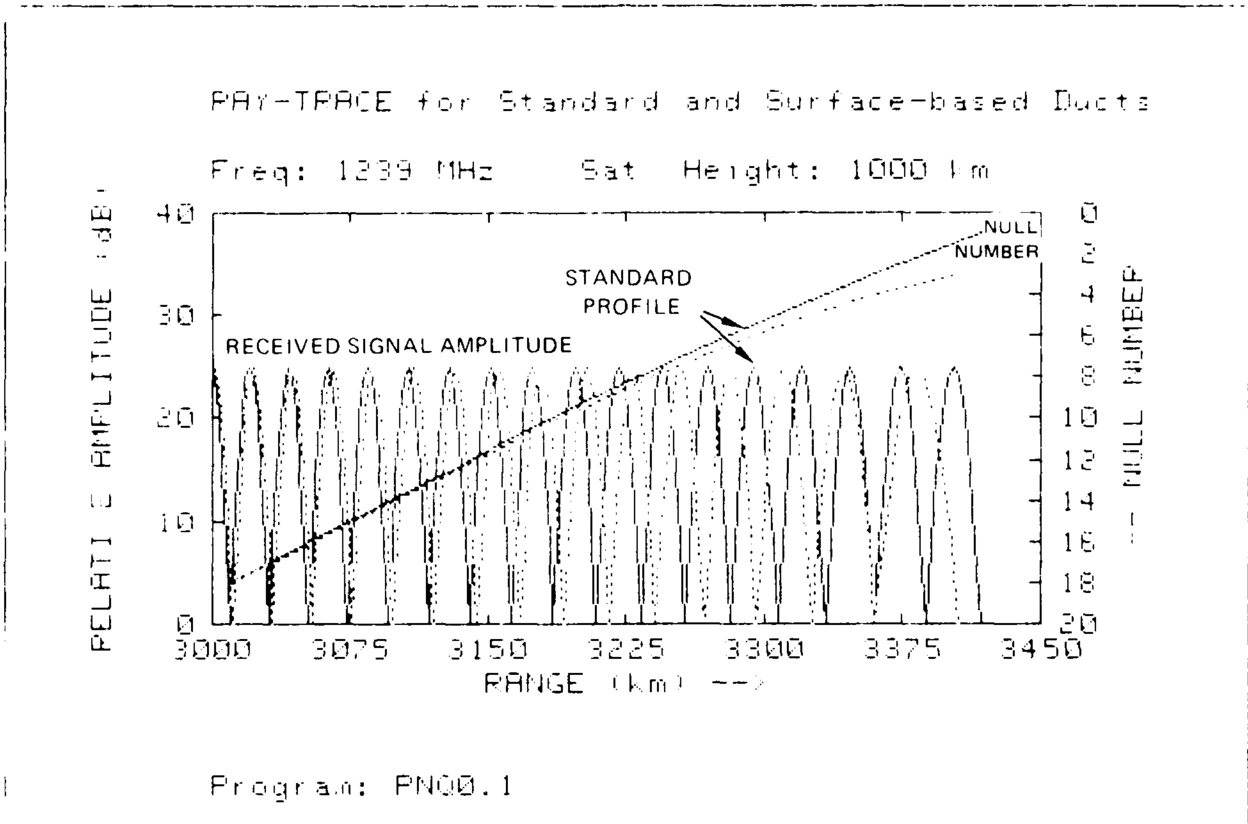

NULL	..STANDARD... ALPHA mrad	RANGE km	SURFACE-BASED ALPHA mrad	RANGE km	NULL	..STANDARD... ALPHA mrad	RANGE km	SURFACE-BASED ALPHA mrad	RANGE km
20	69.2	2968.1	69.2	2969.6	19	65.7	2988.8	65.7	2990.4
18	62.2	3009.7	62.2	3011.5	17	58.8	3030.8	58.8	3032.8
16	55.3	3052.1	55.3	3054.4	15	51.8	3073.6	51.8	3076.2
14	48.4	3095.4	48.4	3098.3	13	44.9	3117.4	44.9	3120.9
12	41.4	3139.8	41.4	3143.7	11	38.0	3162.4	38.0	3167.0
10	34.5	3185.5	34.5	3191.0	9	31.0	3208.9	31.1	3215.6
8	27.6	3232.7	27.6	3240.9	7	24.1	3256.9	24.1	3267.4
6	20.6	3281.7	20.7	3295.3	5	17.2	3307.0	17.2	3325.5
4	13.7	3332.9	13.7	3359.9	3	10.2	3359.7	10.2	3405.8
2	6.6	3387.6	++.+	++++.+	1	2.9	3417.6	++.+	++++.+

Figure 2. Received signal as a function of range for a standard atmosphere and a surface-based duct.

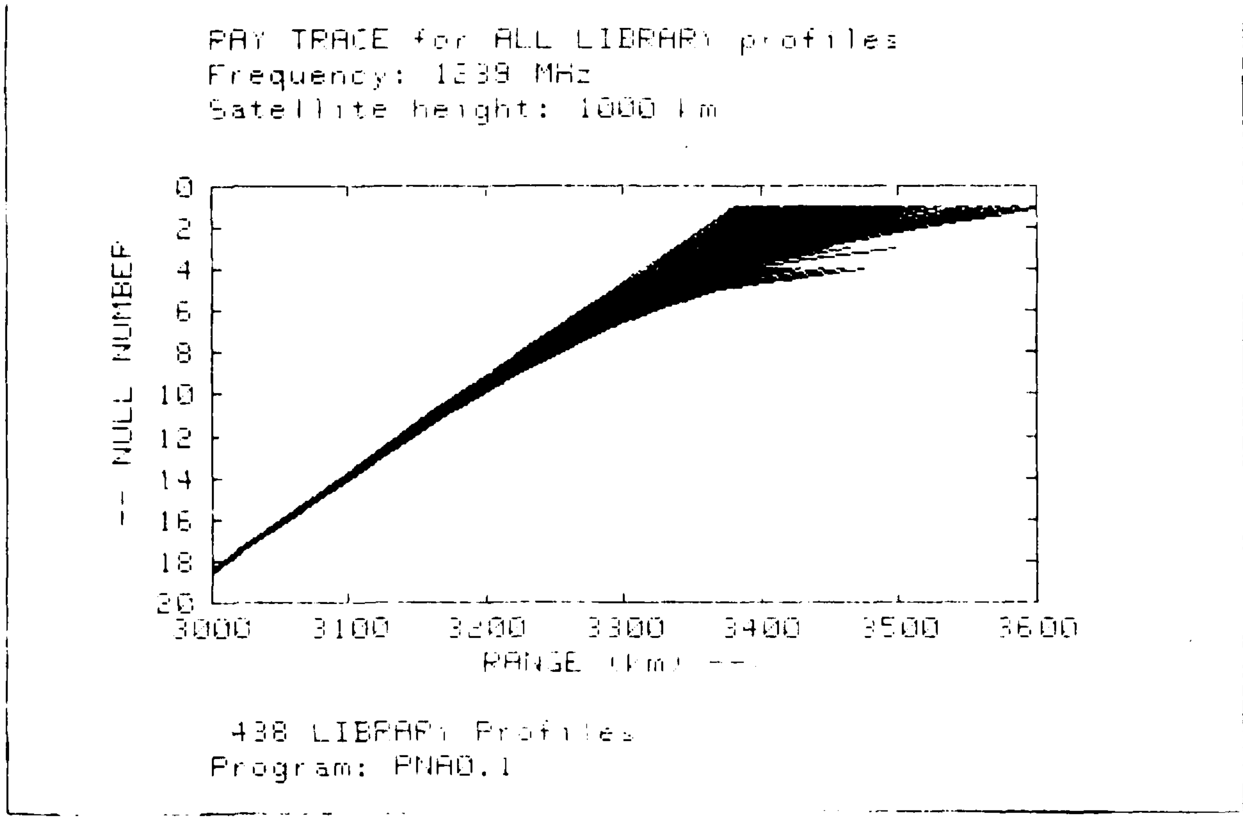

Figure 3. Plot of path length difference as a function of range for all library profiles.

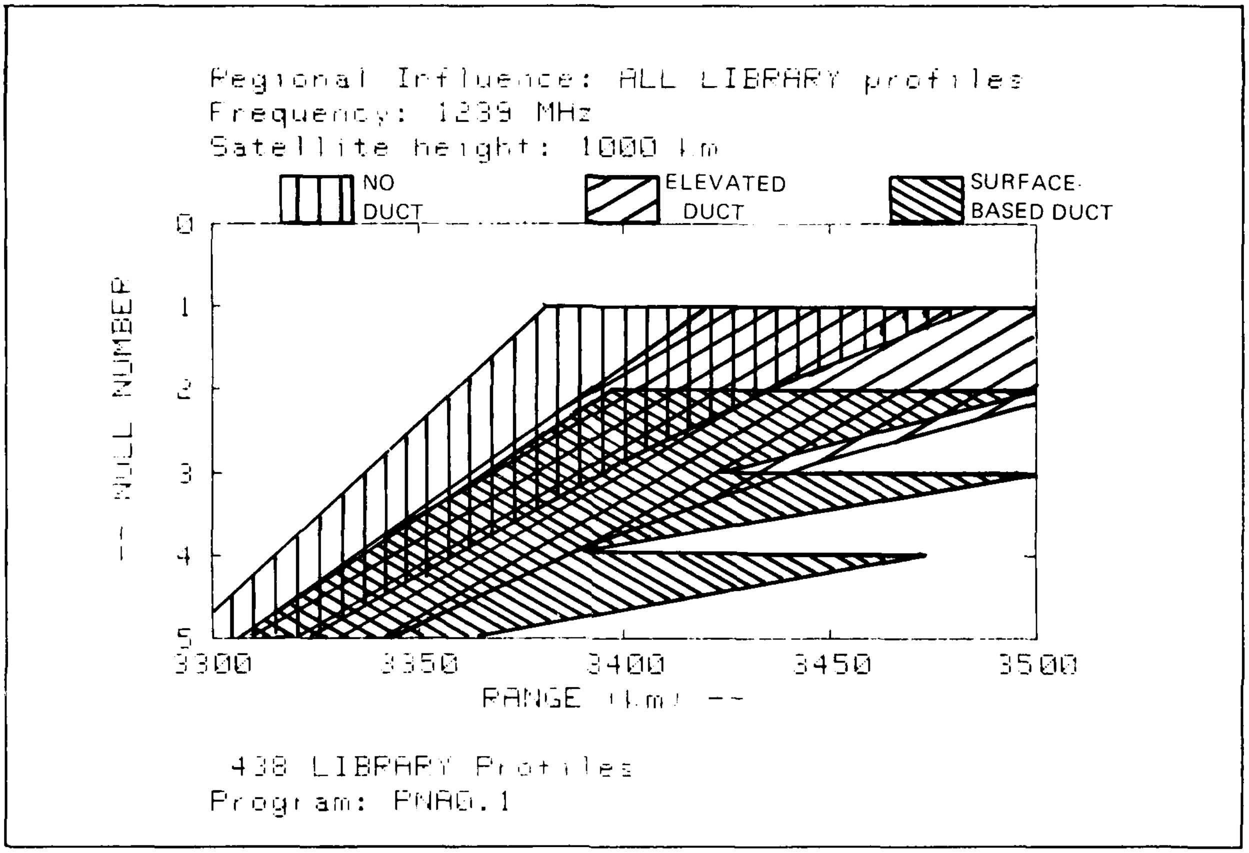

Figure 4. Nonducting, elevated duct, and surface-based duct regimes for library profiles.

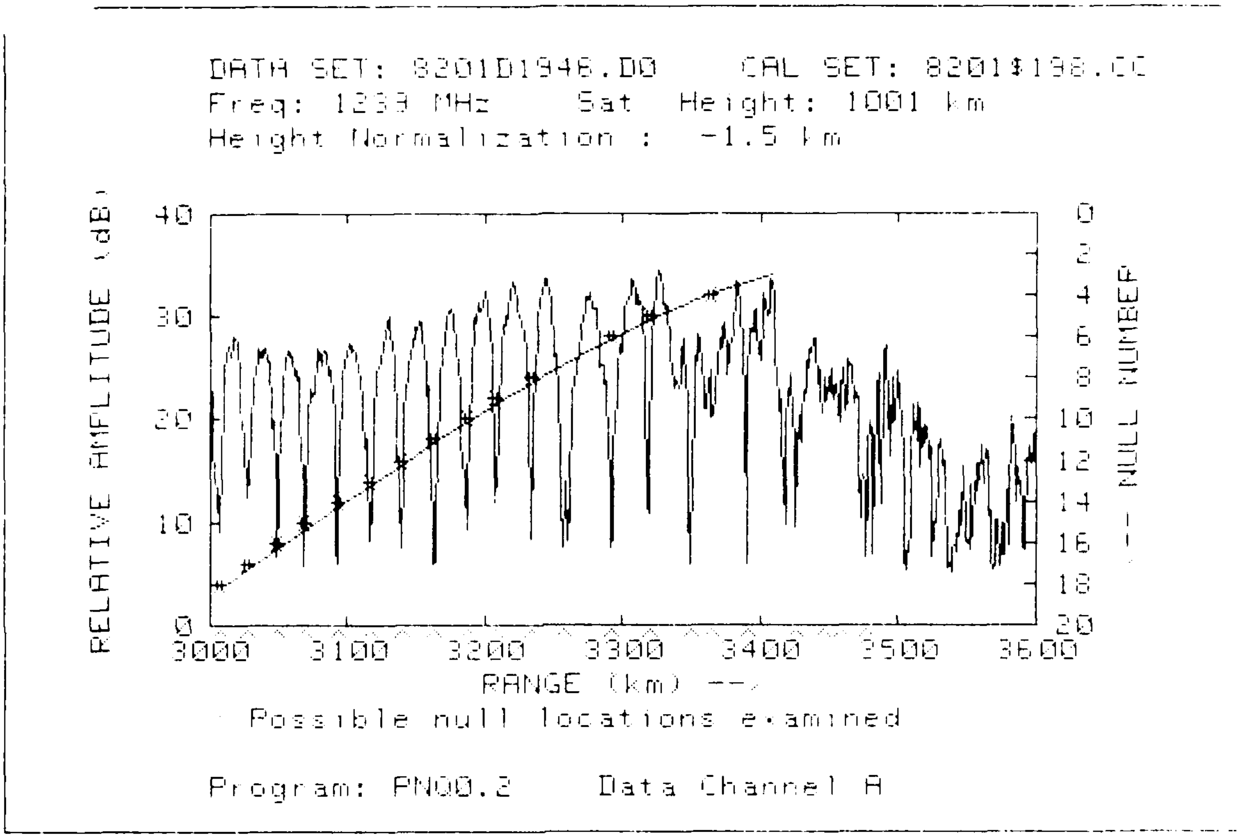

Possible null ranges examined:

2845.5	2847.5	2862.5	2882.5	2901.5	2902.5	2921.5	2940.5
2966.5	2983.5	3006.5	3027.5	3048.5	3068.5	3092.5	3116.5
3139.5	3162.5	3186.5	3207.5	3232.5	3256.5	3291.5	3318.5
3348.5	3364.5	3389.5	3425.5	3444.5	3457.5	3476.5	

NULL	..COMPUTED... ALPHA mrad	RANGE km	.OBS. RANGE km	DIFF km
20	69.2	2969.6	2966.5	3.1
18	62.2	3011.6	3006.5	5.1
16	55.3	3054.5	3049.5	5.9
14	48.4	3098.4	3092.5	5.9
12	41.5	3143.9	3139.5	4.3
10	34.5	3191.2	3186.5	4.7
8	27.6	3241.4	3232.5	8.8
6	20.7	3296.0	3291.5	4.4
4	13.7	3361.3	3364.5	-3.2
2				

NULL	..COMPUTED... ALPHA mrad	RANGE km	.OBS. RANGE km	DIFF km
19	65.7	2990.5	2983.5	7.0
17	58.8	3032.9	3027.5	5.4
15	51.8	3076.3	3068.5	7.8
13	44.9	3120.9	3116.5	4.4
11	38.0	3167.3	3162.5	4.7
9	31.1	3215.9	3207.5	8.3
7	24.1	3267.9		
5	17.2	3326.4	3318.5	7.9
3	10.2	3408.6		
1				

Figure 5. 1239 MHz signal received on 20 July 1978 at 1946 GMT.

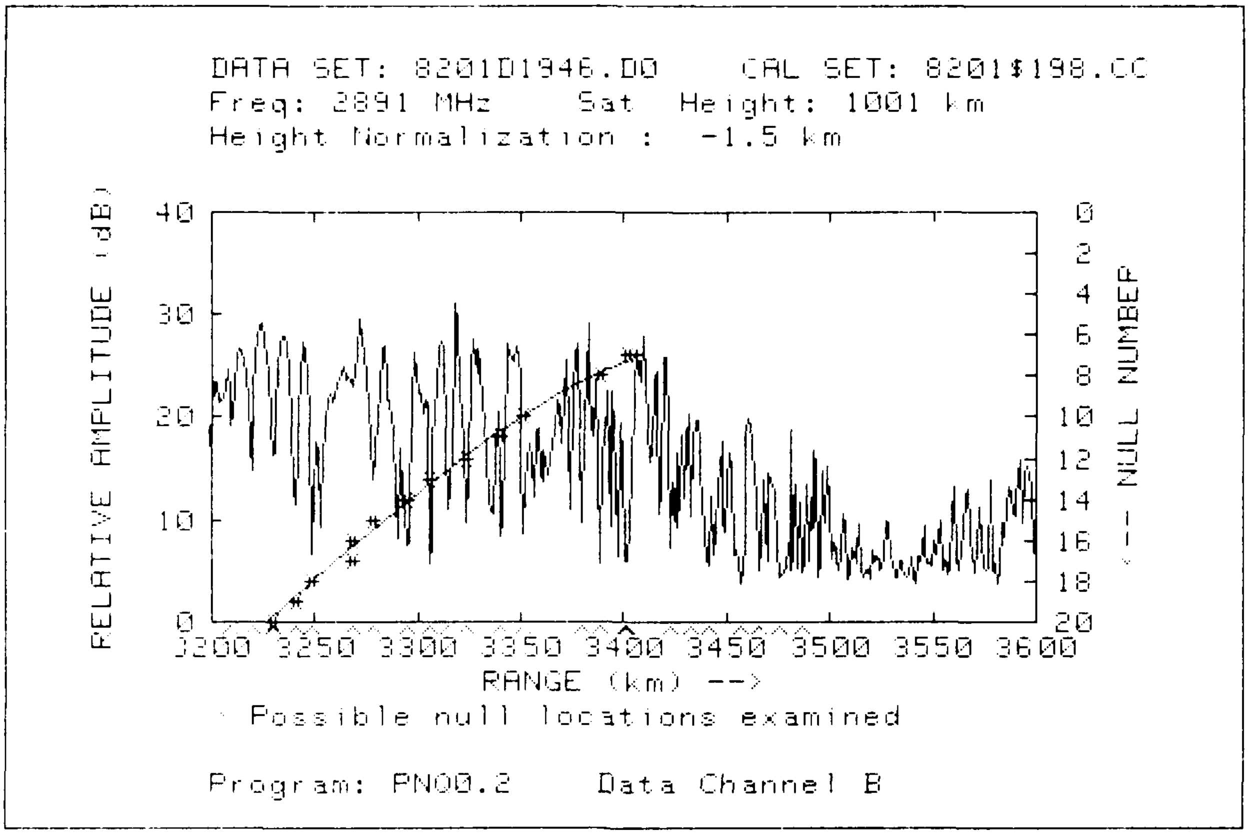

Possible null ranges examined:

2845.5	2854.5	2866.5	2876.5	2888.5	2889.5	2895.5	2901.5
2909.5	2917.5	2924.5	2931.5	2938.5	2952.5	2959.5	2967.5
2977.5	2987.5	2998.5	3006.5	3012.5	3027.5	3041.5	3042.5
3052.5	3062.5	3089.5	3098.5	3099.5	3109.5	3118.5	3122.5
3131.5	3139.5	3150.5	3158.5	3169.5	3179.5	3190.5	3198.5
3209.5	3219.5	3229.5	3240.5	3248.5	3268.5	3278.5	3294.5
3305.5	3314.5	3323.5	3340.5	3351.5	3379.5	3388.5	3400.5
3401.5	3422.5	3432.5	3441.5	3456.5	3465.5	3475.5	3486.5

NULL	..COMPUTED... ALPHA mrad	RANGE km	.OBS. RANGE km	DIFF km	NULL	..COMPUTED... ALPHA mrad	RANGE km	.OBS. RANGE km	DIFF km
20	29.6	3226.7	3229.5	-2.9	19	28.1	3237.7	3240.5	-2.9
18	26.6	3248.8	3248.5	.3	17	25.1	3260.2	3268.5	-8.4
16	23.6	3271.8	3268.5	3.3	15	22.1	3283.7	3278.5	5.2
14	20.7	3296.0	3294.5	1.4	13	19.2	3308.7	3305.5	3.1
12	17.7	3321.9	3323.5	-1.6	11	16.2	3335.8	3340.5	-4.7
10	14.7	3350.7	3351.5	-.9	9	13.2	3366.9		
8	11.7	3385.4	3388.5	-3.2	7	10.2	3408.6	3401.5	7.1
6					5				
4					3				
2					1				

Figure 6. 2891 MHz signal received on 20 July 1978 at 1946 GMT.

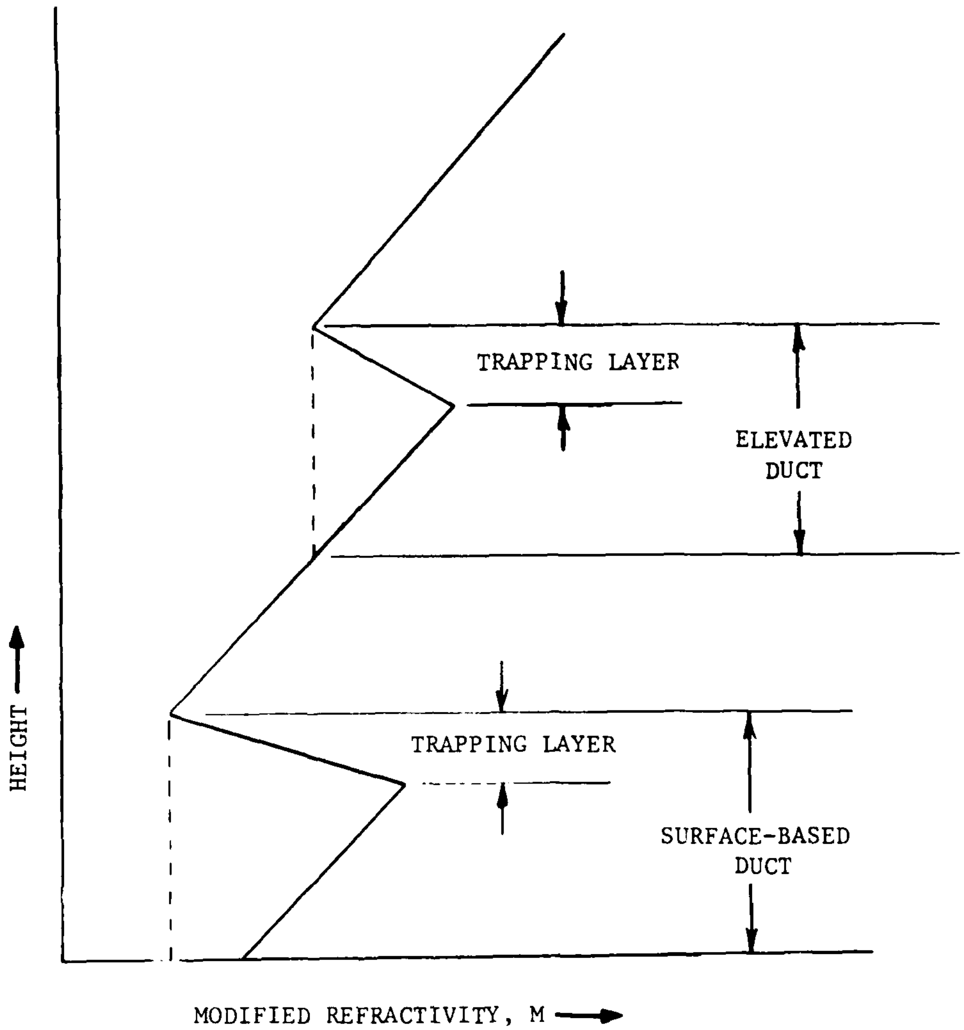

Figure 7. Plot of modified refractivity versus height, showing ducting regions.

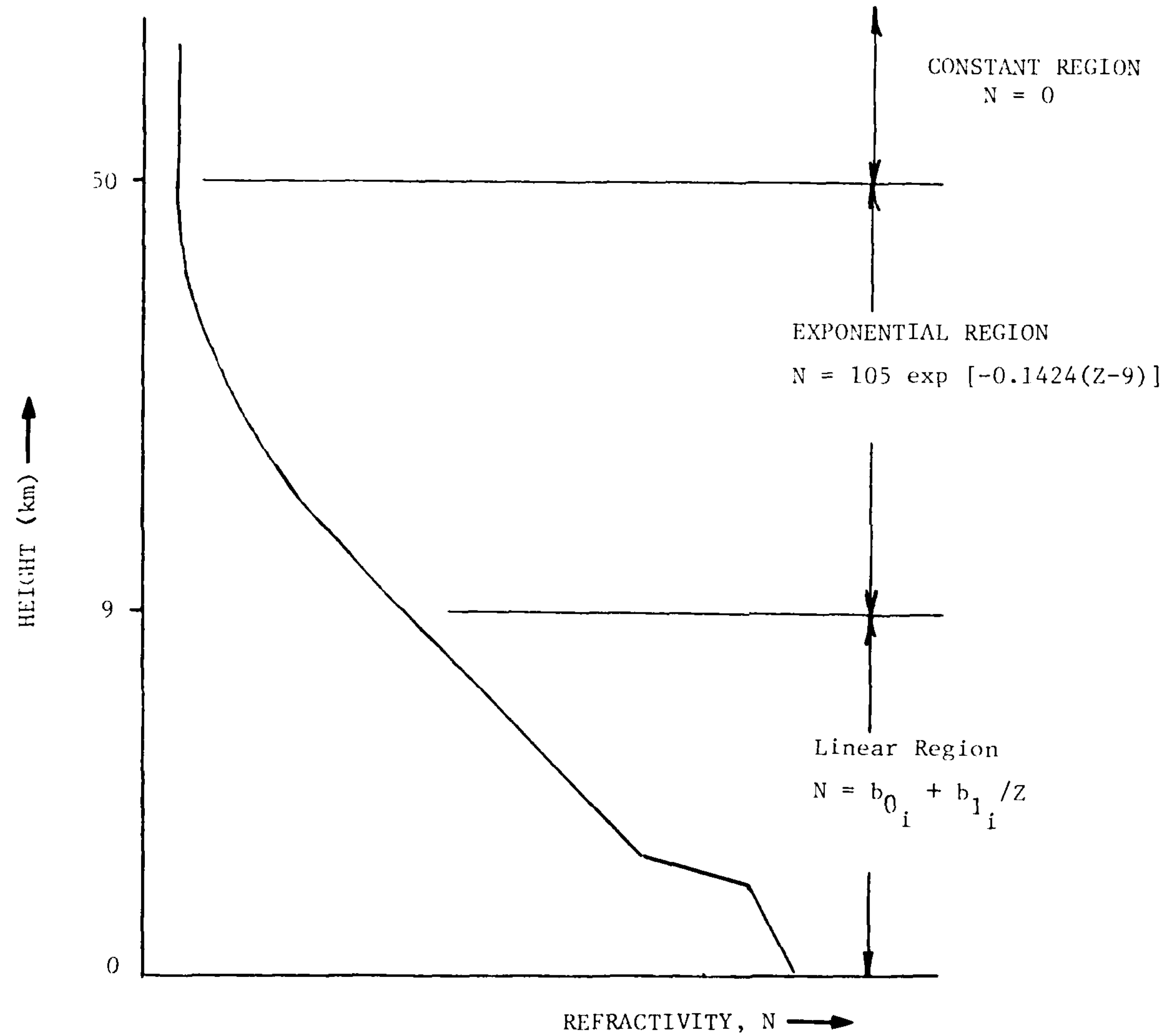

Figure 8. Atmospheric refractivity model.

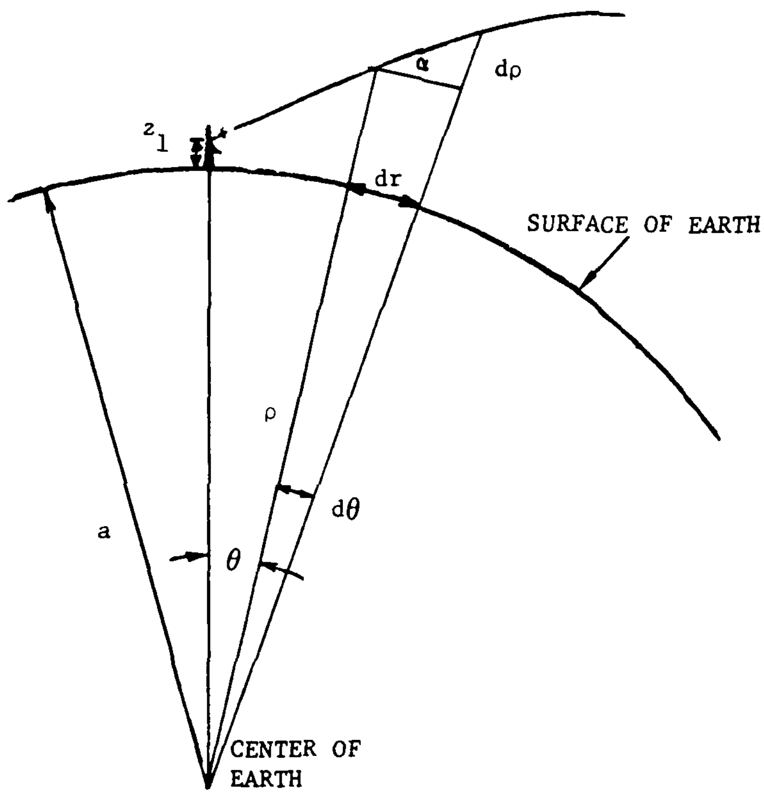

Figure 9. Path of a ray in a vertical plane through the receiver.

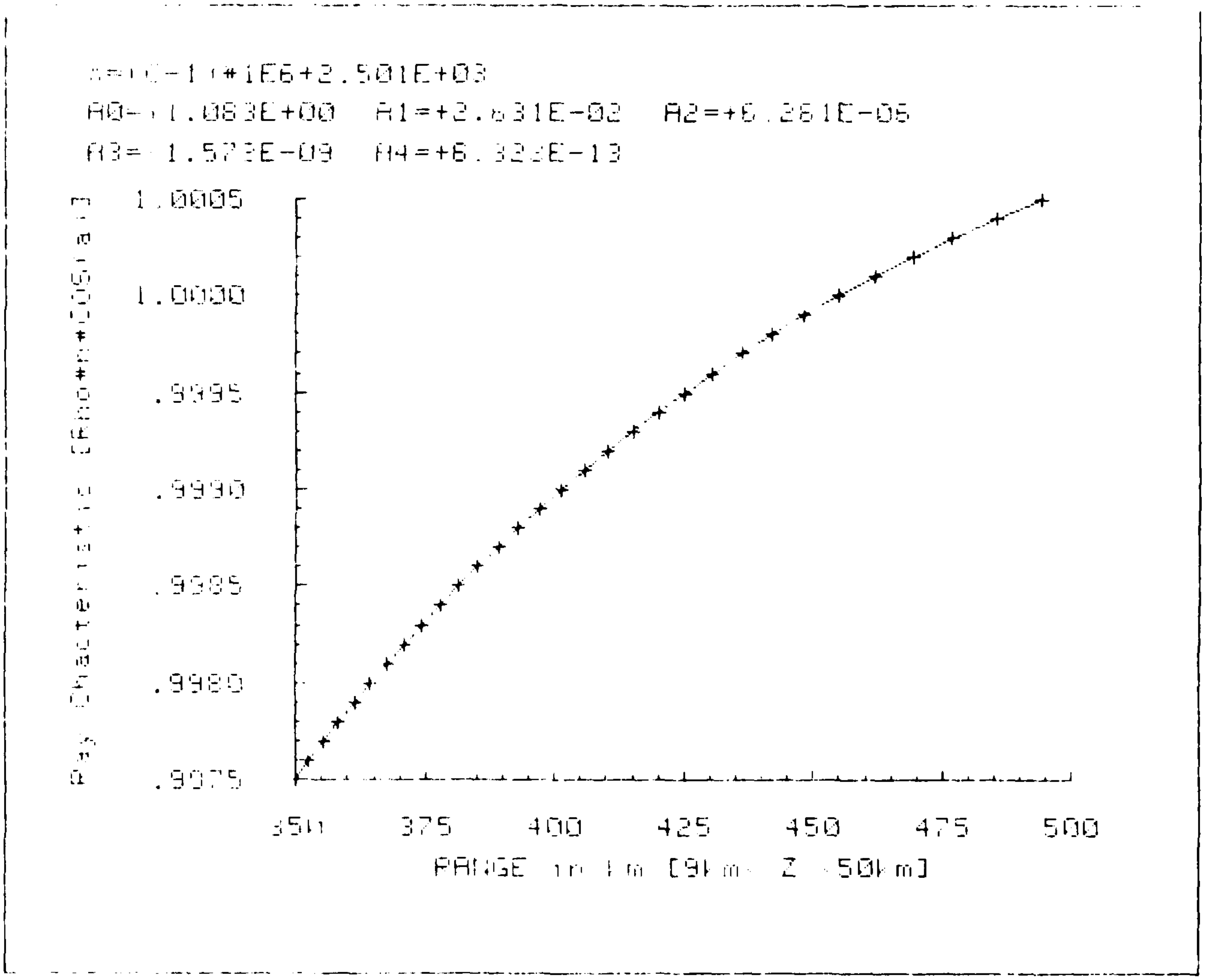

Figure 10. Ground range as a function of n_o cos θ_o for 9 to 50 km altitude.

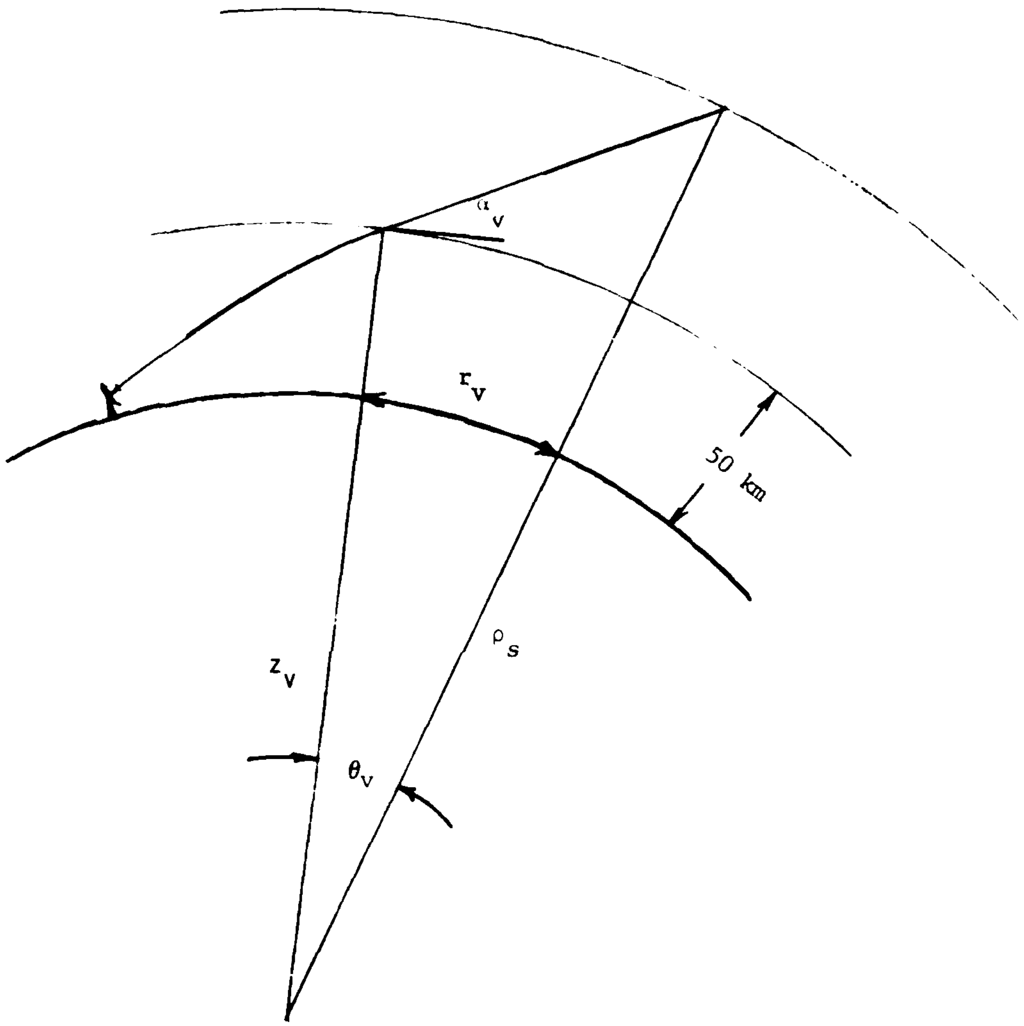

Figure 11. Geometrical representation of ray path for altitudes in excess of 50 km.

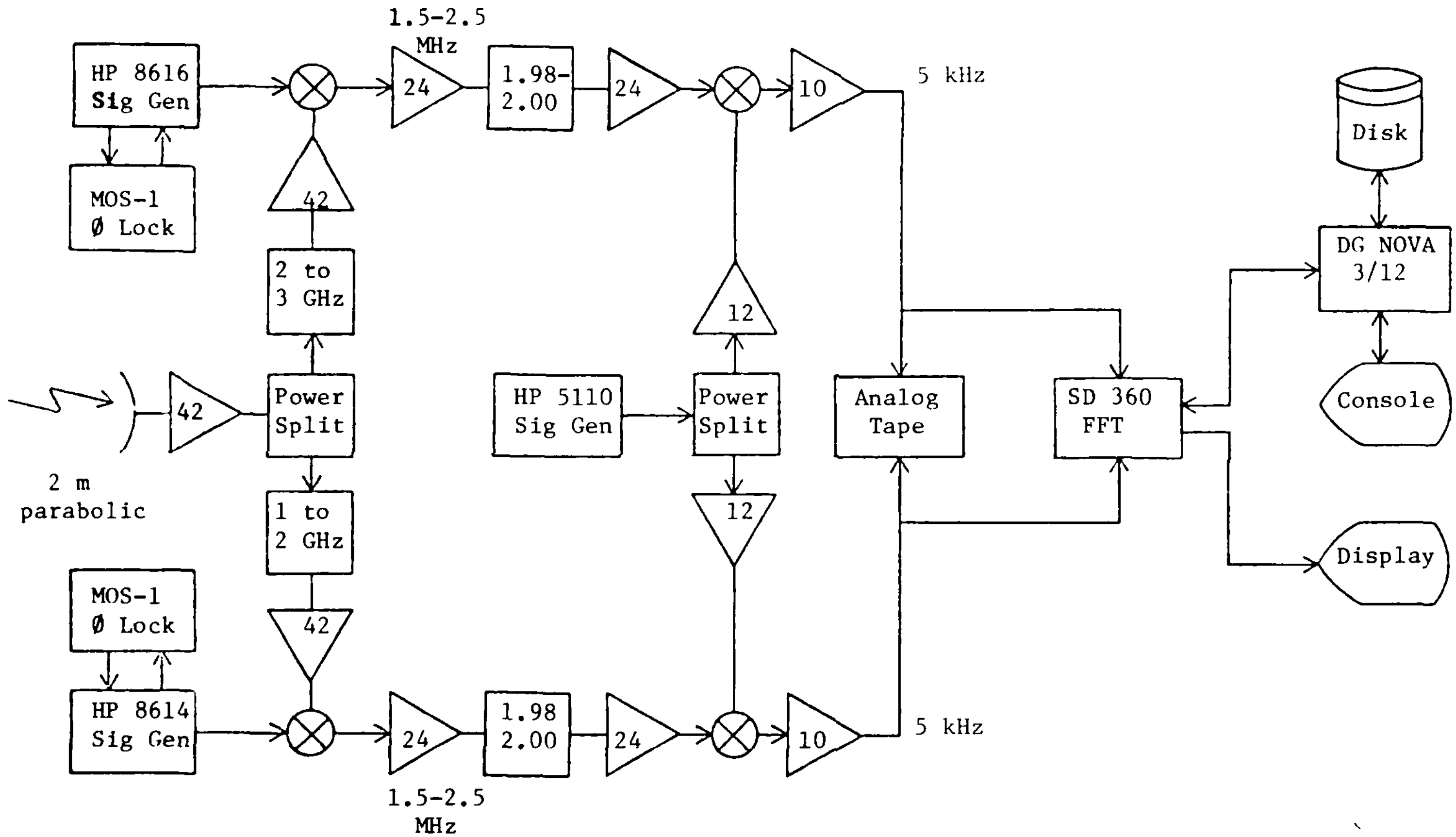

Figure 12. Block diagram of PRISM receiver.

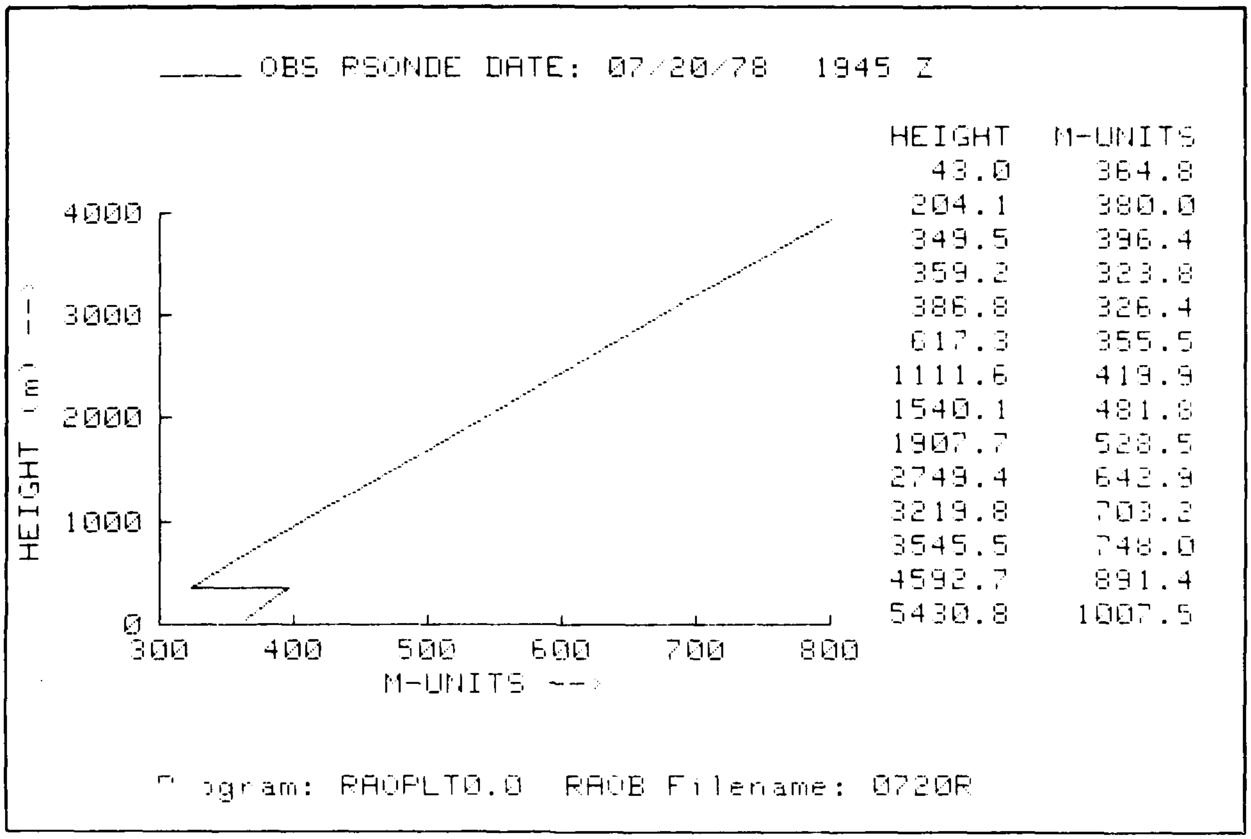

Figure 13. Observed profile, 20 July at 1945 GMT.

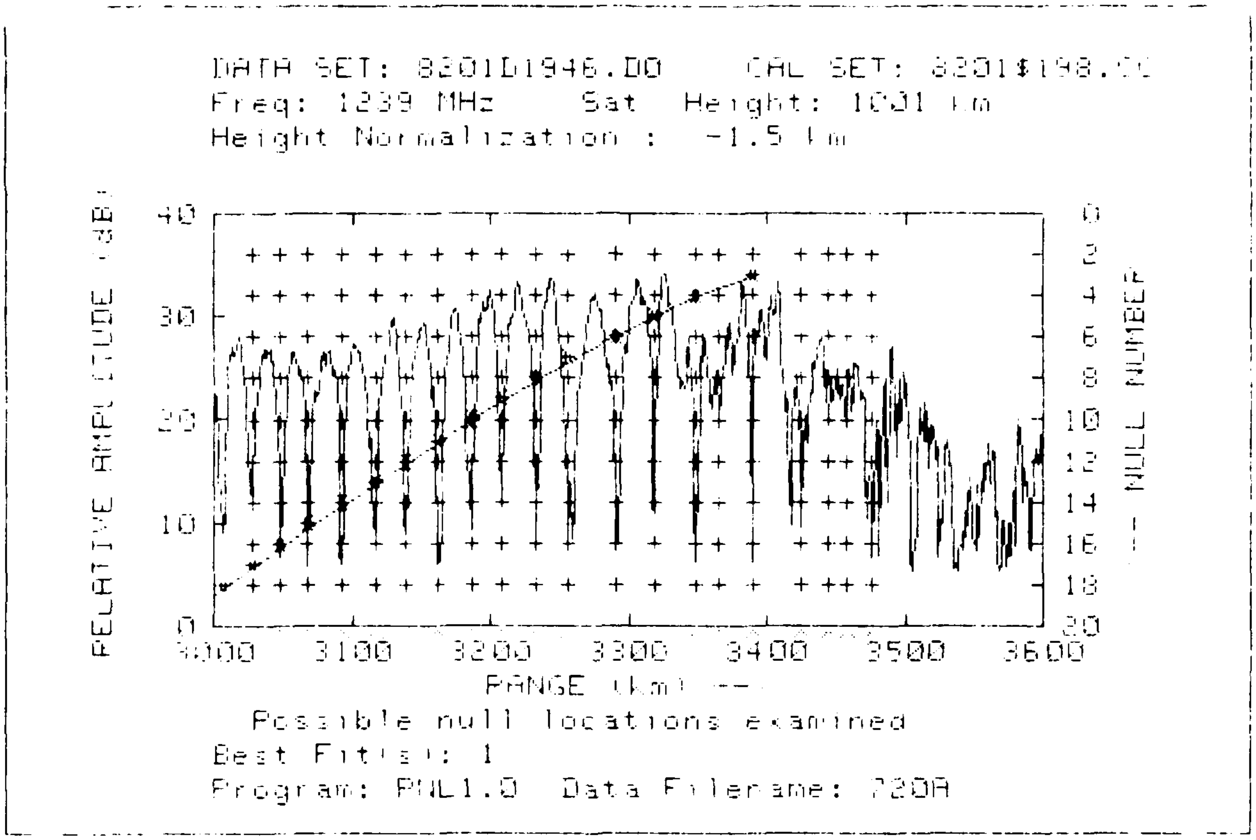

Figure 14. 1239 MHz signal, 20 July at 1946 GMT.

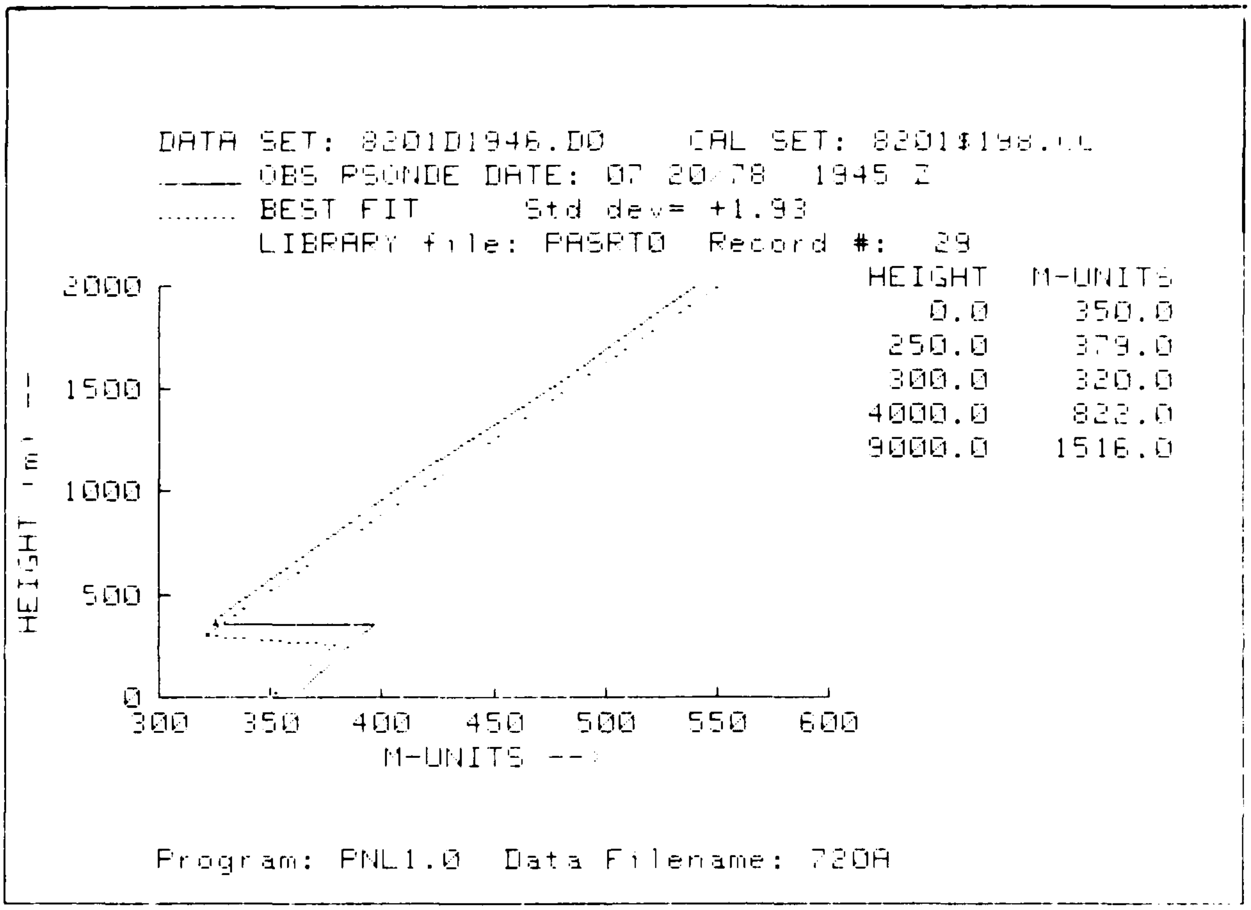

Figure 15. Inferred profile, 1239 MHz.

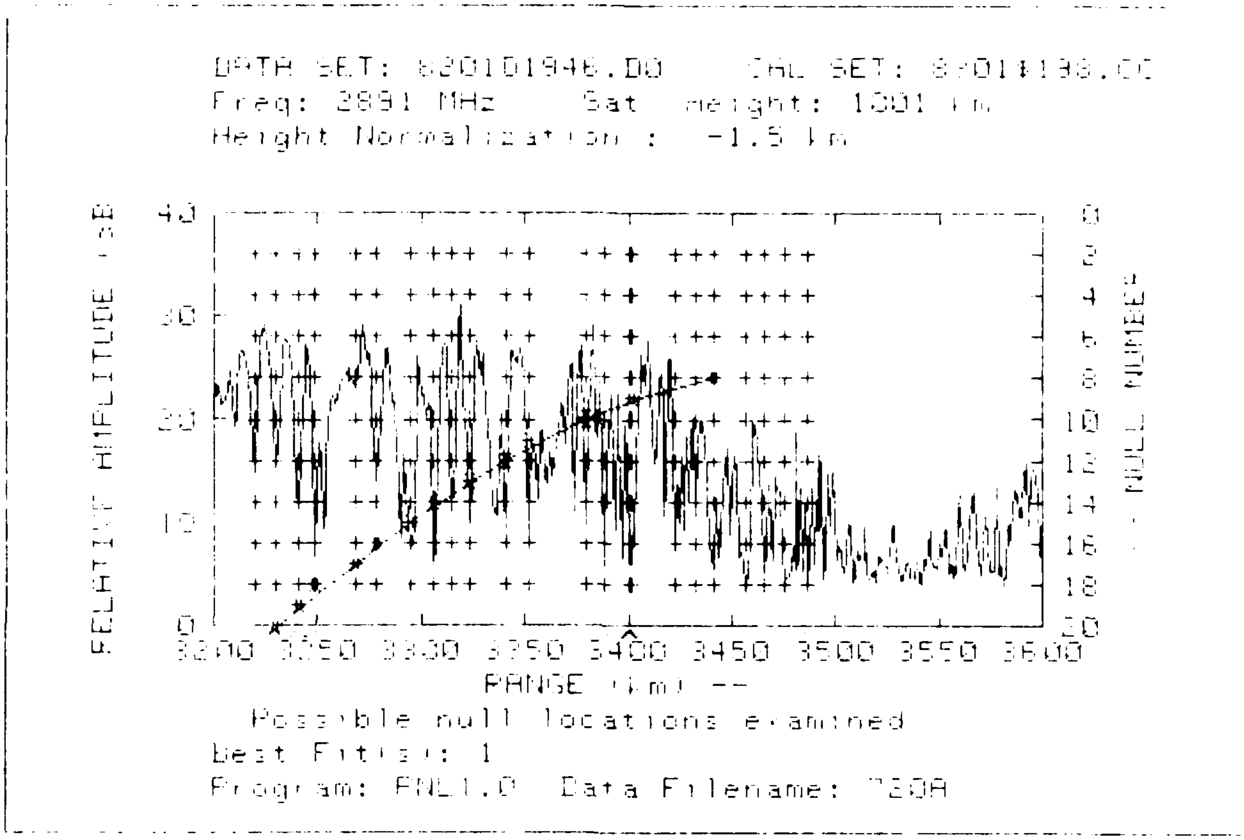

Figure 16. 2891 MHz signal, 20 July at 1946 GMT.

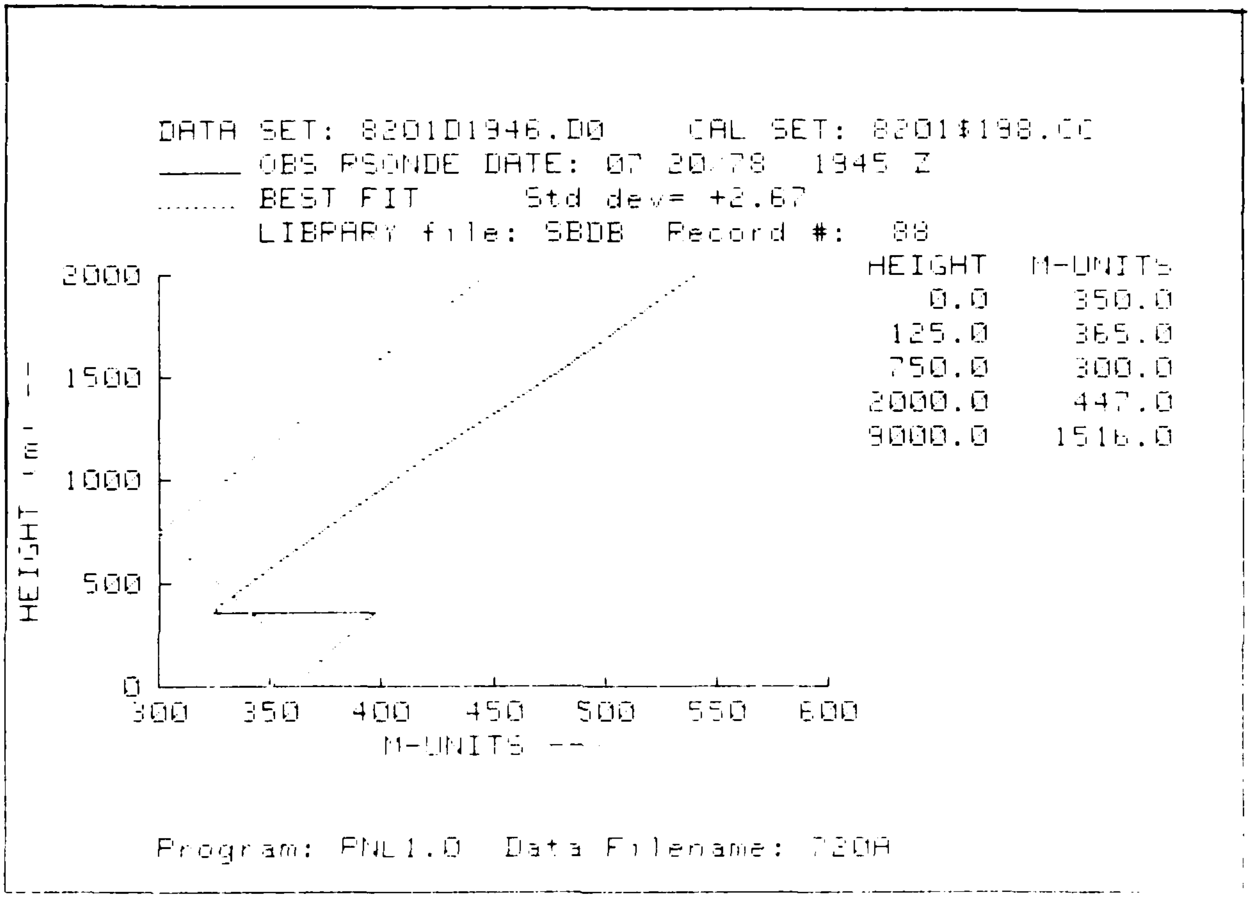

Figure 17. Inferred profile, 2891 MHz.

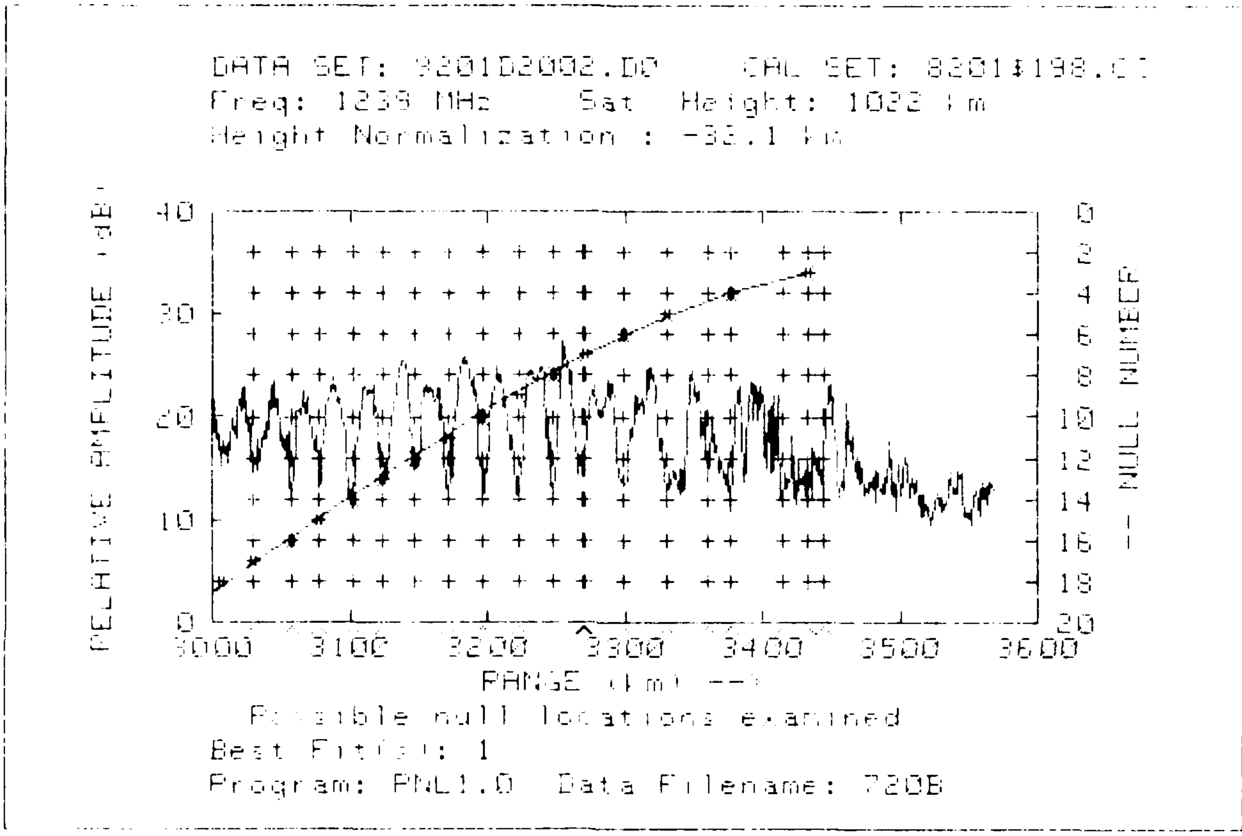

Figure 18. 1239 MHz signal, 20 July at 2002 GMT.

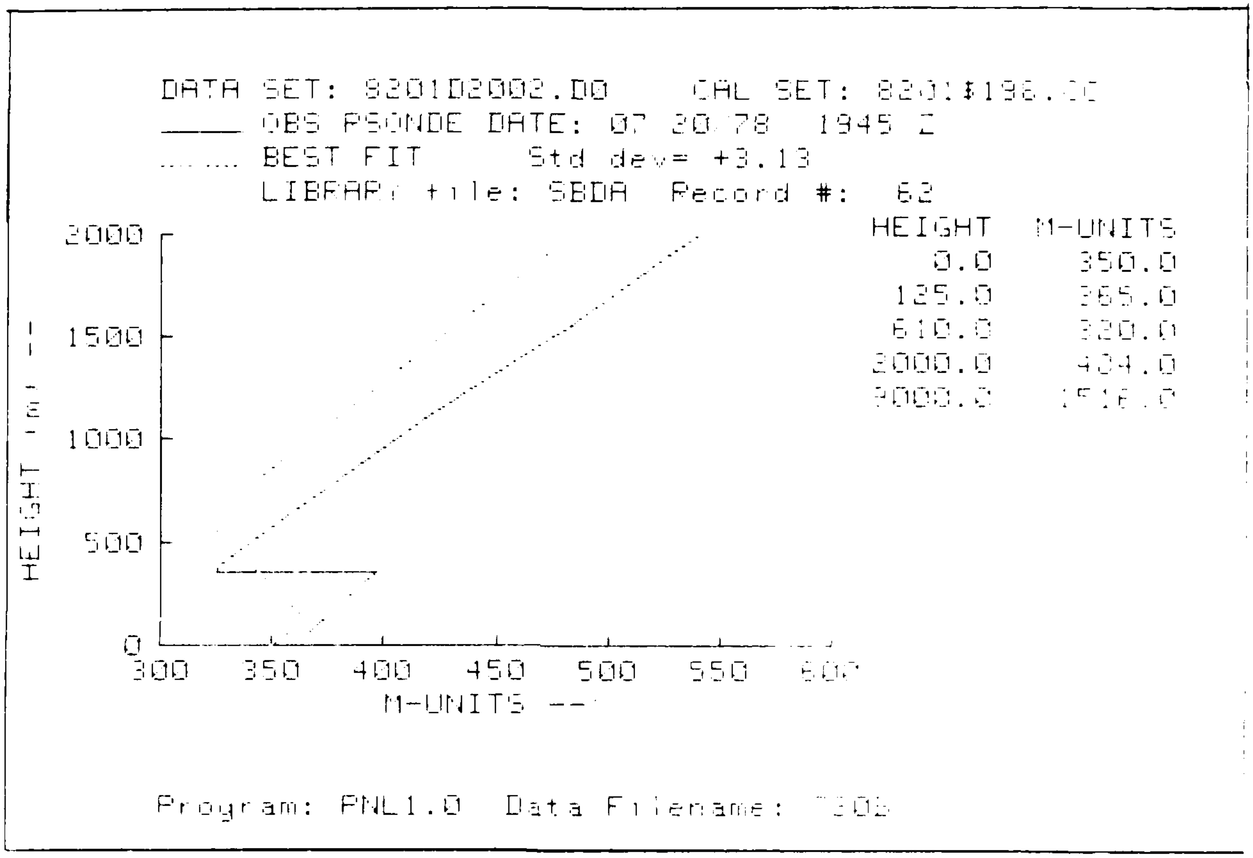

Figure 19. Inferred profile, 1239 MHz.

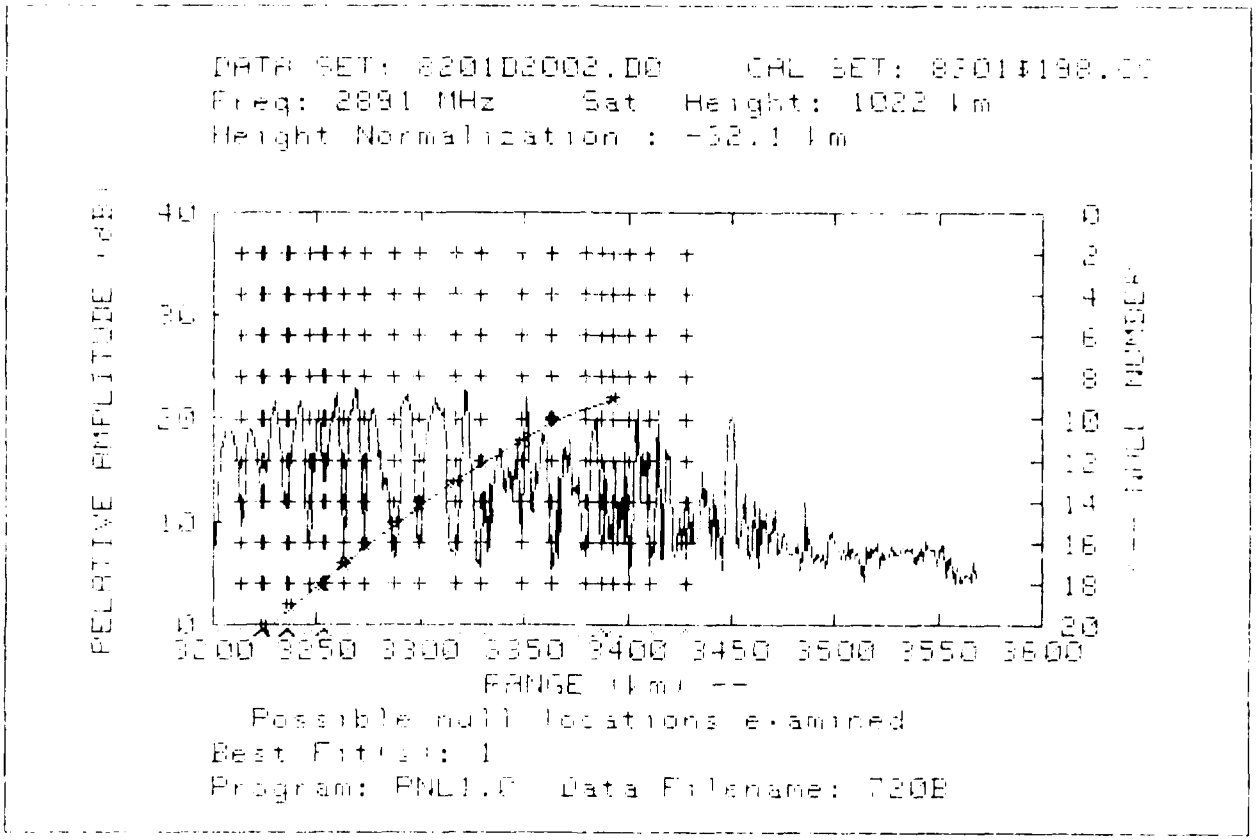

Figure 20. 2891 MHz signal, 20 July at 2002 GMT.

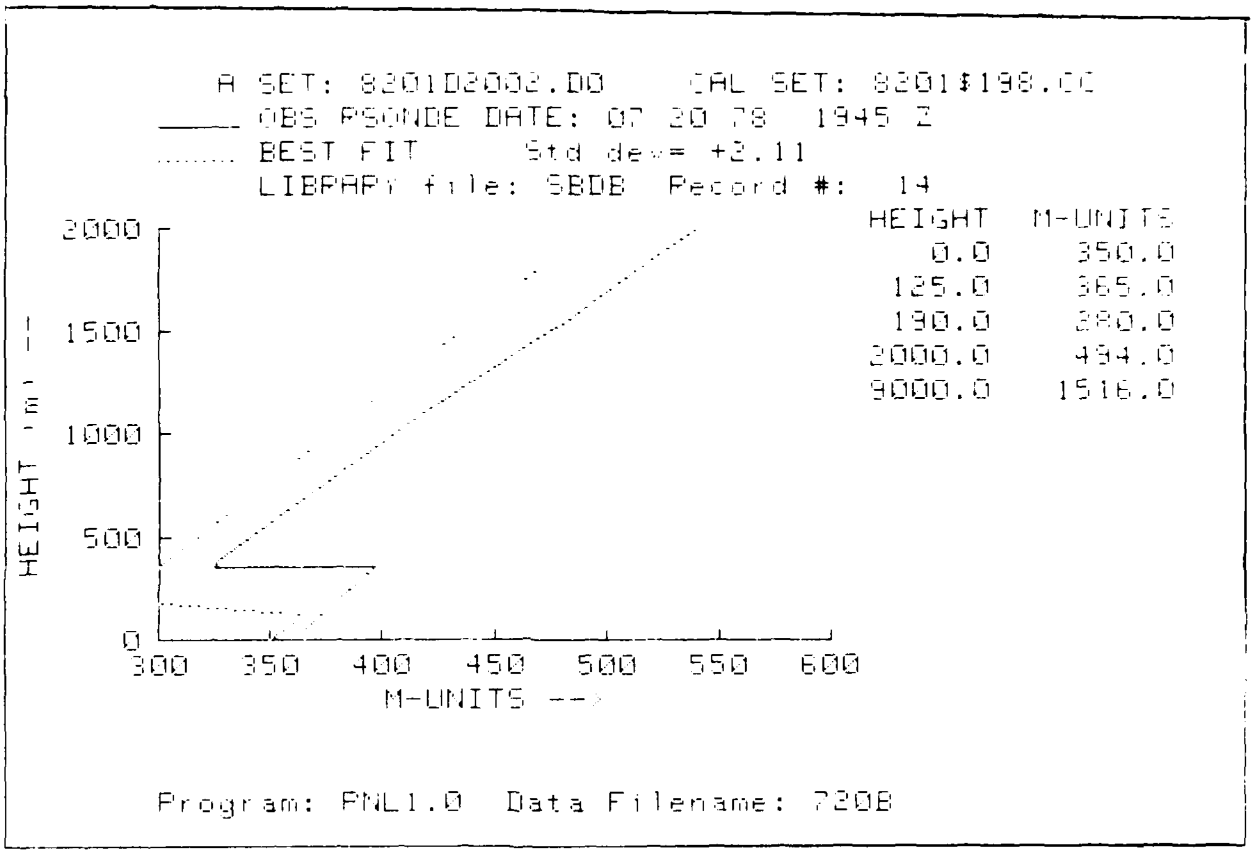

Figure 21. Inferred profile, 2891 MHz.

OBS RSONDE 07/28/78 2000 Z

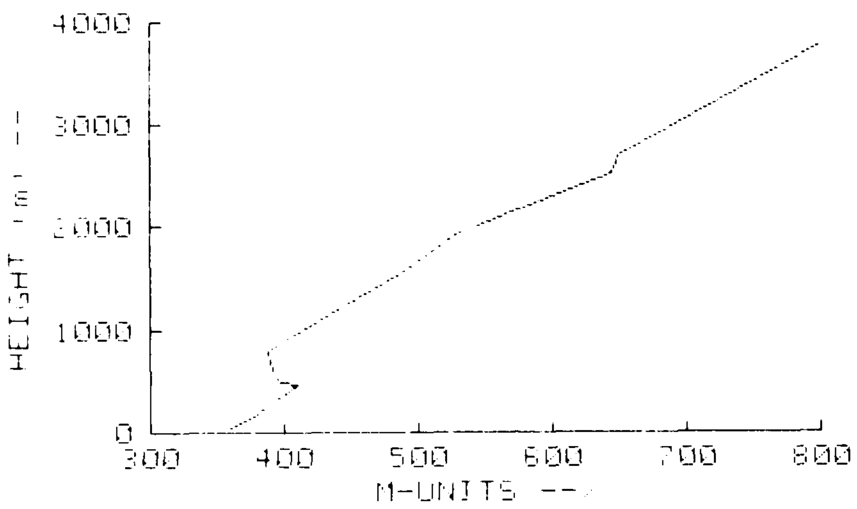

HEIGHT	M-UNITS
43.0	359.0
133.0	373.8
465.3	410.8
487.8	396.5
593.2	391.3
787.0	388.7
1004.4	413.5
1543.1	486.3
1935.1	529.5
2517.5	644.1
2688.6	648.9
3217.4	723.2
3815.6	807.6
3925.5	829.1

Program: RAOPLT0.0 RAOB Filename: 0728R

Figure 22. Observed profile, 28 July at 2000 GMT.

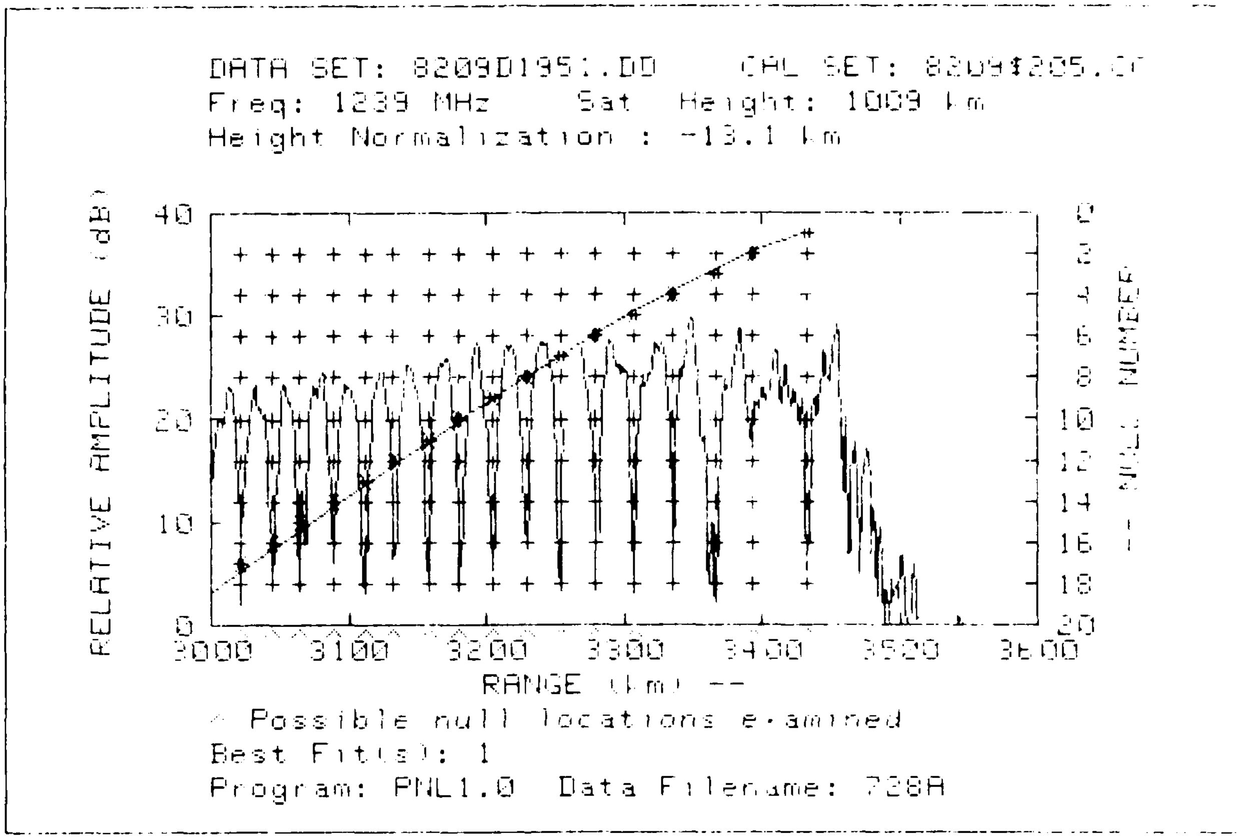

Figure 23. 1239 MHz signal, 28 July at 1951 GMT.

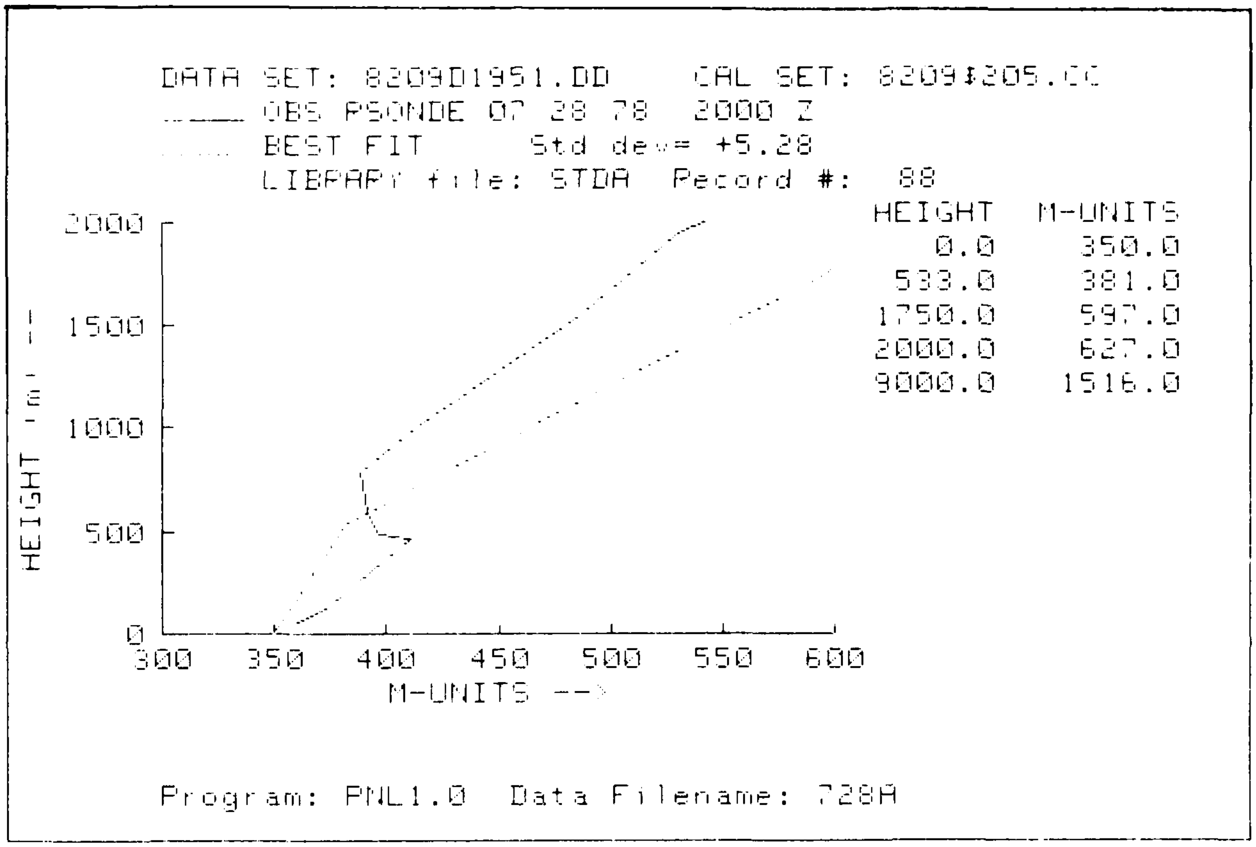

Figure 24. Inferred profile, 1239 MHz.

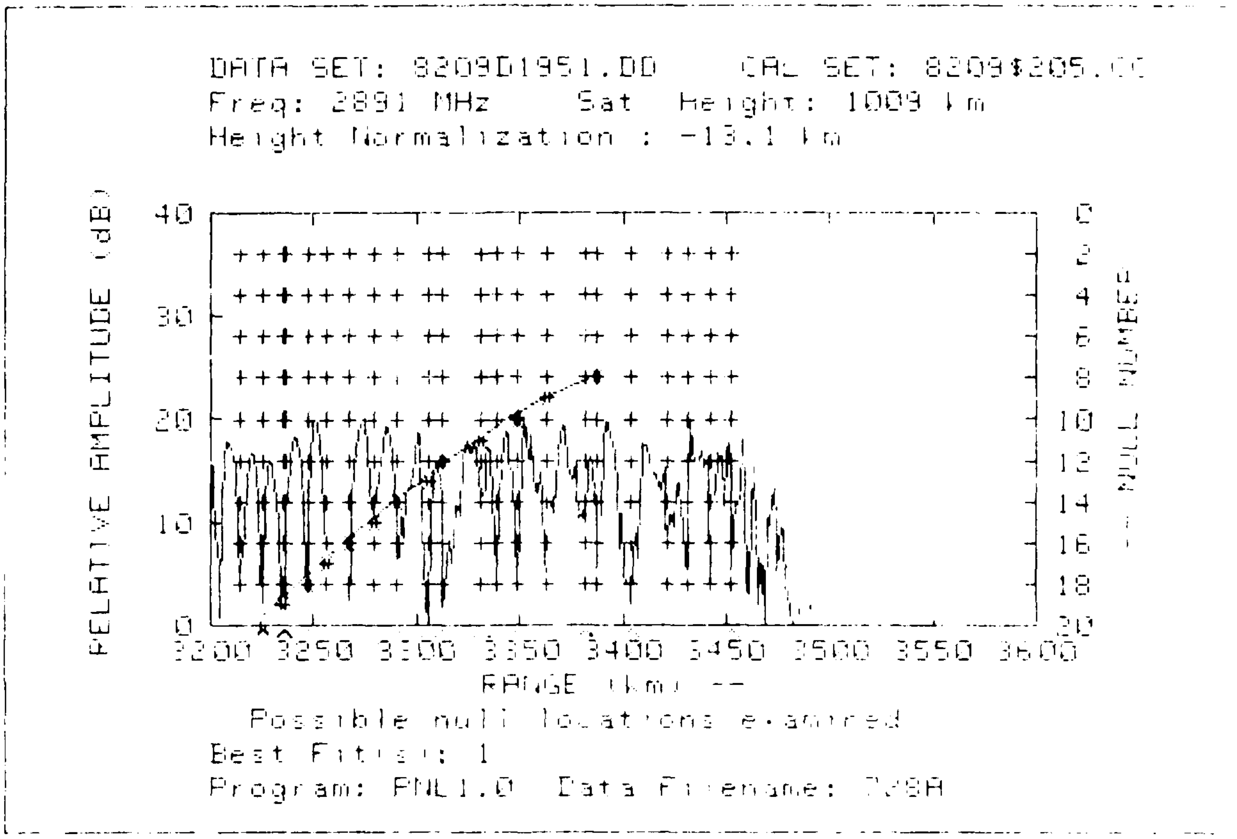

Figure 25. 2891 MHz signal, 28 July at 1951 GMT.

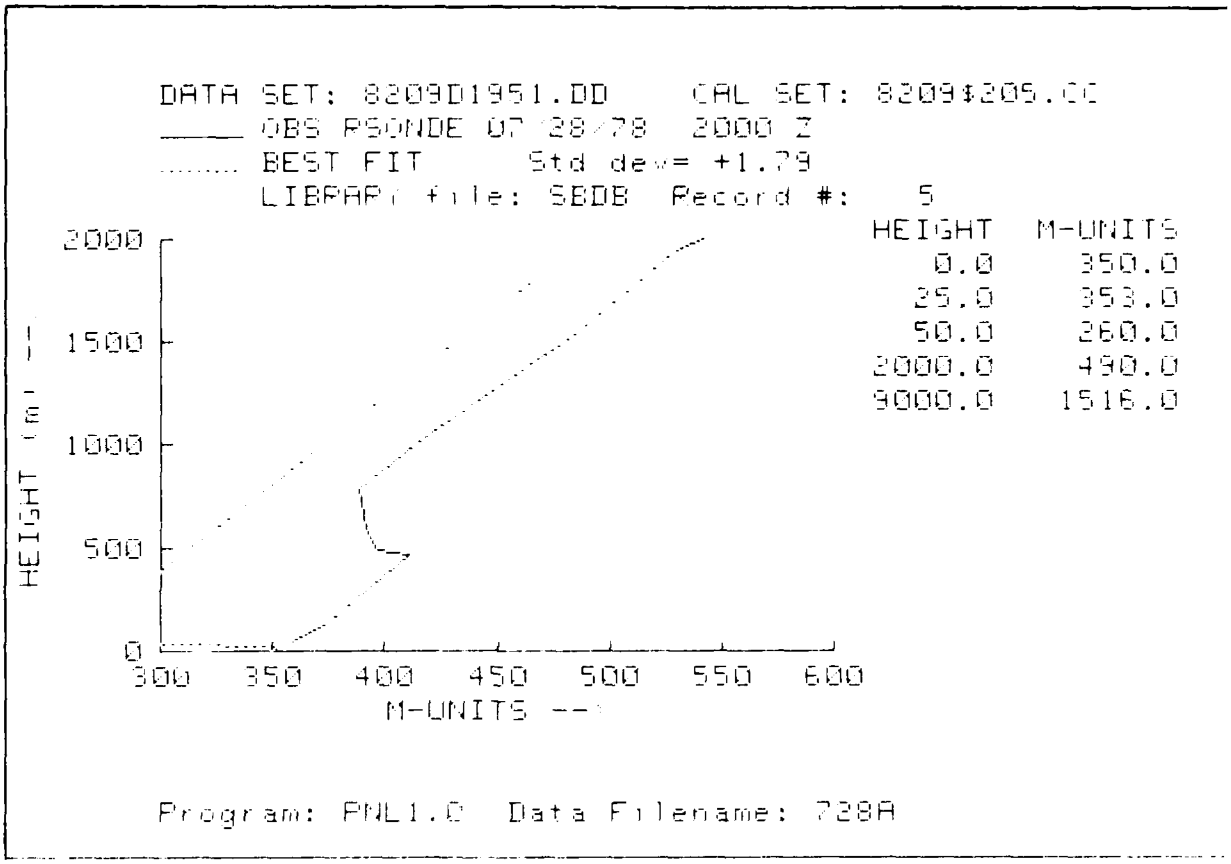

Figure 26. Inferred profile, 2891 MHz.

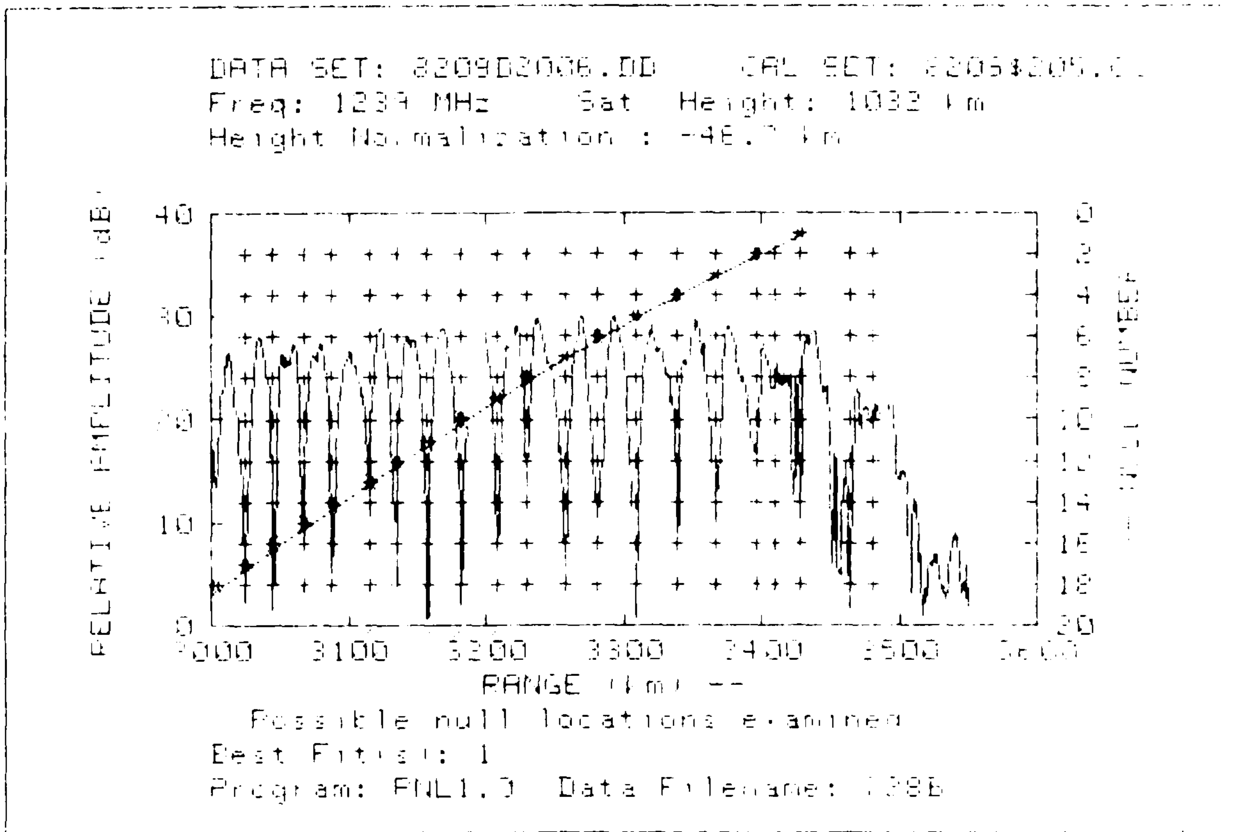

Figure 27. 1239 MHz signal, 28 July at 2006 GMT.

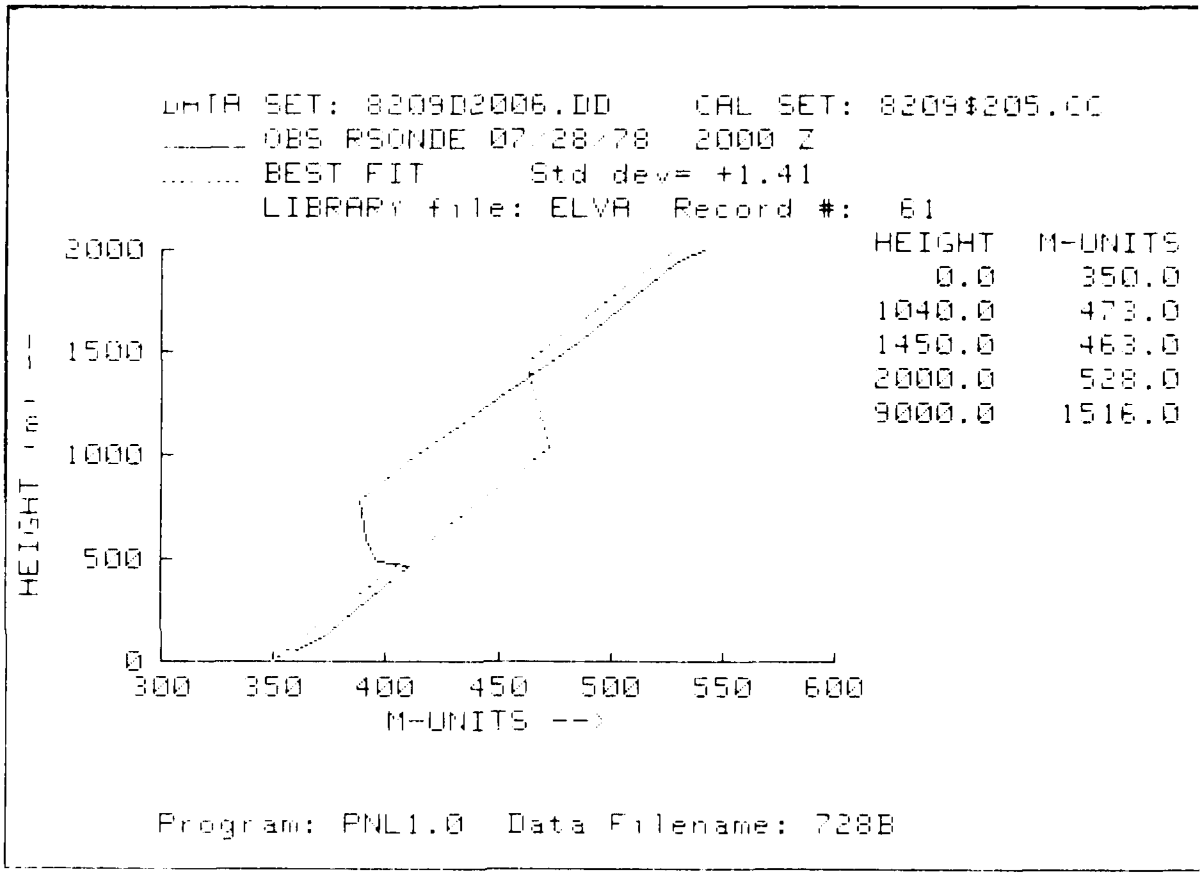

Figure 28. Inferred profile, 1239 MHz.

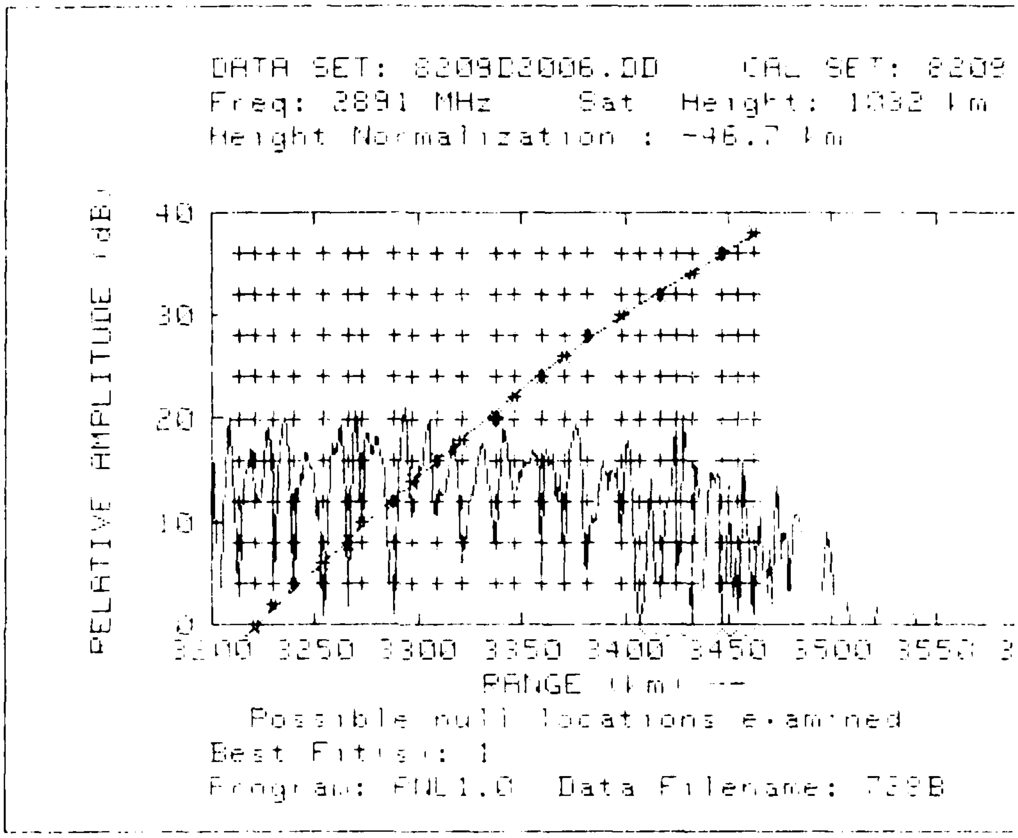

Figure 29. 2891 MHz signal, 28 July at 2006 GMT.

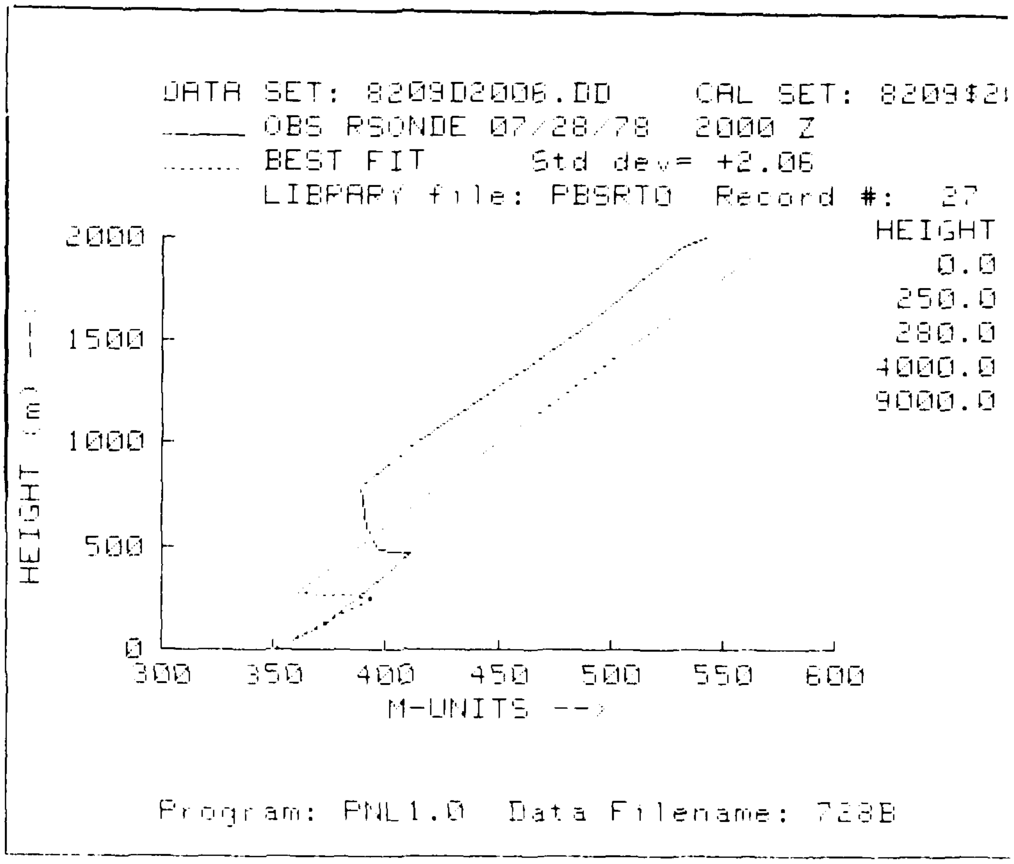

Figure 30. Inferred profile, 2891 MHz.

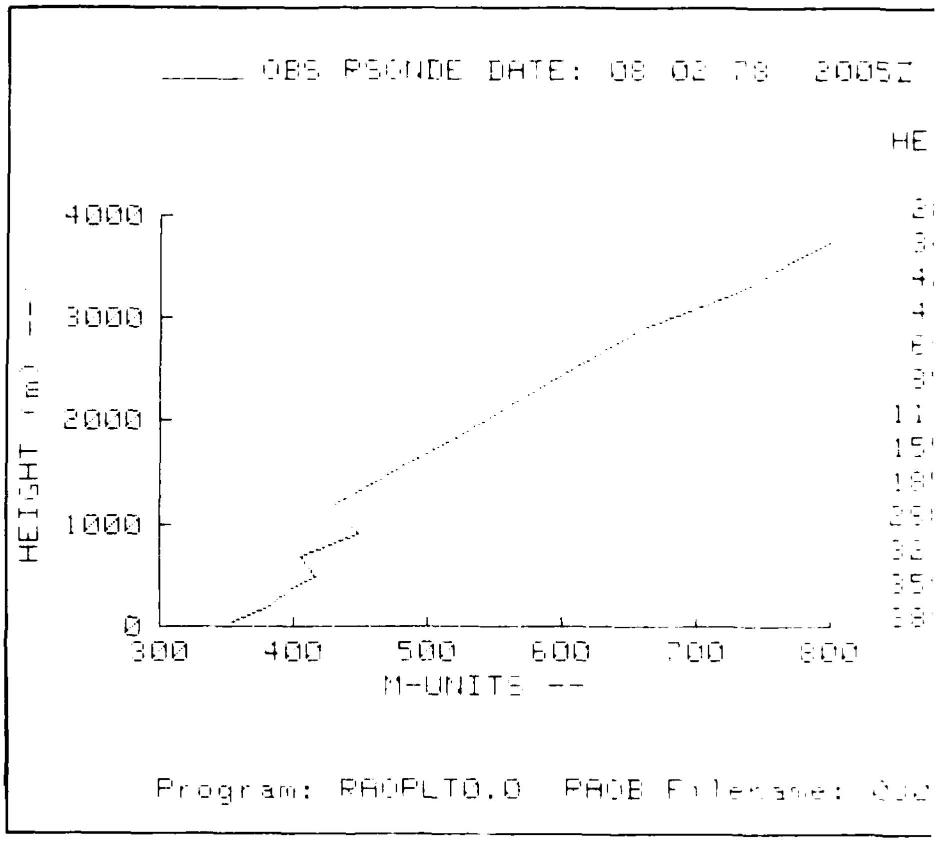

Figure 31. Observed profile, 2 August at 200

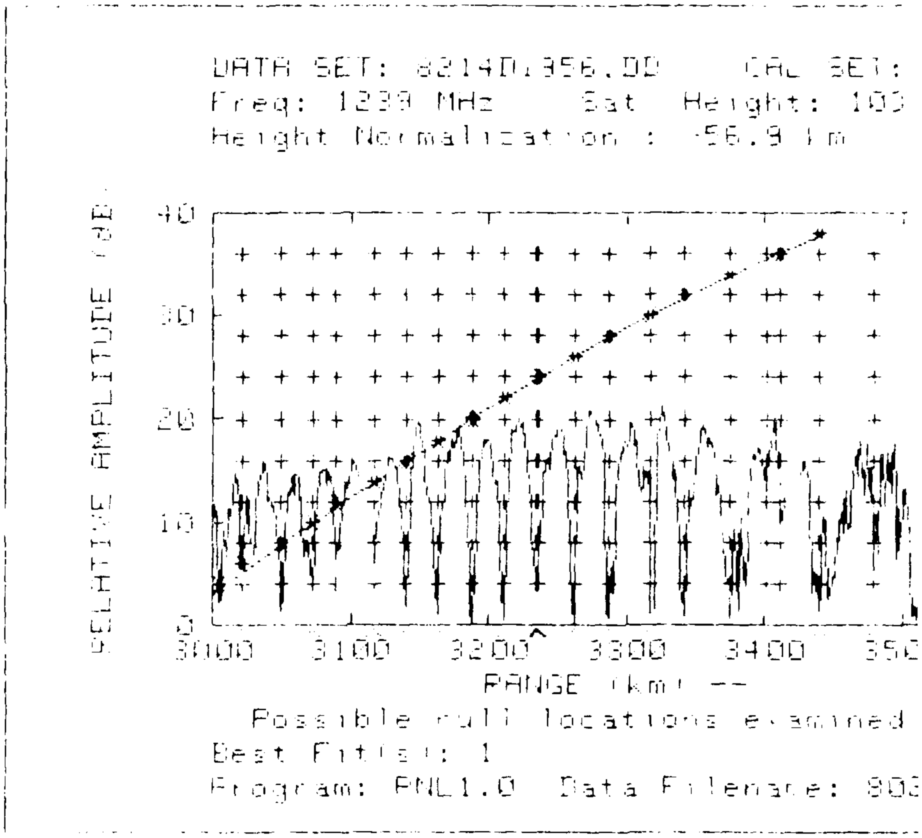

Figure 32. 1239 MHz signal, 2 August at 19

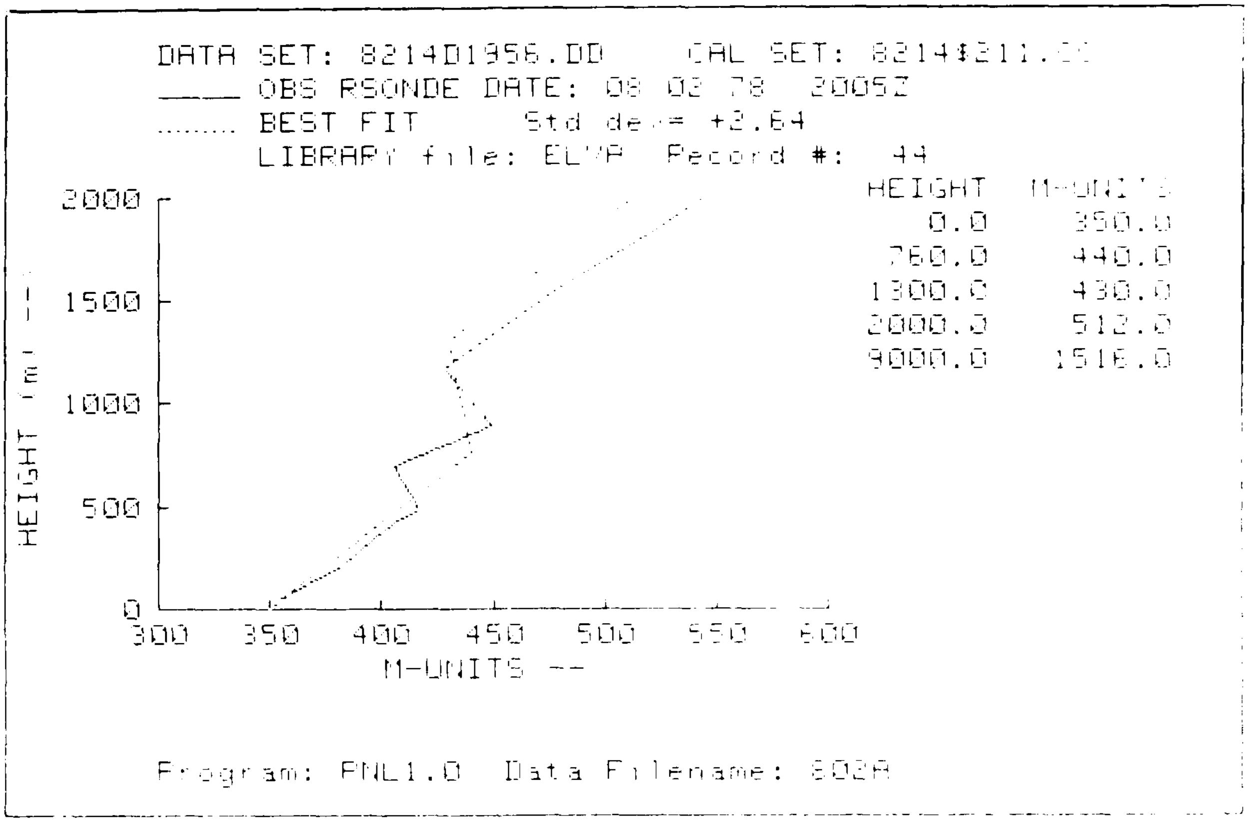

Figure 33. Inferred profile, 1239 MHz.

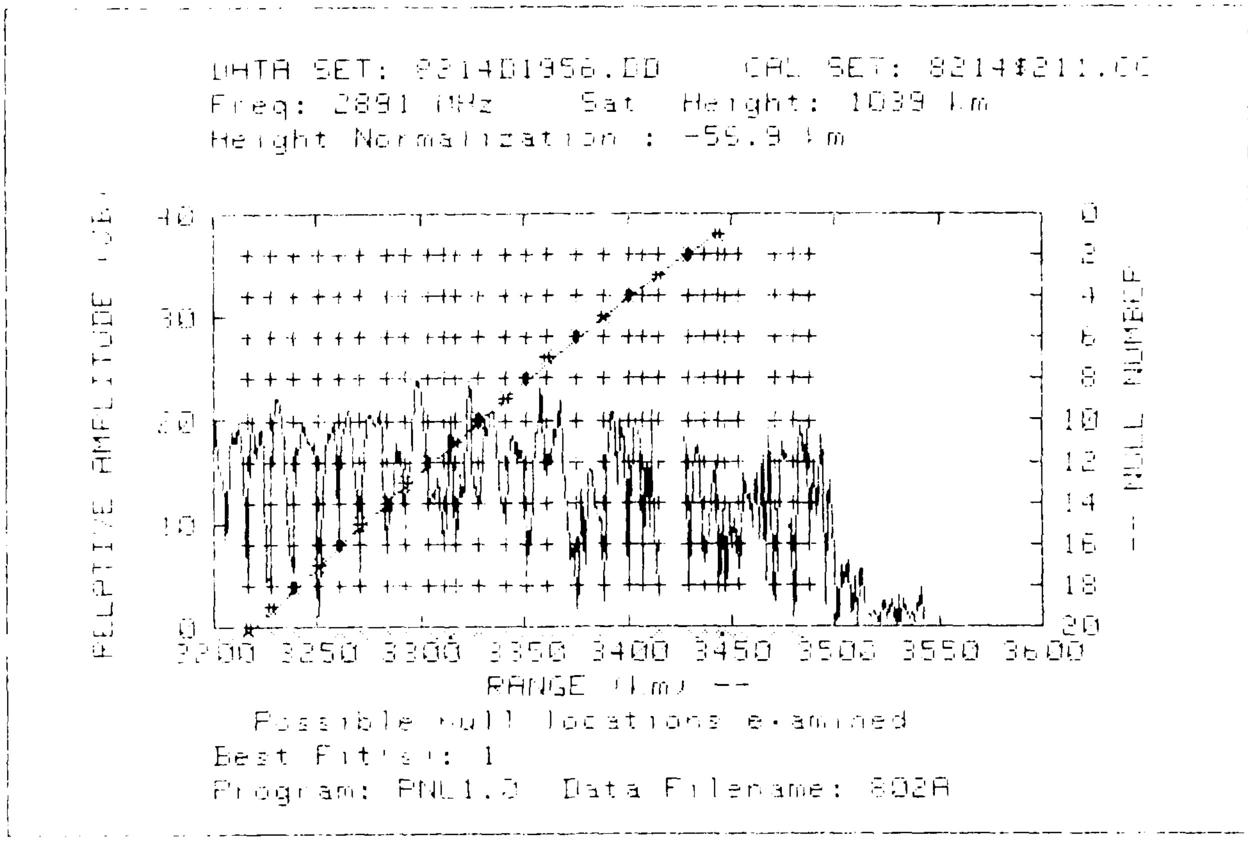

Figure 34. 2891 MHz signal, 2 August at 1956 GMT.

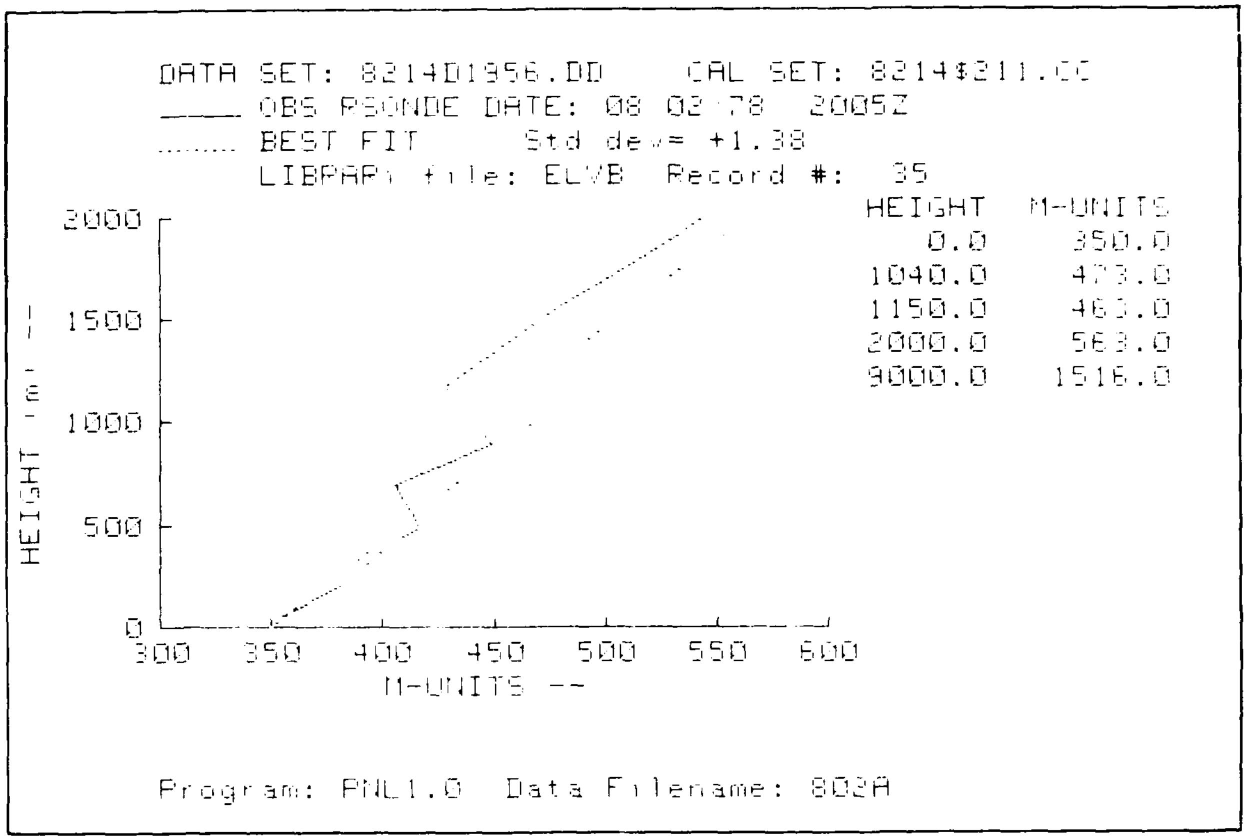

Figure 35. Inferred profile, 2891 MHz.

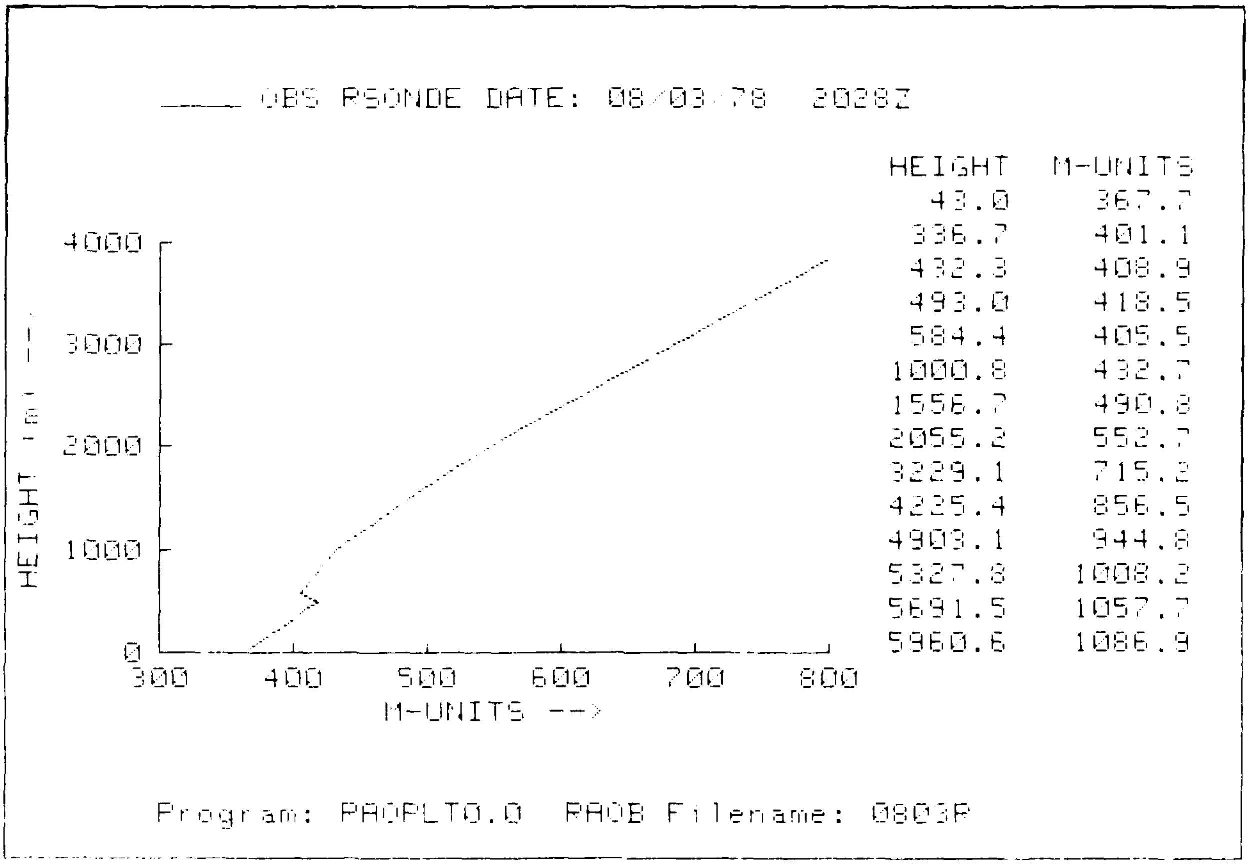

Figure 36. Observed profile, 3 August at 2028 GMT.

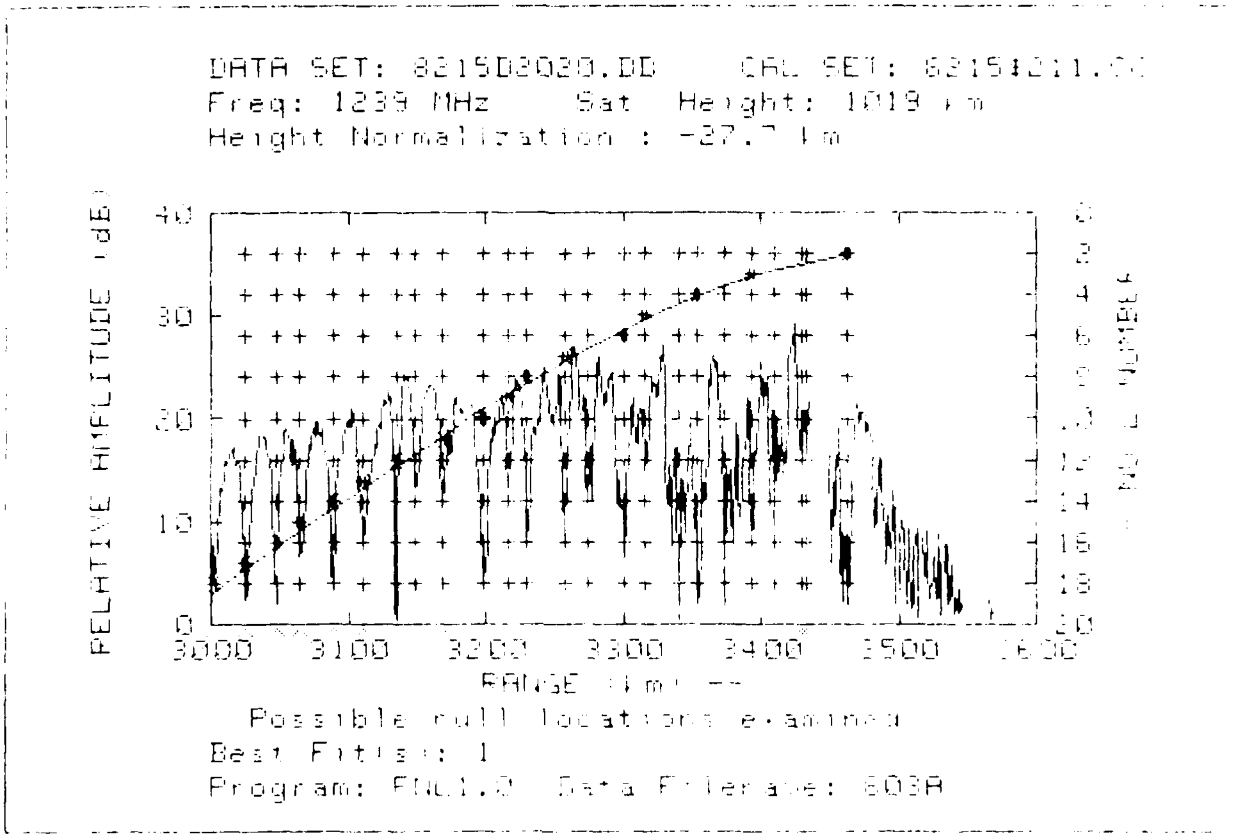

Figure 37. 1239 MHz signal, 3 August at 2020 GMT.

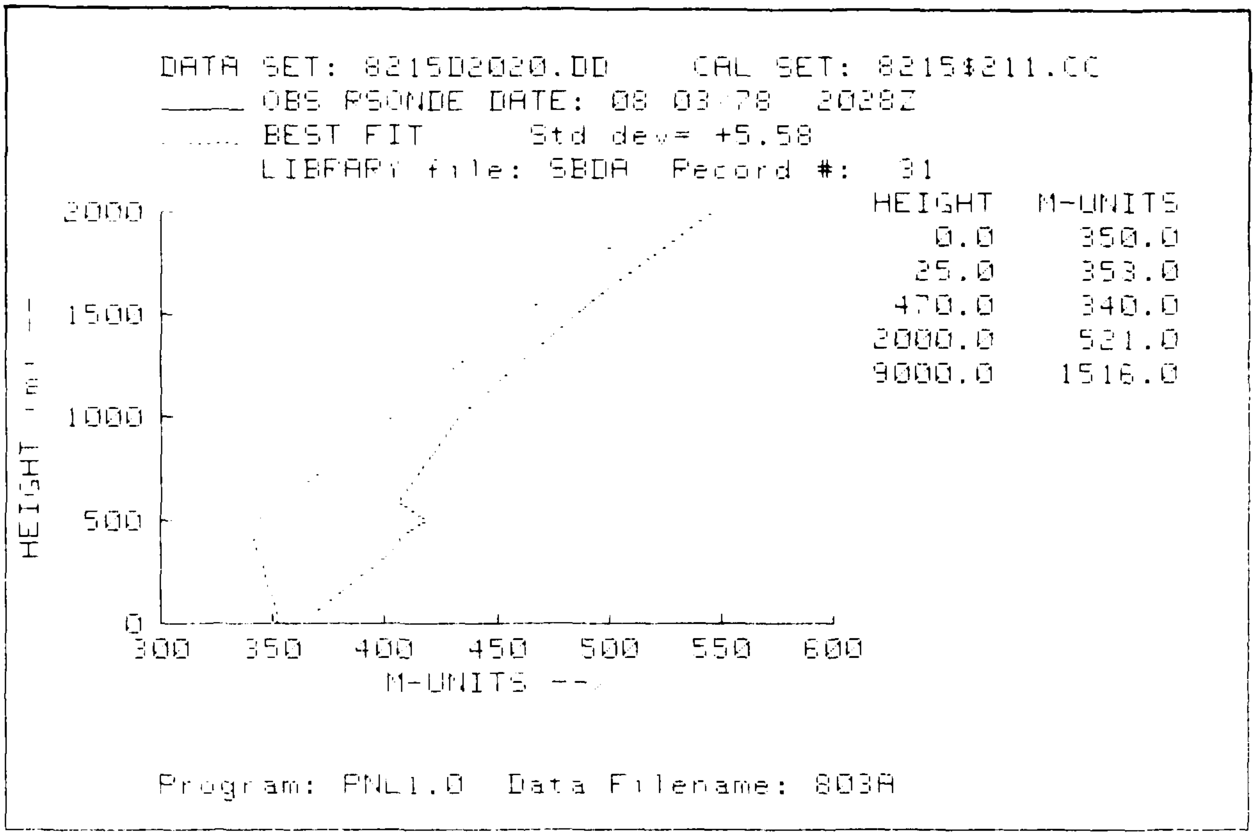

Figure 38. Inferred profile, 1239 MHz.

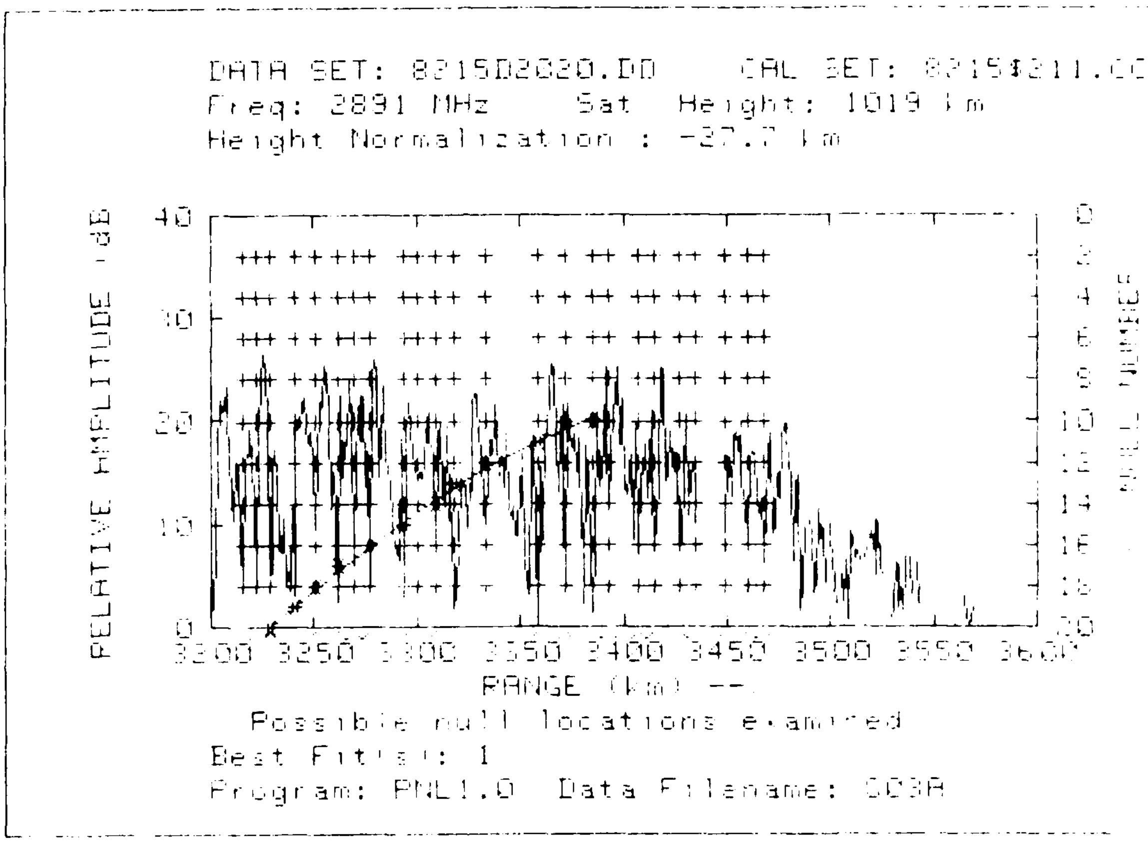

Figure 39. 2891 MHz signal, 3 August at 2020 GMT.

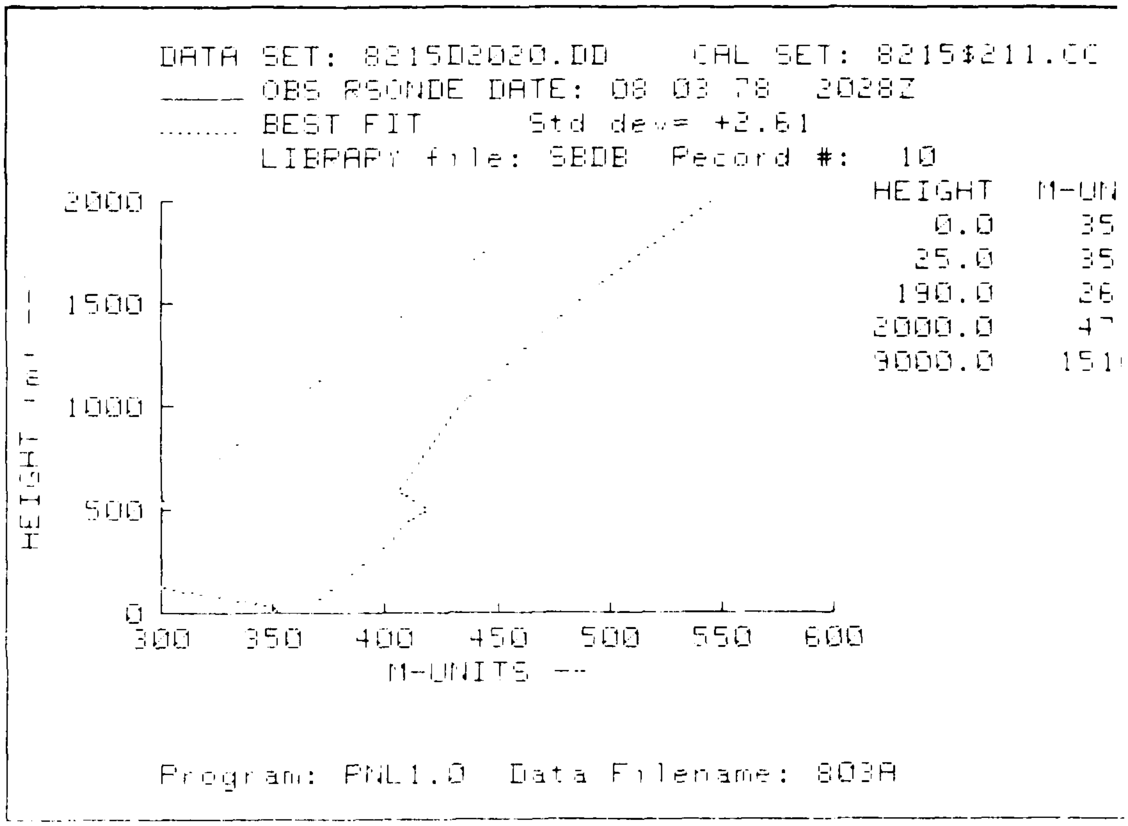

Figure 40. Inferred profile, 2891 MHz.

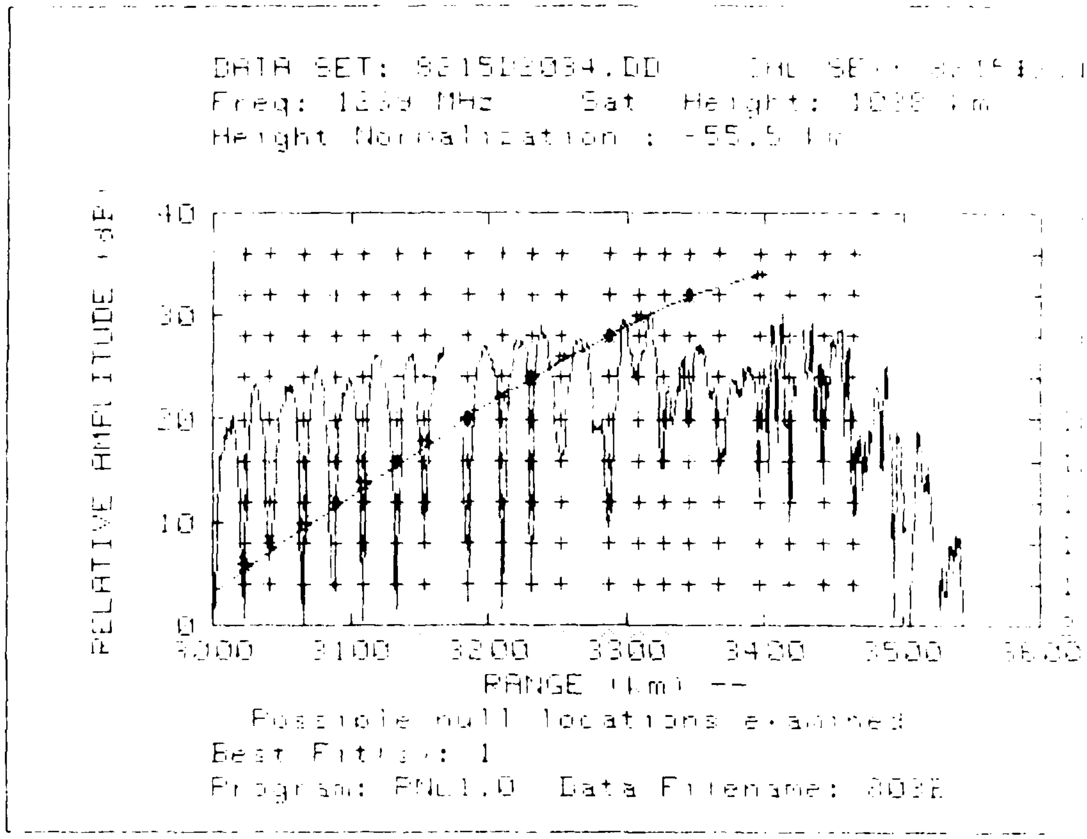

Figure 41. 1239 MHz signal, 3 August at 2034 GMT.

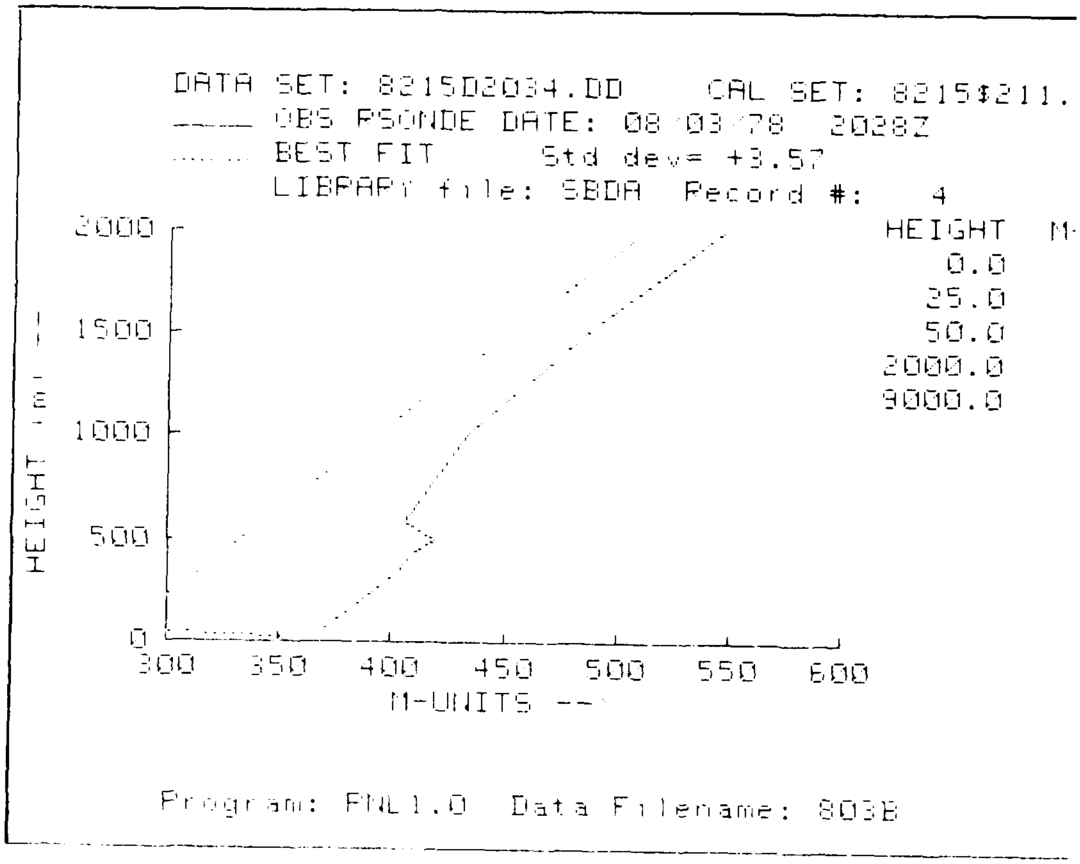

Figure 42. Inferred profile, 1239 MHz.

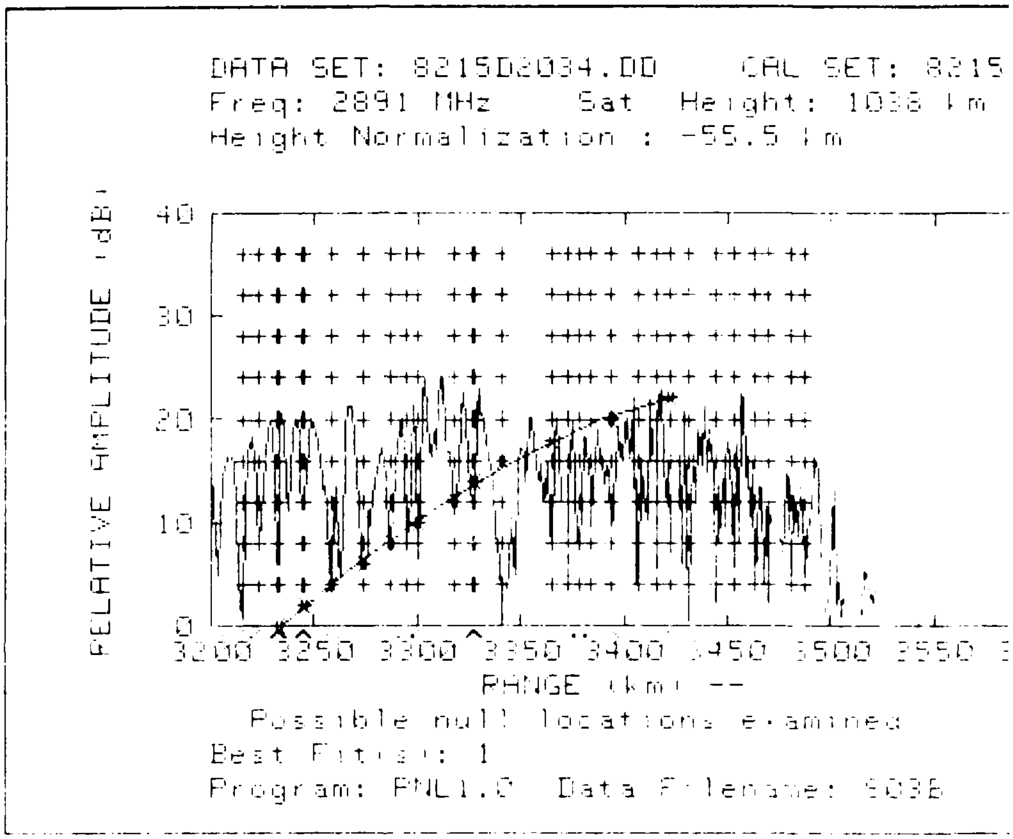

Figure 43. 2891 MHz signal, 3 August at 2034 GM

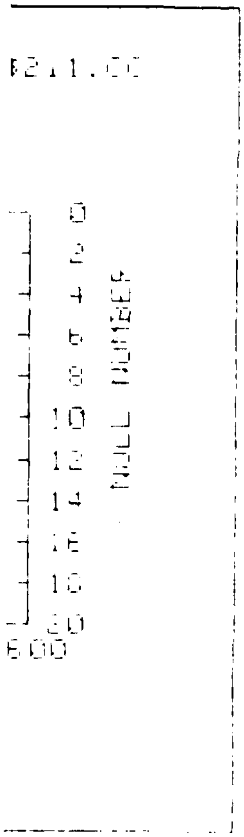

T.

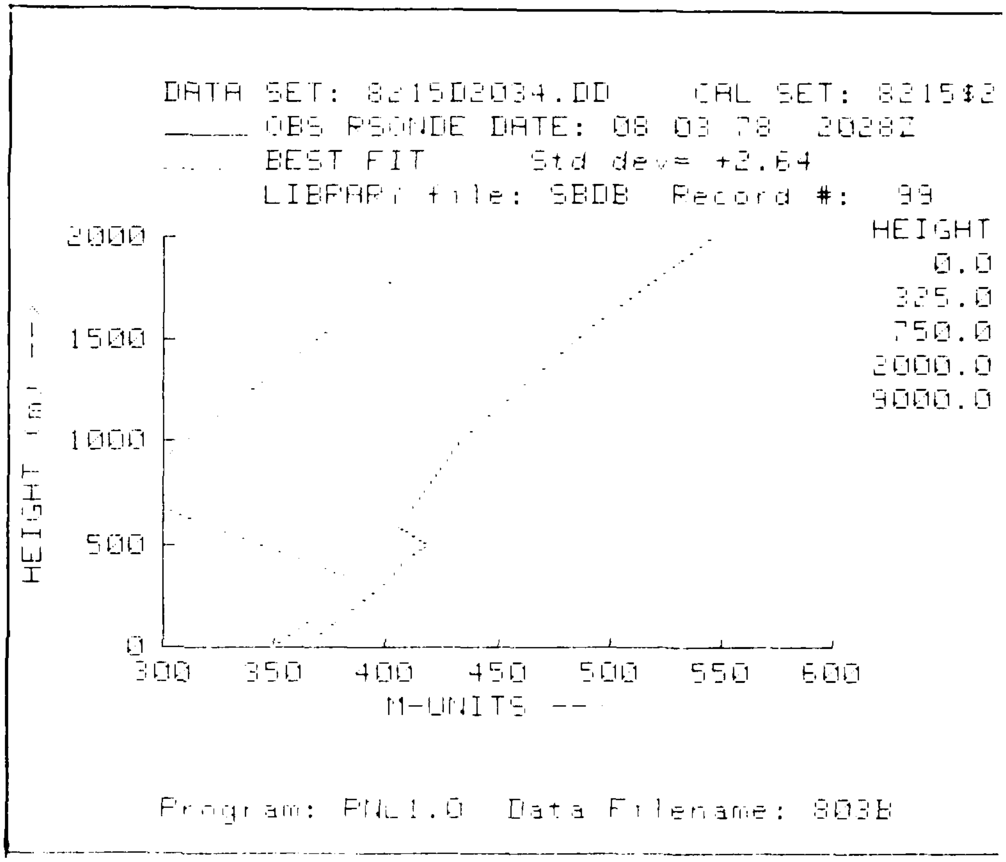

Figure 44. Inferred profile, 2891 MHz.

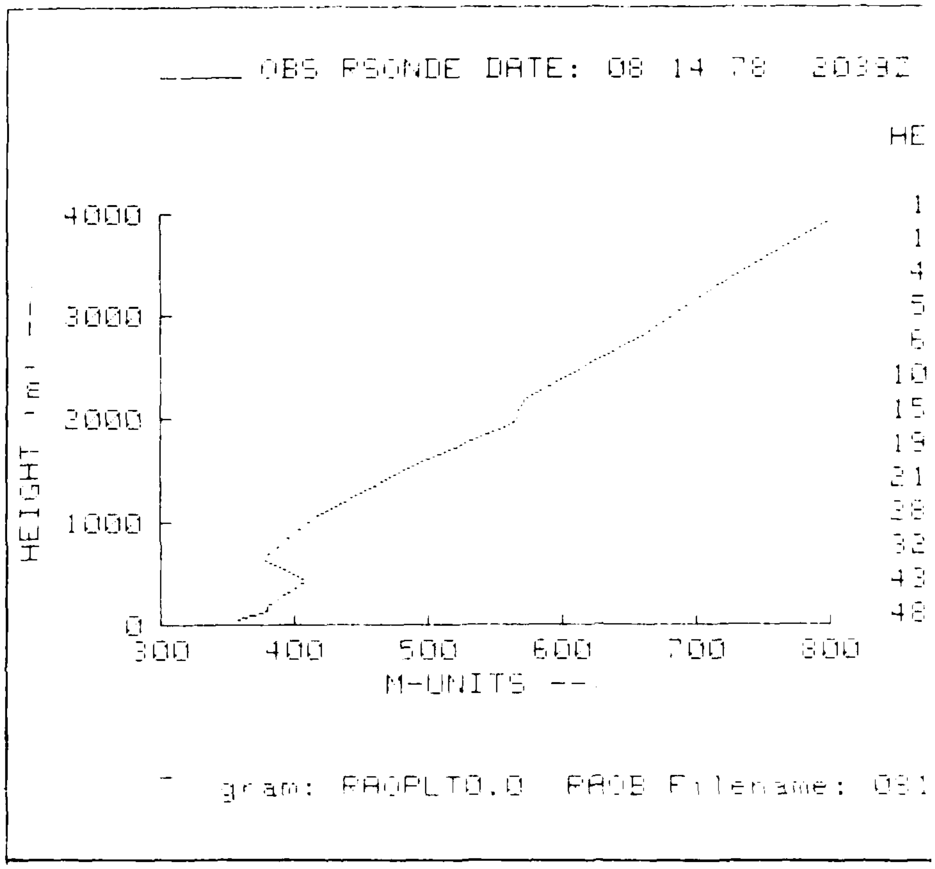

Figure 45. Observed profile, 14 August at

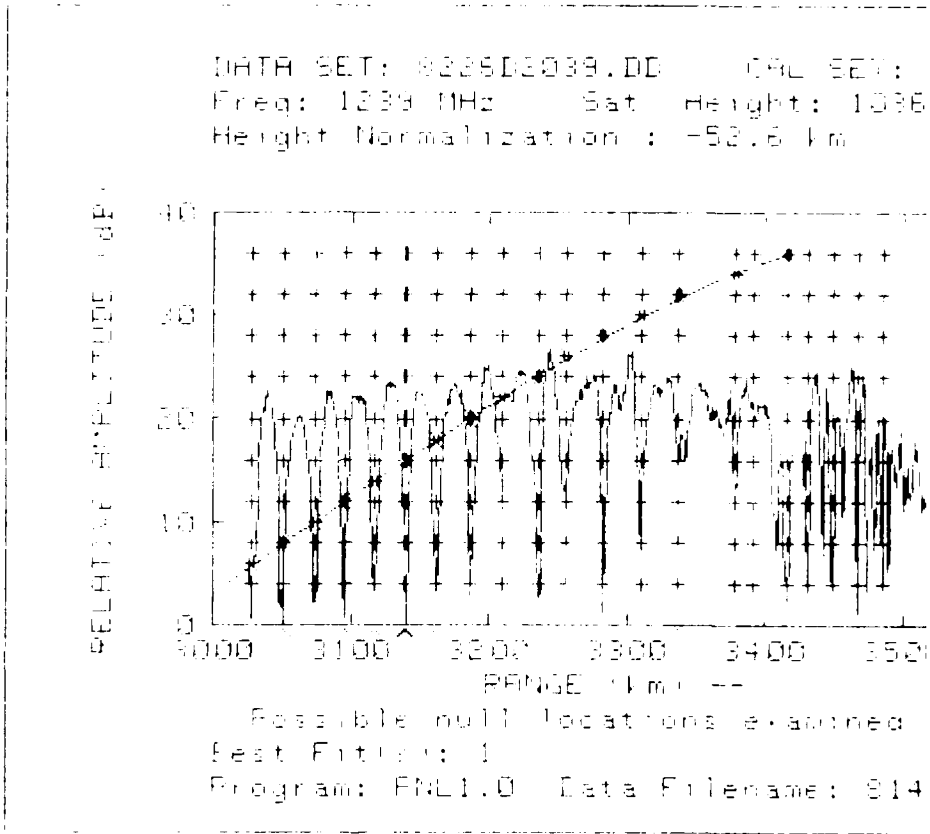

Figure 46. 1239 MHz signal, 14 August at 20

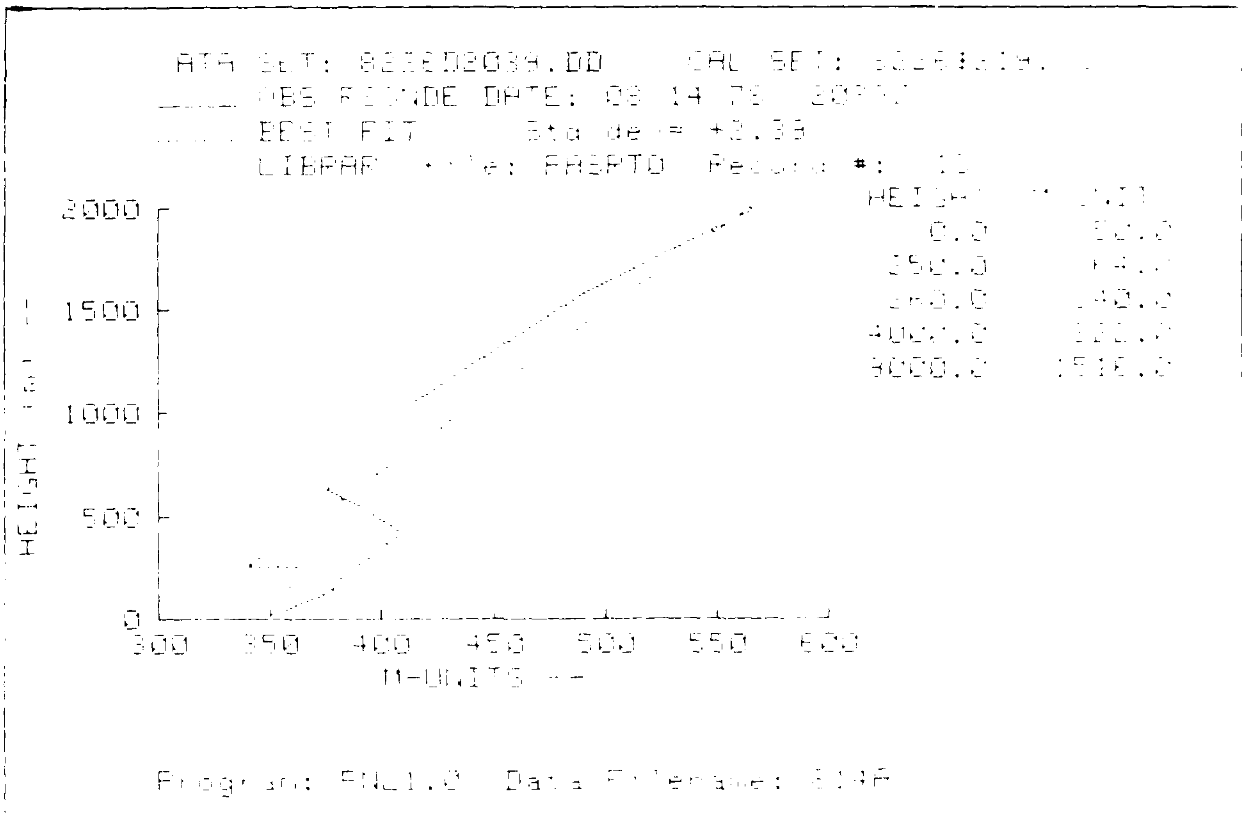

Figure 47. Inferred profile, 1239 MHz.

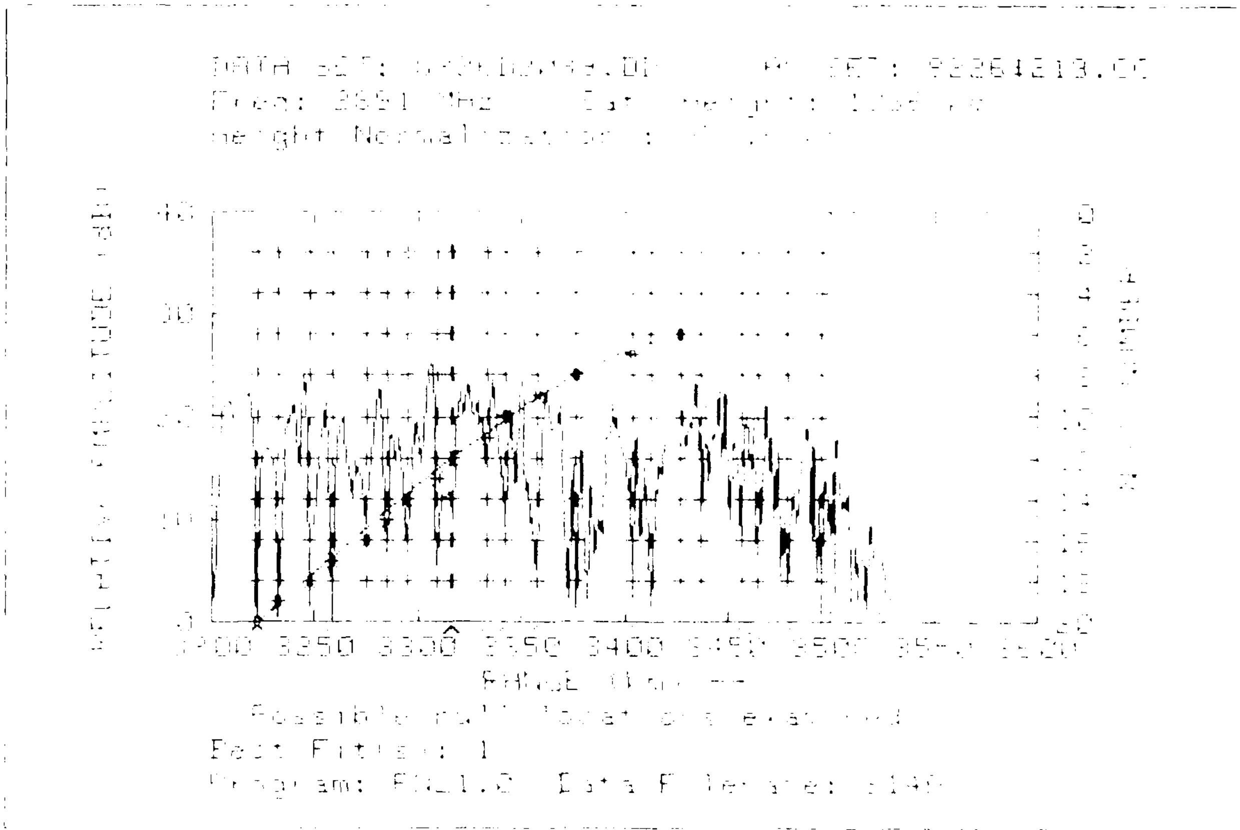

Figure 4[illegible]. [illegible] MHz [illegible], 14 [illegible]

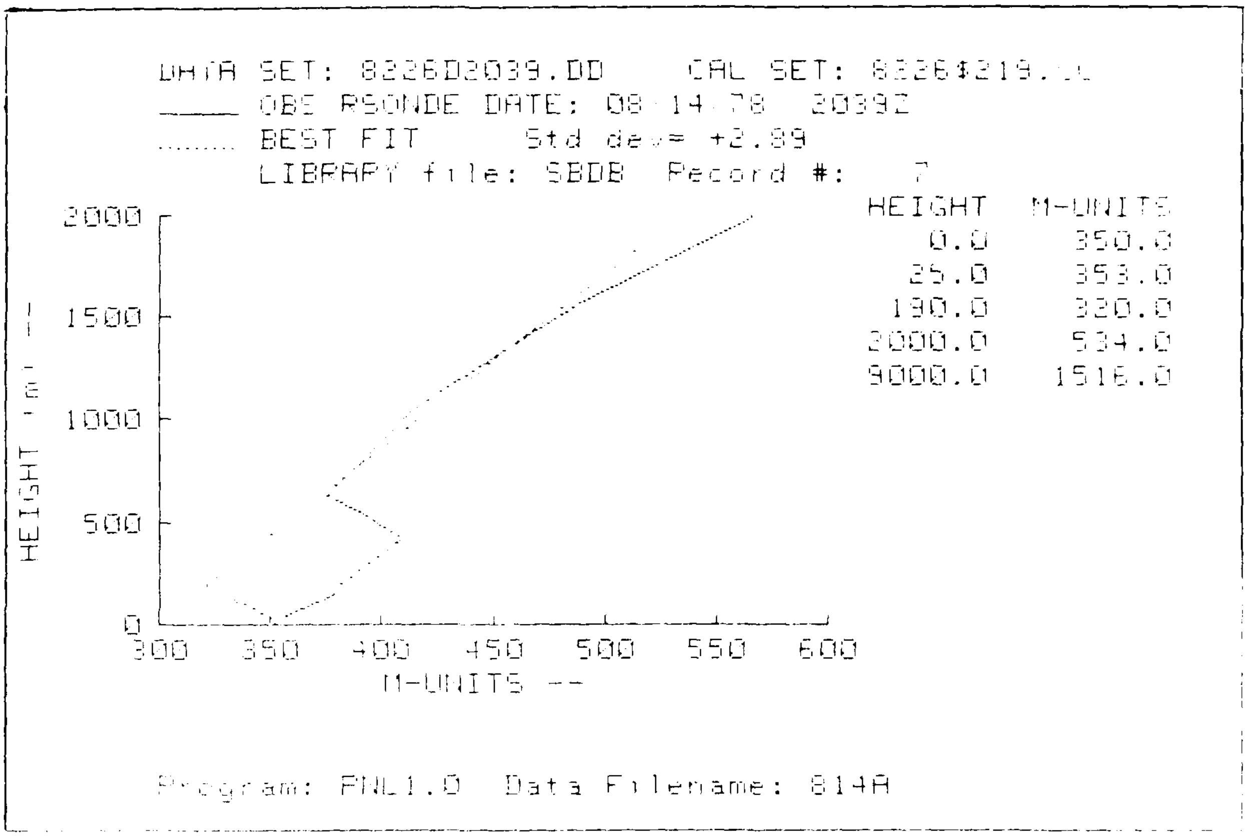

Figure 49. Inferred profile, 2891 MHz.

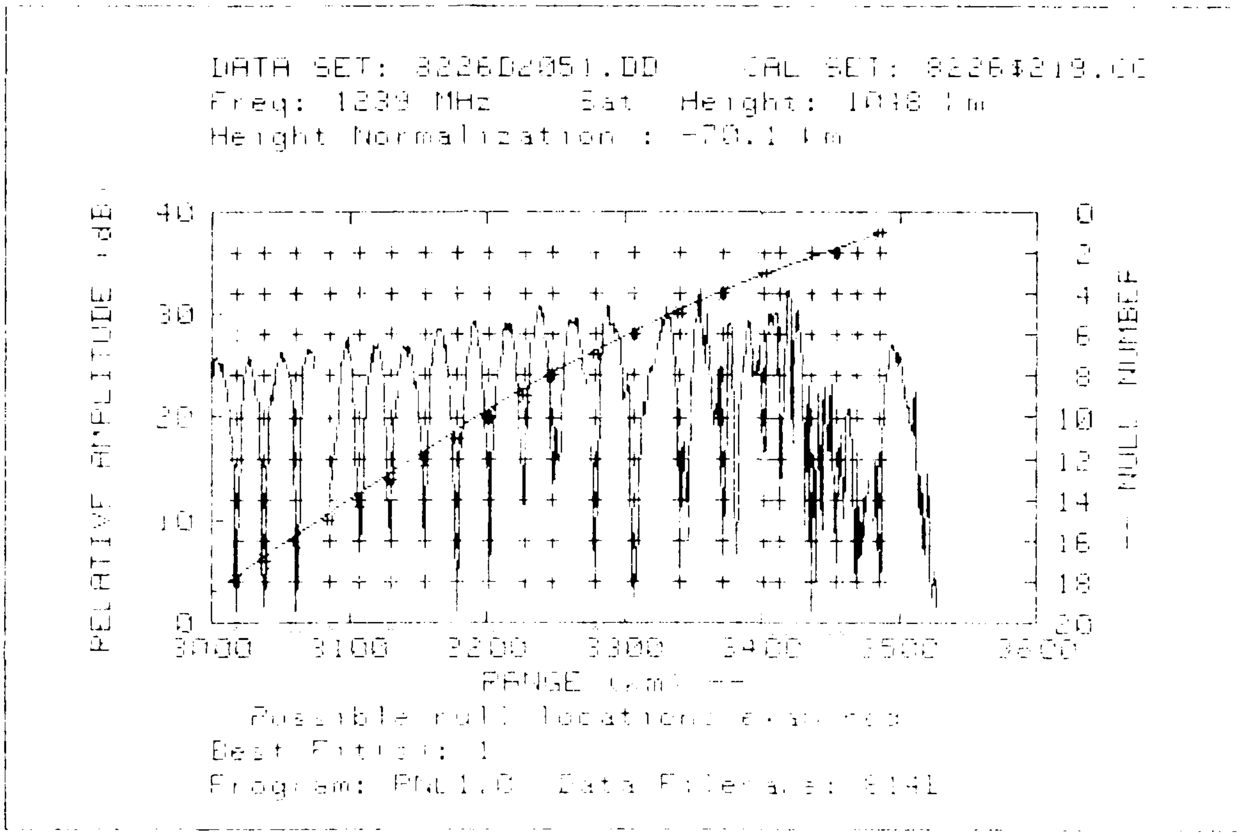

Figure 50. 1239 MHz signal, 14 August at 2051 GMT.

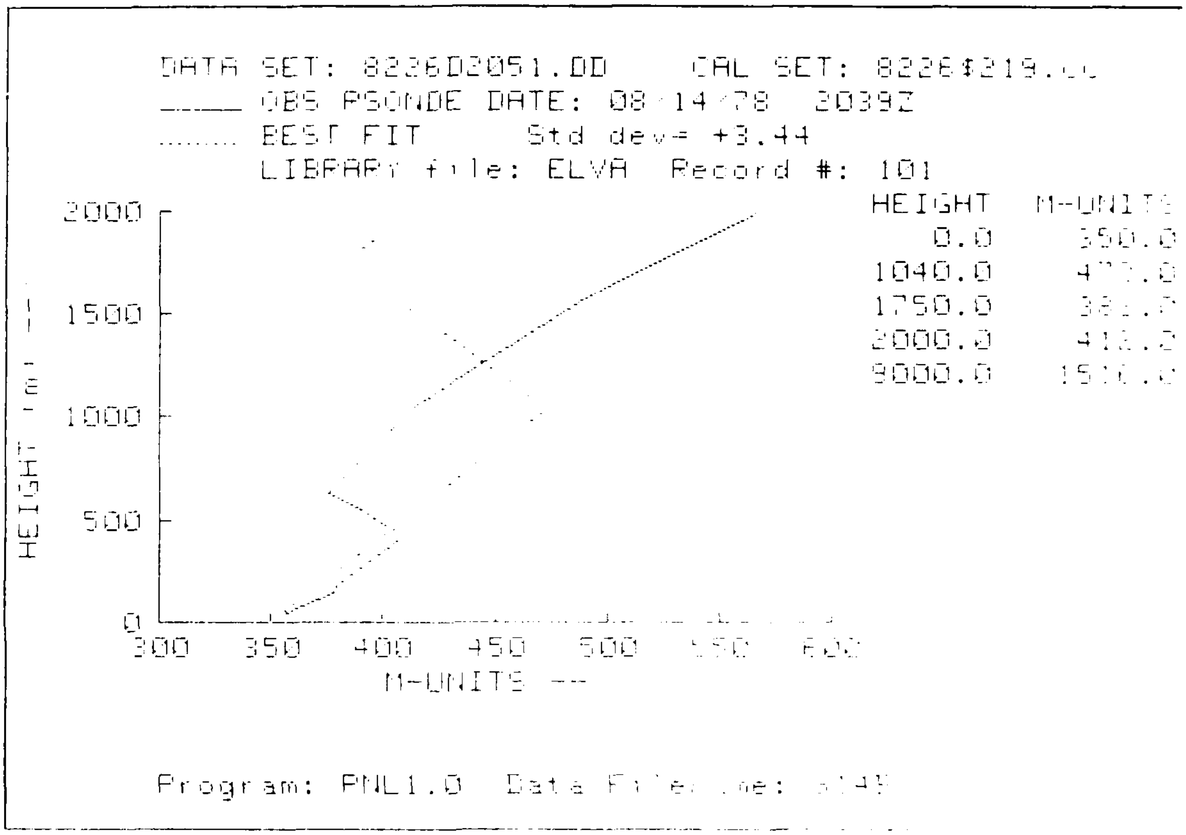

Figure 51. Inferred profile, 1239 MHz.

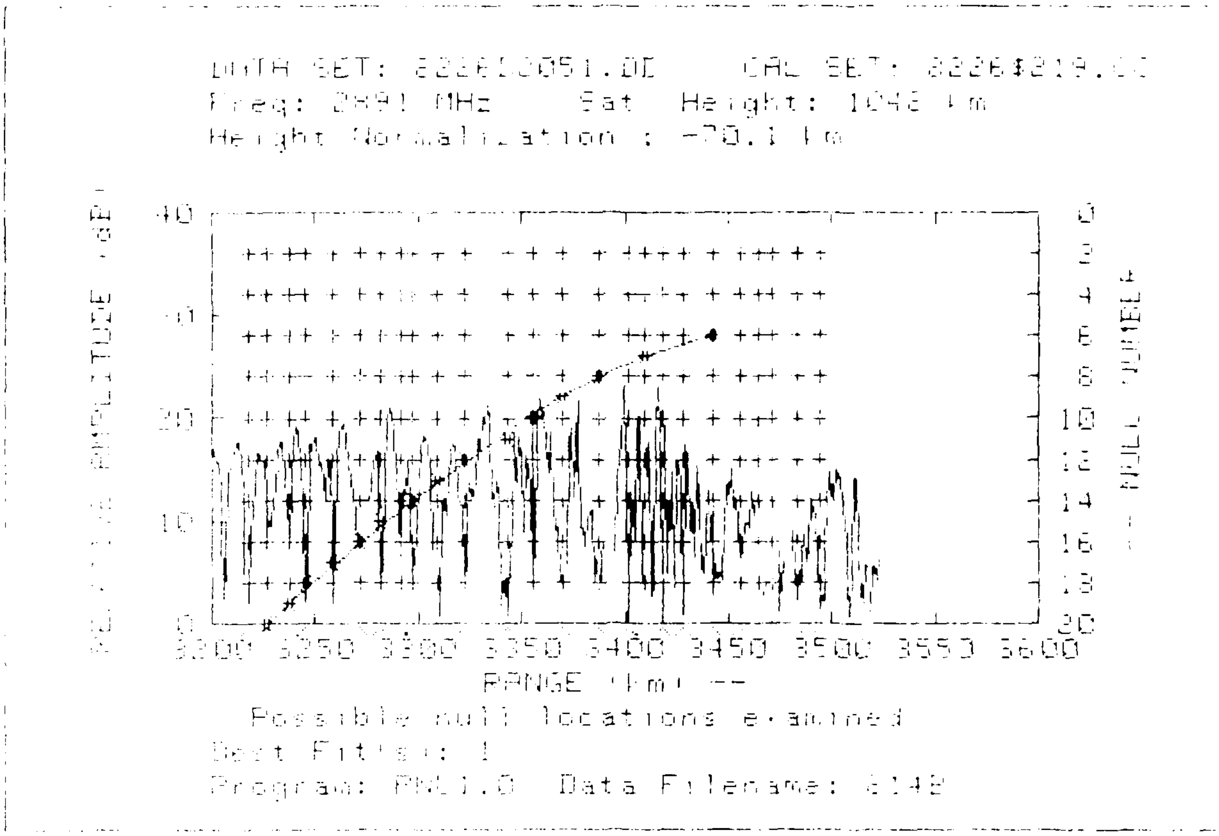

Figure 62. 2891 MHz signal, 14 August at 2051 GMT.

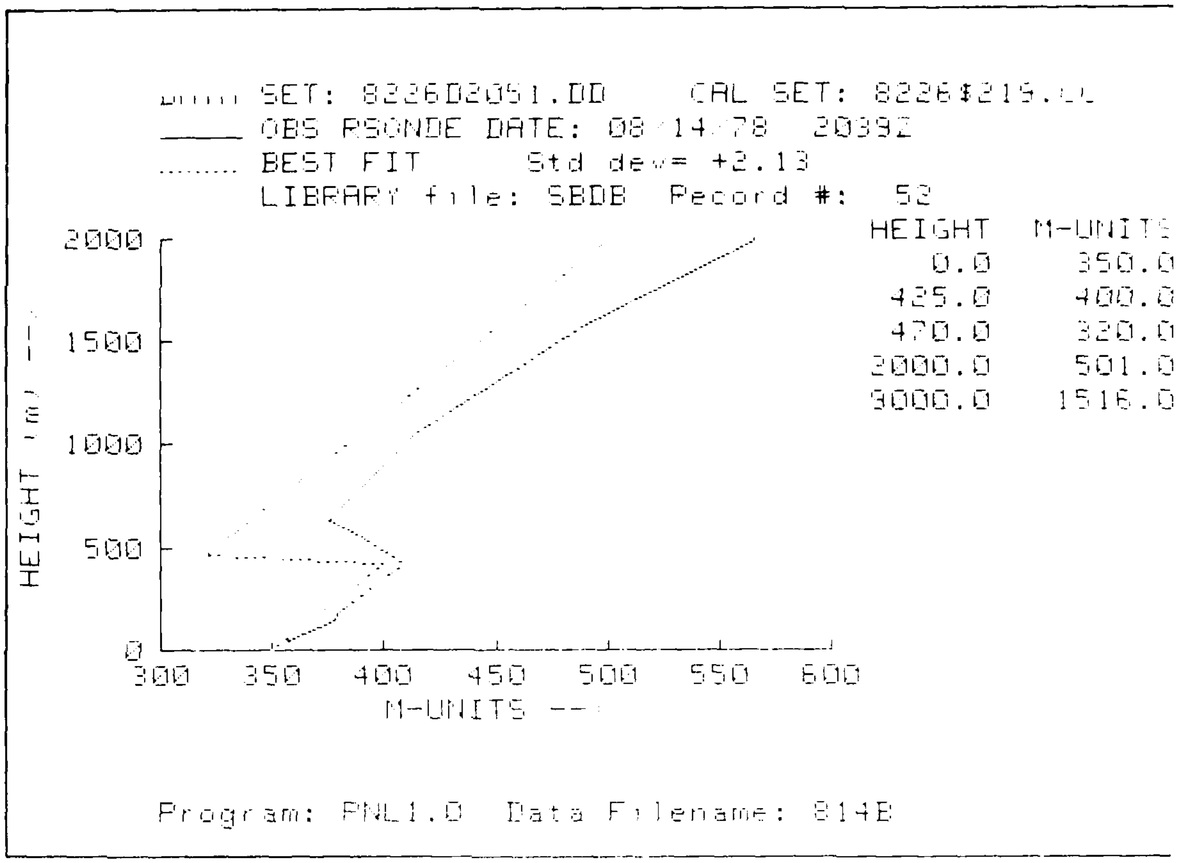

Figure 53. Inferred profile, 2891 MHz.

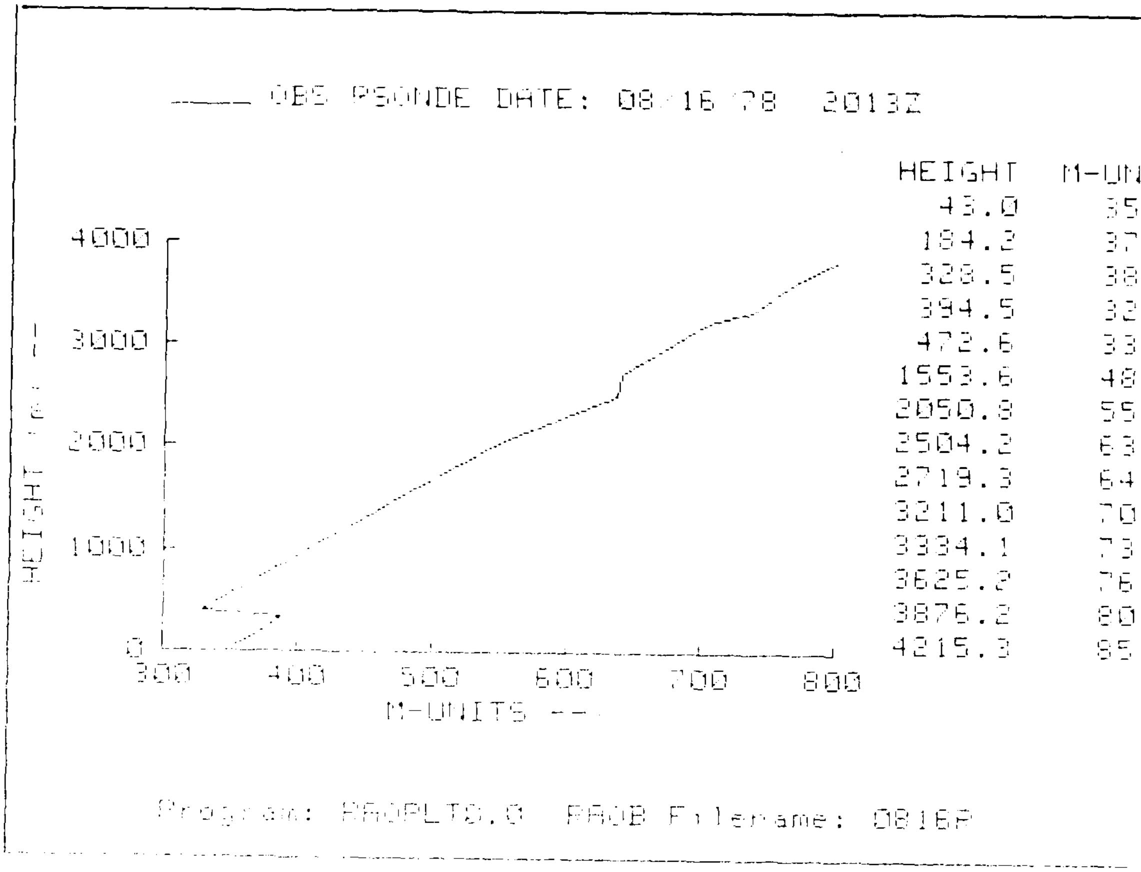

Figure 54. Observed profile, 16 August at 2013 GMT.

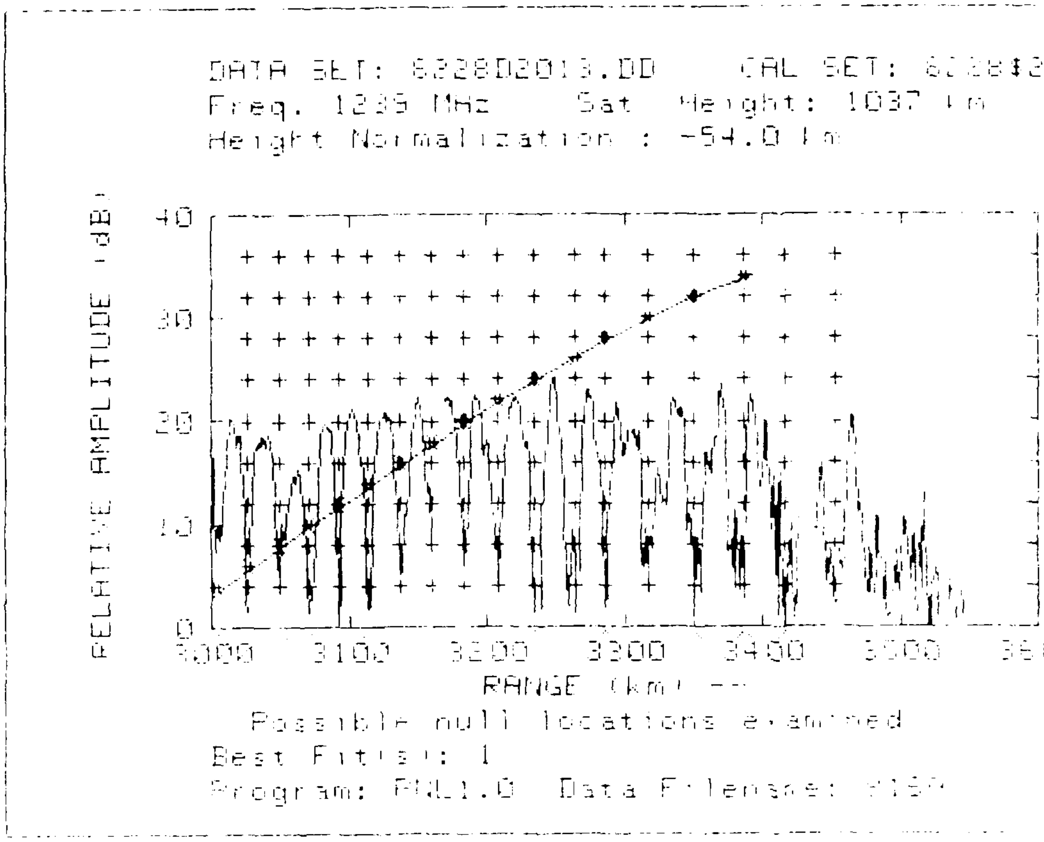

Figure 55. 1239 MHz signal, 16 August at 2013 GMT.

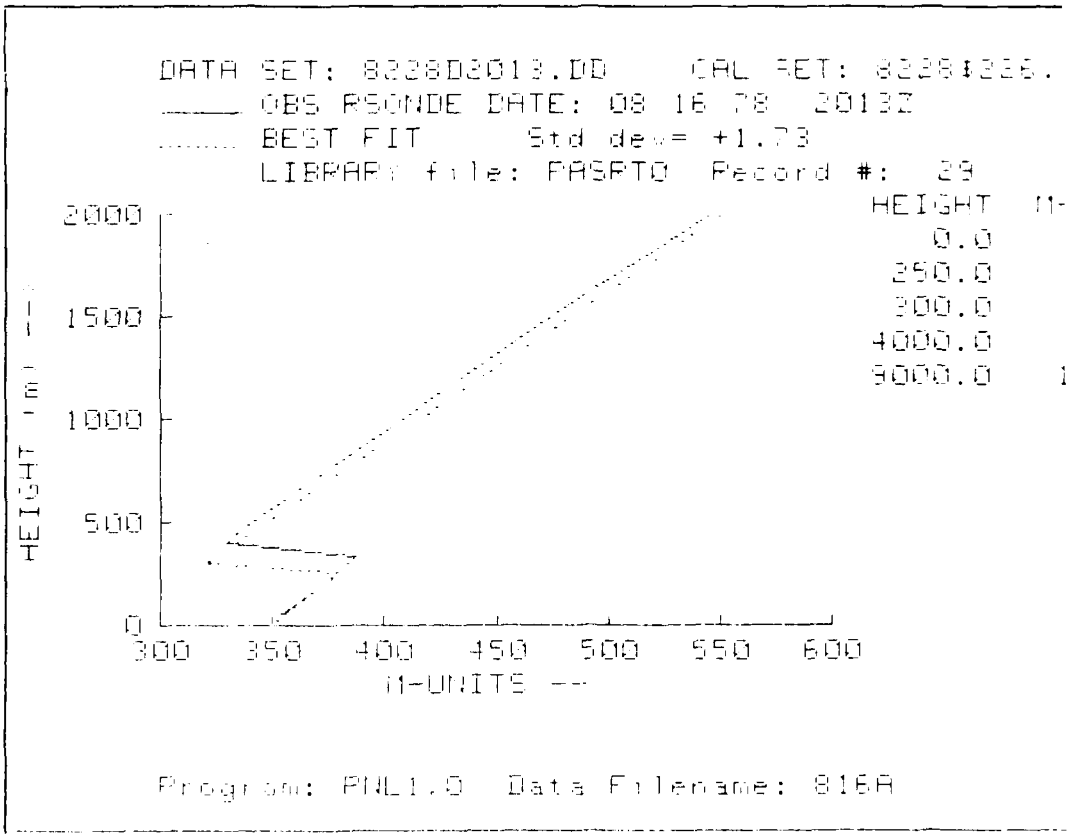

Figure 56. Inferred profile, 1239 MHz.

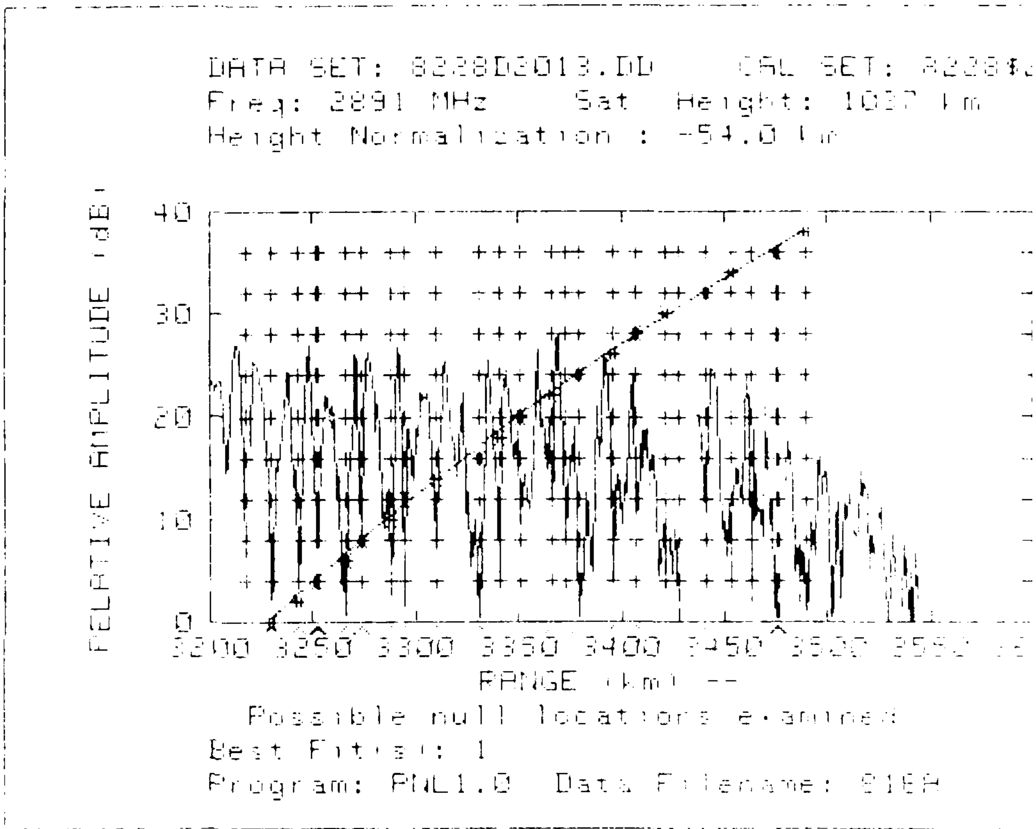

Figure 57. 2891 MHz signal, 16 August at 2013 GMT.

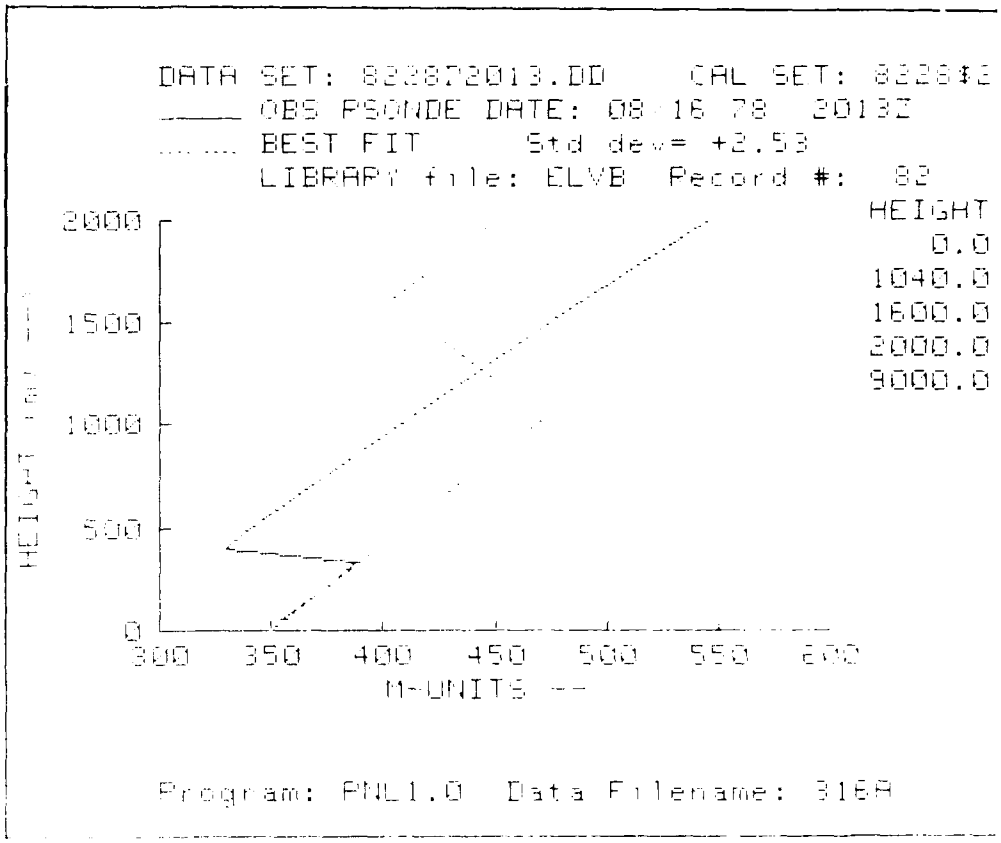

Figure 58. Inferred profile, 2891 MHz.

6.00

M-UNITS
350.0
473.0
403.0
450.0
1516.0

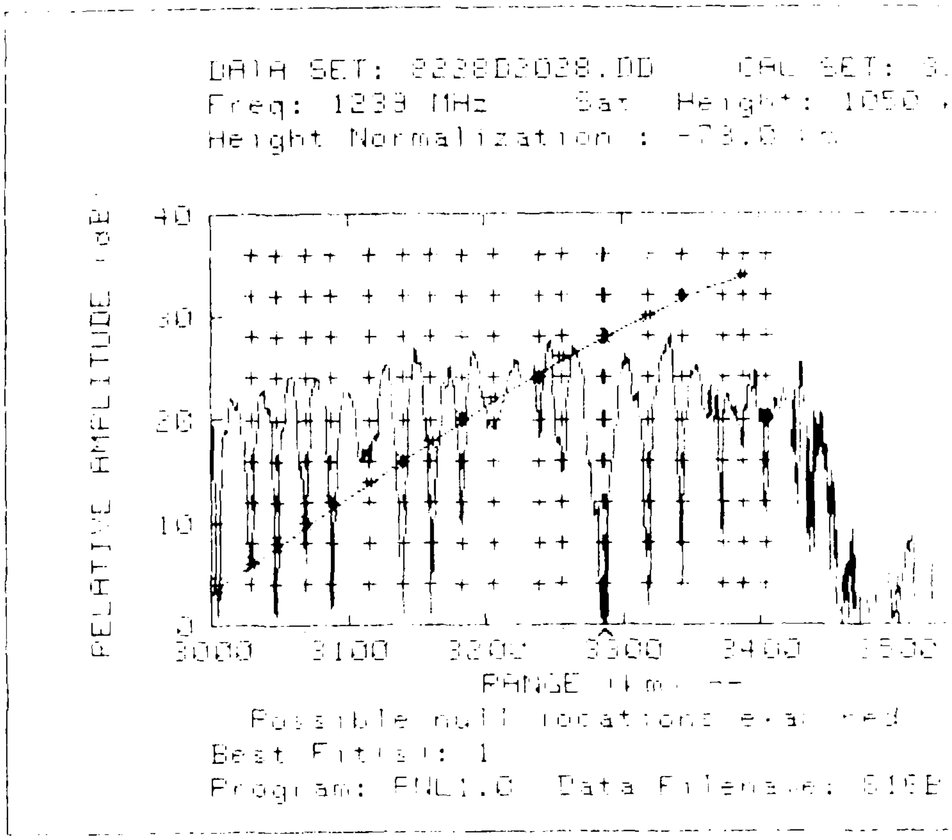

Figure 59. 1239 MHz signal, 16 August at

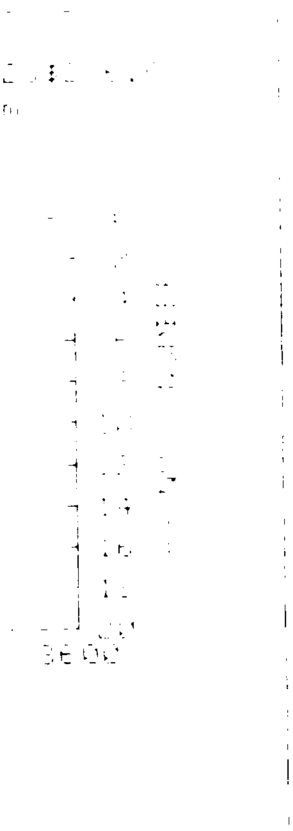

2028 GMT.

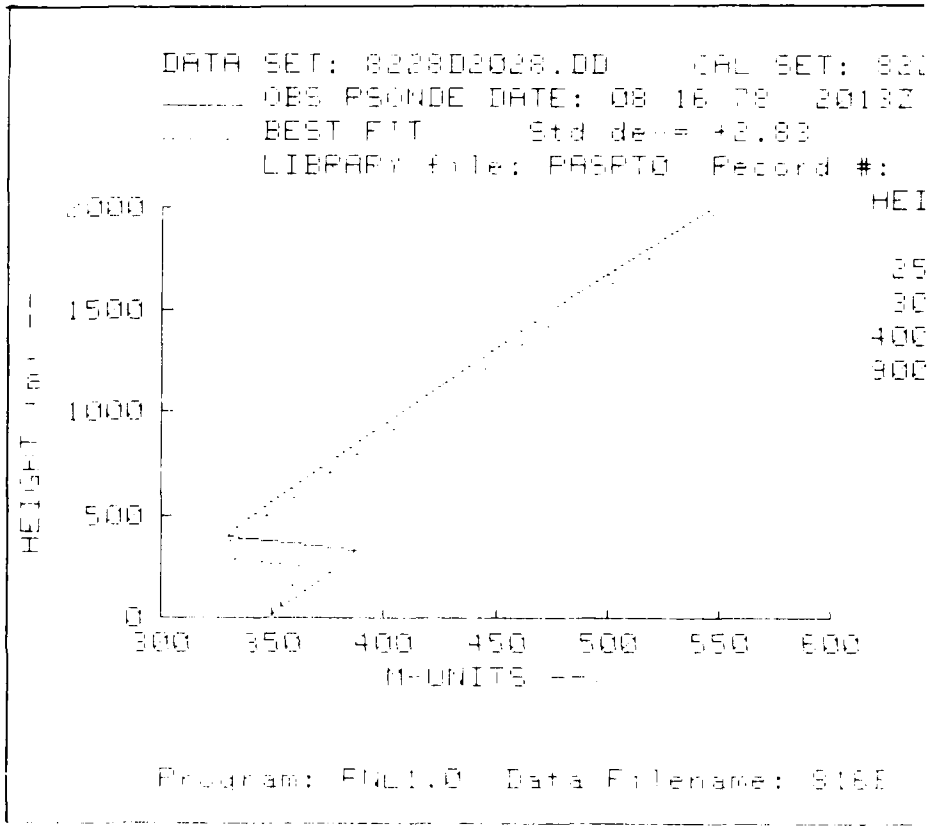

Figure 60. Inferred profile, 1239 MHz.

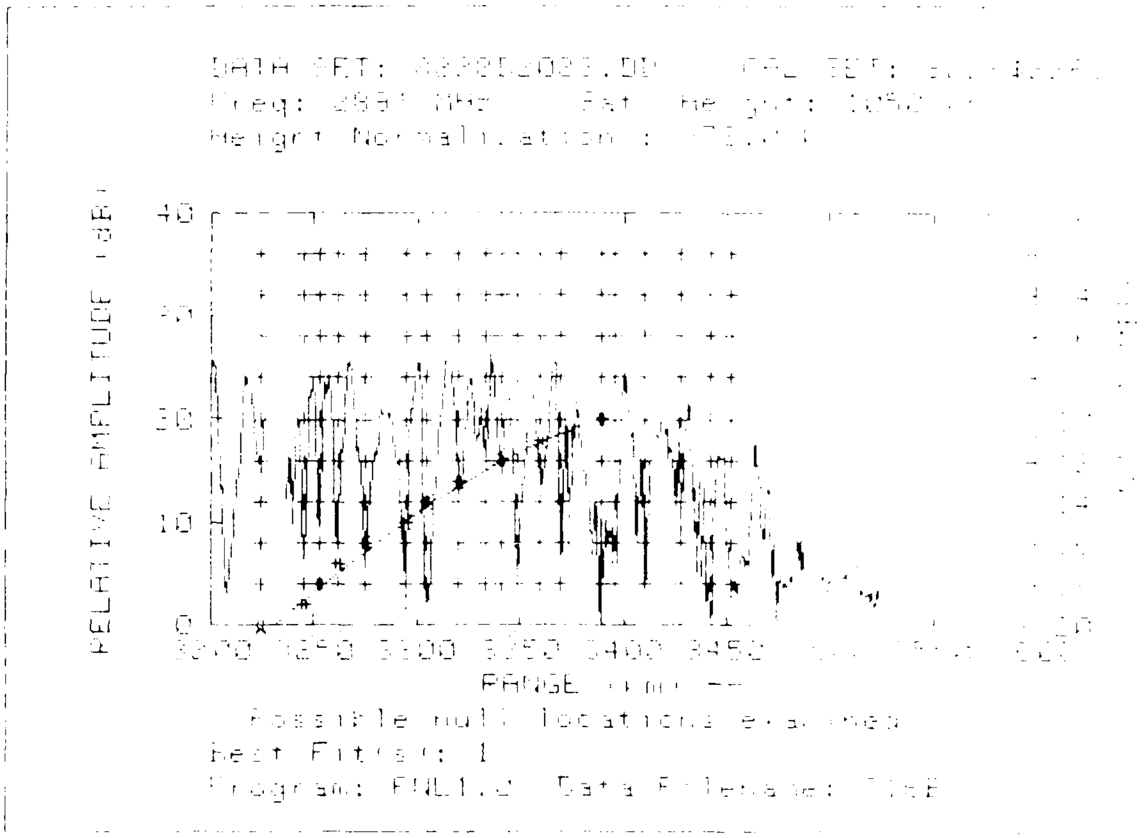

Figure 61. 2891 MHz signal, 16 August at 2028 GMT.

AD-A095 498   NAVAL OCEAN SYSTEMS CENTER SAN DIEGO CA   F/G 4/1
TROPOSPHERIC REFRACTIVITY PROFILES INFERRED FROM RF MEASUREMENT--ETC(U)
OCT 80 K D ANDERSON
UNCLASSIFIED   NOSC/TR-629   NL

2 OF 2
AD A
095498

END
DATE
FILMED
3-81
DTIC

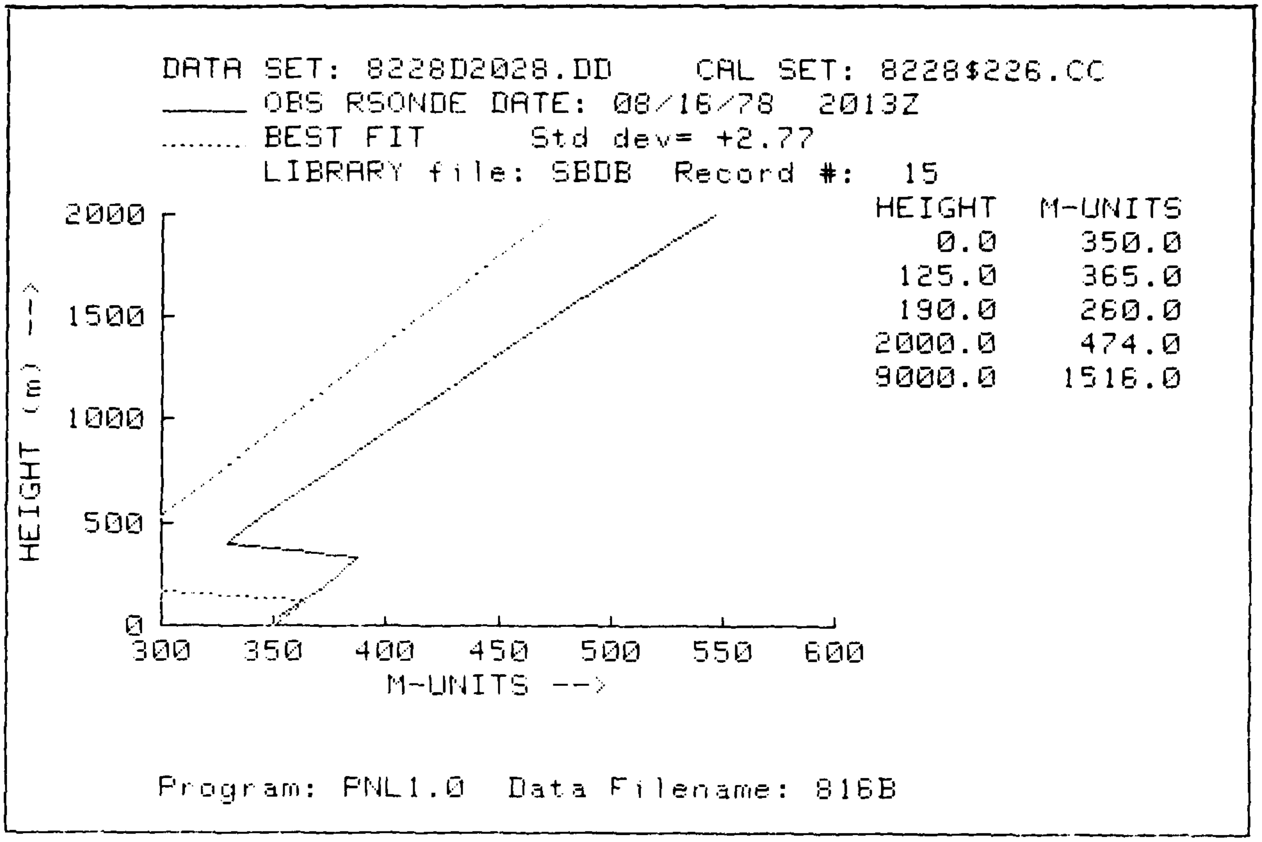

Figure 62. Inferred profile, 2891 MHz.

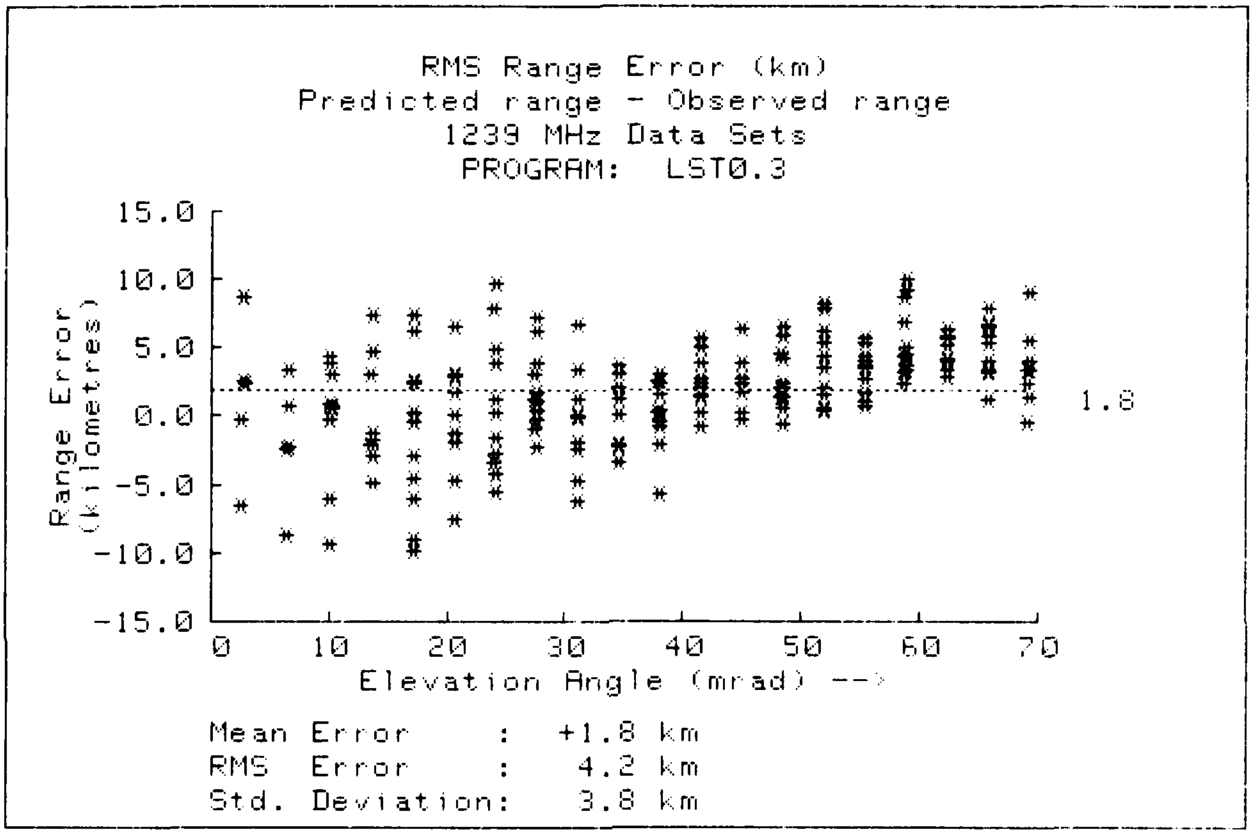

Figure 63. Range error, 1239 MHz.

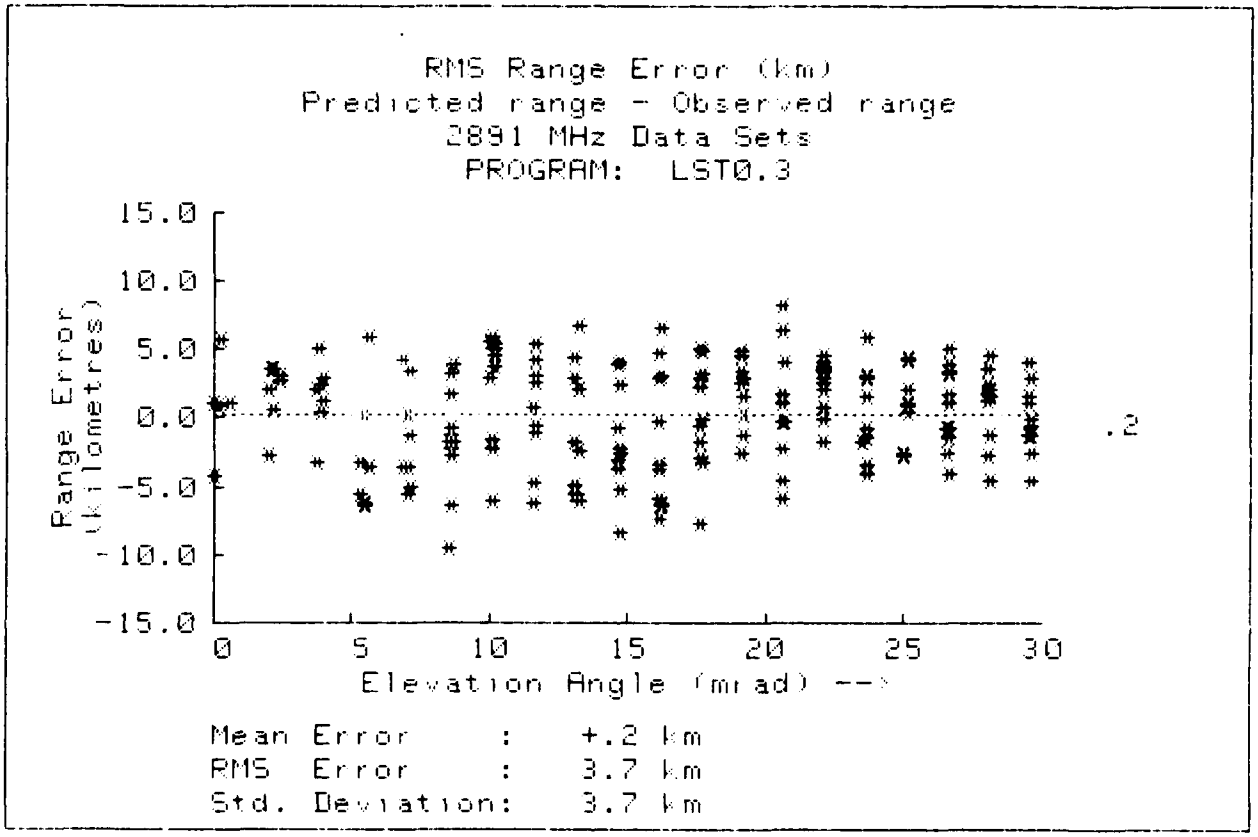

Figure 64. Range error, 2891 MHz.

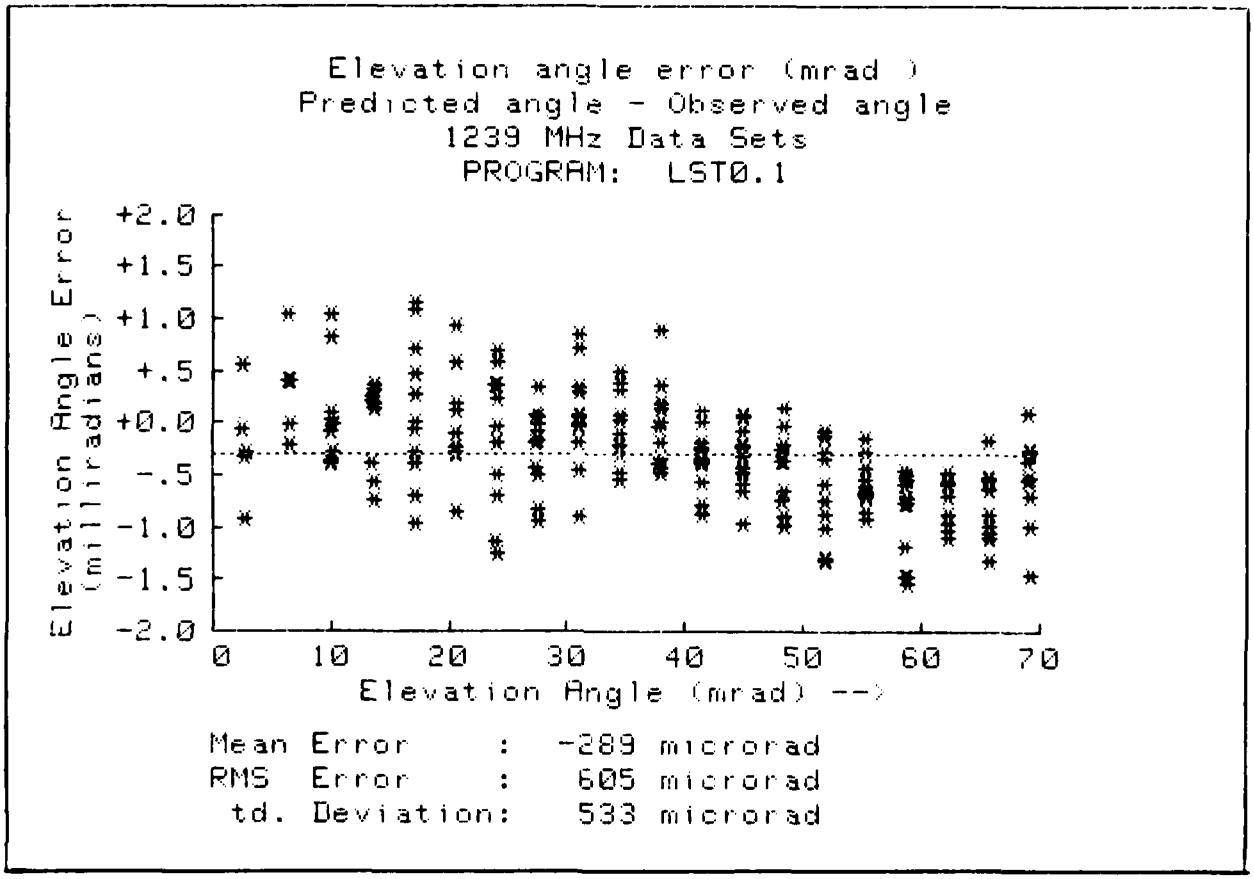

Figure 65. Elevation angle error, 1239 MHz.

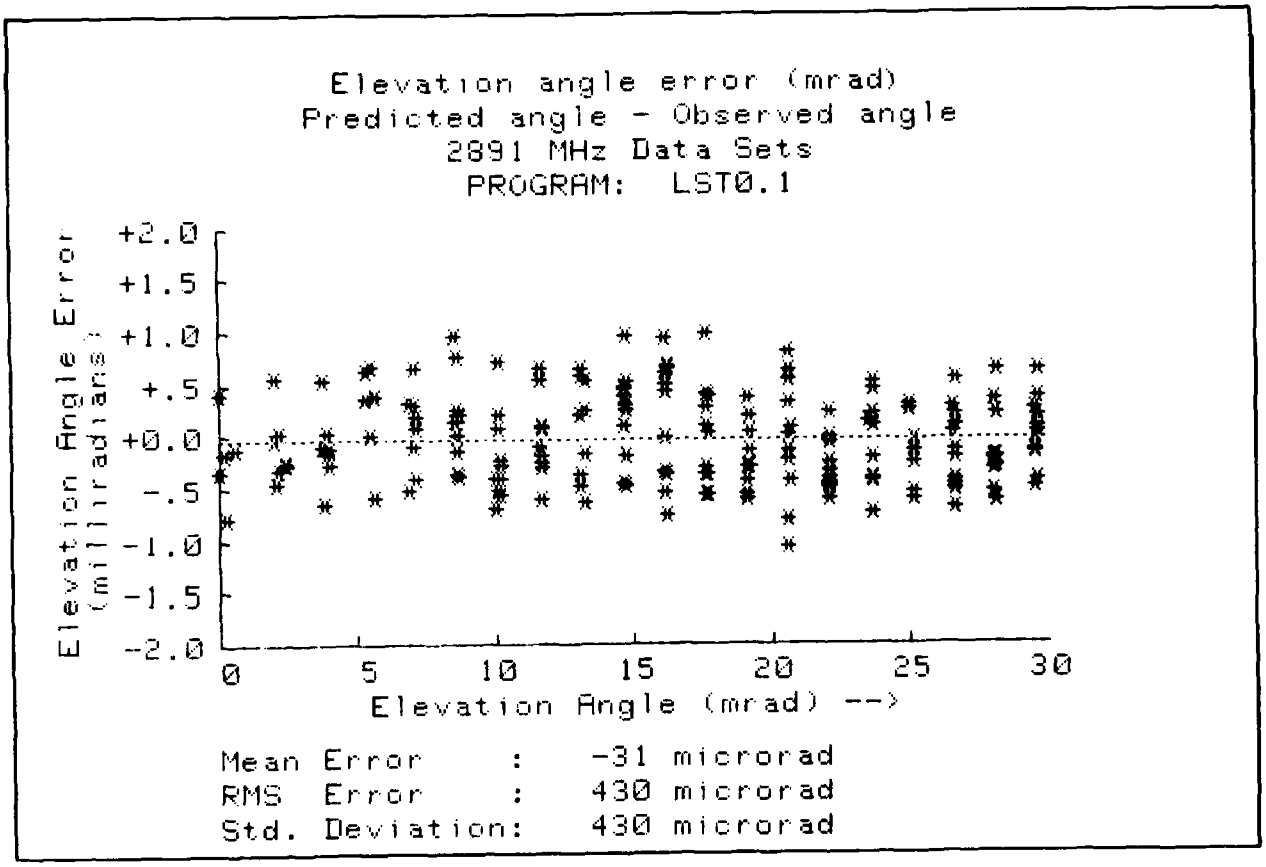

Figure 66. Elevation angle error, 2891 MHz.

DATE

ILME